

**Wind Machines for Frost Damage Mitigation  
Experimental and numerical investigations**

Dai, Y.

**DOI**

[10.4233/uuid:7000b291-671c-4ab3-86fa-beeff39bf5df](https://doi.org/10.4233/uuid:7000b291-671c-4ab3-86fa-beeff39bf5df)

**Publication date**

2025

**Document Version**

Final published version

**Citation (APA)**

Dai, Y. (2025). *Wind Machines for Frost Damage Mitigation: Experimental and numerical investigations*. [Dissertation (TU Delft), Delft University of Technology]. <https://doi.org/10.4233/uuid:7000b291-671c-4ab3-86fa-beeff39bf5df>

**Important note**

To cite this publication, please use the final published version (if applicable).  
Please check the document version above.

**Copyright**

Other than for strictly personal use, it is not permitted to download, forward or distribute the text or part of it, without the consent of the author(s) and/or copyright holder(s), unless the work is under an open content license such as Creative Commons.

**Takedown policy**

Please contact us and provide details if you believe this document breaches copyrights.  
We will remove access to the work immediately and investigate your claim.

# **WIND MACHINES FOR FROST DAMAGE MITIGATION**

EXPERIMENTAL AND NUMERICAL INVESTIGATIONS



# **WIND MACHINES FOR FROST DAMAGE MITIGATION**

EXPERIMENTAL AND NUMERICAL INVESTIGATIONS

## **Dissertation**

for the purpose of obtaining the degree of doctor  
at Delft University of Technology,  
by the authority of the Rector Magnificus, prof. dr. ir. T.H.J.J. van der Hagen,  
chair of the Board for Doctorates,  
to be defended publicly on 20 January 2025 at 15:00.

by

**Yi DAI**

Master of Environmental Science,  
Delft University of Technology, Delft, The Netherlands,  
born in Hubei, China.

This dissertation has been approved by the promotor

promotor: Prof. dr. ir. B.J.H. van de Wiel

copromotor: Dr. ir. J.A.E. ten Veldhuis

Composition of the doctoral committee:

Rector Magnificus,	chairperson
Prof. dr. ir. B.J.H. van de Wiel,	Delft University of Technology
Dr. ir. J.A.E. ten Veldhuis,	Delft University of Technology

*Independent members:*

Dr. ir. A.M.J. Coenders	Delft University of Technology
Dr. ir. R.J. Ronda,	KNMI
Prof. dr. ir. A.P. Siebesma,	Delft University of Technology
Prof. dr. ir. S.C. Steele-Dunne,	Delft University of Technology
Prof. dr. ir. D. Zardi,	University of Trento

The author received financial support from the Netherlands Organization for Scientific Research (NWO) project EN-WSS.2018.006, with Prof. dr. B.J.H. van de Wiel leads as the principal investigator (P.I.).

*Keywords:* Frost damage mitigation; Wind Machine; Distributed Temperature Sensing; Large-eddy Simulation; plant-tissue temperature

*Front & Back:* The cover picture was taken at the orchard of Krabbendijke. The wind machine in the middle is enlarged for better visibility. The picture was applied with a artistic canvas filter in GIMP.

Copyright © 2024 by Y. Dai

An electronic version of this dissertation is available at  
<http://repository.tudelft.nl/>.

# CONTENTS

<b>Summary</b>	<b>vii</b>
摘要	<b>xi</b>
<b>1 Introduction</b>	<b>1</b>
1.1 Frost and Frost mitigation . . . . .	2
1.2 Wind machines for frost damage mitigation . . . . .	3
1.3 Research tools and questions . . . . .	5
<b>2 A quantitative 3D investigation based on observations</b>	<b>7</b>
2.1 Introduction . . . . .	8
2.2 Experimental setup . . . . .	10
2.3 Results and Discussion . . . . .	12
2.4 Conclusion . . . . .	24
<b>3 An integrated large-eddy simulation for modeling plant-tissue warming</b>	<b>27</b>
3.1 Introduction . . . . .	28
3.2 The integrated model . . . . .	29
3.3 Simulation settings . . . . .	32
3.4 Results and discussion . . . . .	36
3.5 Conclusion . . . . .	45
<b>4 From smooth wall flow to grass-canopy flows</b>	<b>47</b>
4.1 Introduction . . . . .	48
4.2 Model description and setup . . . . .	49
4.3 Results from DNSs . . . . .	50
4.4 Conclusion and discussion . . . . .	60
<b>5 Conclusion</b>	<b>65</b>
5.1 Summary of conclusions . . . . .	65
5.2 Implications for the agricultural sector and farmers. . . . .	67
5.3 Research outlook . . . . .	68
<b>Bibliography</b>	<b>78</b>
<b>Acknowledgements</b>	<b>79</b>
<b>A Appendix</b>	<b>81</b>
A.1 Error analysis . . . . .	81
A.2 Description of Quadrant-Hole (QH) analysis . . . . .	82
A.3 Periodic boundary conditions in a large-size domain . . . . .	84

**Curriculum Vitæ**

**87**

**List of Publications**

**89**

# SUMMARY

Frost is a meteorological phenomenon that can cause significant damage to crops and fruit plants, leading to substantial economic losses in the agricultural sector. In 2017, spring frosts caused losses amounting to 3.3 billion euros across Europe (Lamichhane, 2021). In France, at least half of the 680 km<sup>2</sup> of vineyards were damaged due to frost events in 2021 (Liubchenkova, 2021). Due to global warming, bud blooming tends to occur much earlier, while the probability of single frost nights in spring remains the same. Consequently, crop vulnerability increasingly coincides with the frost season. Effective mitigation methods such as sprinkling, wind machines, and paraffin pots remain essential for preventing crop damage.

Among various mitigation methods, wind machines are potentially cost-effective and energy-efficient. However, little is known about the warming effectiveness of wind machines and the physical mechanisms behind the warming process. Therefore, the primary motivation of this thesis is to investigate whether wind machines are effective warming devices for future frost damage mitigation. However, current physical understanding of machine-induced warming remains limited. Experimental studies often face challenges with the coverage and resolution of measurements, which are typically insufficient to fully capture the temporal and spatial variability of machine-induced air mixing in orchards. Furthermore, there are only a few numerical studies available. The dynamic interplay between turbulent warming plumes and canopy structure, as well as the heterogeneous plant-air heat exchange in the orchard, has not been investigated numerically so far.

We address these challenges using a combination of an experimental field study (Chapter 2) and a numerical modeling study (Chapter 3). We employed the technique of Distributed Temperature Sensing (DTS) to measure the spatial and temporal temperature responses before and after the wind machine operation. The DTS technique is a fiber optic-based sensing technique that can measure temperature at high spatial (sampling at 0.25 m) and temporal (10 s) resolution along the fiber optic cables. Based on physical insights from quasi-3D temperature measurements over 6.75 ha, we developed a numerical model that simulates the warming effects of wind machines on plant tissues and near-canopy air (Chapter 3). The strong jet motions induced by the wind machine are simulated using an actuator disk parameterization model. To incorporate the effects of the orchard canopy, we employed a canopy parameterization model. To further diagnose the plant-tissue warming process, we integrated a conceptual plant-air heat exchange model into the canopy module. From those studies we found:

- **Chapter 2: Observational Evidence:** we provide observational evidence that indeed wind machine operation results in a significant warming of the fruit trees and the air near the surface. By measuring the quasi-3D temperature responses over a 6.75 ha orchard, we found a 30% and 50% reduction in local inversion strength

(8°C) over 2.66 ha and 0.45 ha, respectively. On average, wind machine operation raised in-canopy temperature by 3 K within 40 minutes. To the best of our knowledge, Chapter 2 is the first study to quantify the machine-induced warming effects over such large area with high resolution observations.

- **Chapter 2 and 3: Non-negligible Background Wind Effects:** Based on observations and numerical simulations, we showed that even a very light background wind ( $0.2 \text{ m s}^{-1}$ ) causes a strong difference in the warming of air and leaves upstream compared to downstream of the wind machine. Advection effects result in a ‘plume drift’ of 60 m over a rotation period of 5 minutes. Interaction between the jet and the background wind creates wave-like patterns downstream of the wind machine and flow convergence upstream. The warming range is much further downstream (550 m) in comparison to upstream (150 m). In the cross-stream direction, warming ranges for air and leaves extend approximately 250 meters on each side.
- **Chapter 2: Flux Transport:** We quantified the effect of wind machine operation on vertical heat flux transport using so-called Quadrant-Hole analysis. Flux transport during operation is dominated by sweeping and ejection motions. Downdrafts of warm air and updrafts of cool air are intermittent but effective in vertical heat exchange. By inducing those turbulent sweeps and ejections, wind machines are highly effective in increasing canopy airspace temperature to mitigate frost damage.
- **Chapter 3: Numerical Model Development:** We developed a numerical model to simulate the warming effects of wind machines on canopies (e.g., plant-tissue temperatures) in orchards. The model, based on the Large Eddy Simulation (LES) method, incorporates a canopy model, an air-plant-tissue heat exchange model, and a wind machine model. Simulation results were compared with measurements taken at a 9 m tower and with a horizontal measurement plane over a 6.75 ha orchard. The numerical model closely reproduces the mixing and warming effects of wind machine operation observed in the orchard canopy, providing a useful surrogate for outdoor reality with respect to wind machine operation in orchards. The model therefore can be used for future sensitivity and scenario studies, as to explore optimization of wind machine operation modes.

In Chapter 4, an additional study was conducted to numerically represent a grass canopy using Direct Numerical Simulations. The simulation of various canopy density cases revealed that the canopy density highly affects the near-surface velocity profiles. With increasing density, the wind shear at the canopy top increases, while it decreases near the surface. Also, the drag force parameterization varied with canopy density, showing quadratic dependence on wind speed for sparse canopies and linear dependence for dense canopies. We diagnosed the so-called “effective mixing length”, a concept that is often used in model parameterizations of canopy, as to parameterize Reynolds stress. The mixing length scale exhibited a local maximum near half the canopy height and a local minimum near the canopy top. As such, these findings question the use of a ‘constant canopy mixing length’, as often assumed. Also, the locality of the vertical mixing

process can be questioned, where nonlocal sweeps and ejections can play a significant role (Chapter 2, 3).

The work in this thesis contributes to quantifying, understanding, and predicting the warming effects of wind machines in orchards. The data from the outdoor experiment can be used for future modeling studies to benchmark their results on field data. Likewise, the new numerical model can be used to explore various frost mitigation scenarios. In conclusion, this thesis provides valuable insights and practical recommendations for using wind machines to mitigate frost damage in agriculture. We hope the results and insights presented will aid farmers and the agricultural sector in effectively managing frost damage and enhancing crop protection.



# 摘要

霜冻是一种气象现象，会对农作物和果树造成严重损害，导致农业部门遭受巨大的经济损失。2017年的春季霜冻导致整个欧洲损失了3.3亿欧元。在2021年的法国，至少有一半葡萄园因霜冻事件而受损。由于全球变暖，花蕾绽放的时间往往提前，而在春季夜晚出现霜冻的概率却保持不变。因此，作物的脆弱期越来越多地与霜冻季节相重叠。洒水、风力机器和燃烧供暖等缓解霜冻的方法对于防止作物受损仍然至关重要。

在各种缓解霜冻的方法中，风机在成本效益和能源效率方面具有潜力。然而，人们对风机的增温效果以及增温过程背后的物理机制知之甚少。因此，本学位论文的主要动机是研究风机是否是未来减轻冻害的有效增温设备。然而，目前对机器增温的物理理解仍然有限。实验研究往往面临测量覆盖范围和分辨率的挑战，这些测量通常不足以充分捕捉风机激起的果园空气混合的时间和空间变化性。此外，现有的数值研究也很少。到目前为止，在湍流的热羽流与植物冠层结构之间动态相互作用的方面，以及果园中分布差异的植物-空气热交换的方面，还尚未进行过数值研究。

为了应对这些挑战，我们的研究结合了实验测量（第二章）和数值建模（第三章）。我们采用了分布式温度传感（DTS）技术来测量风机运行前后的空间和时间温度差异。分布式温度传感技术是一种基于光纤的传感技术，可沿光纤以较高的空间分辨率（采样间隔为0.25米）和时间分辨率（10秒）来测量温度。根据对6.75公顷范围内的准三维温度测量得出的物理见解，我们建立了一个数值模型，该模型模拟了风机对植物组织和近树冠空气的增温效应（第三章）。风机引起的强烈喷射运动是通过致动器参数化模型模拟的。为了结合果园冠层的影响，我们采用了冠层参数化模型。为了进一步诊断植物组织升温过程，我们将概念性的植物-空气热交换模型集成到了植被冠层模块中。从这些研究中我们发现：

- 第二章节：观察证据：我们提供了风机运行的确导致导致果树和近地表空气显著升温的观测证据。通过测量6.75公顷果园的准三维温度前后差异，我们发现局部逆温强度（ $8^{\circ}\text{C}$ ）在2.66公顷和0.45公顷范围内分别降低了30%和50%。在40分钟内，风机平均使植被树冠内的温度升高了3 K。据我们所知，第二章是首个通过高分辨率的测量量化了如此大面积范围内风机引起的增温效应的研究。
- 第二和第三章节：不可忽略的背景风效应：根据观测和数值模拟，我们发现即使是非常轻微的背景风（ $0.2\text{ m s}^{-1}$ ）也会导致风机上游与下游的空气和树叶升温效果存在显著差异。流体移动的效应导致在风机旋转的5分钟周期内出现了60米的“羽流位移”。风机的喷流与背景风之间的相互作用在下游形成波浪状图案，并在上游形成了气流对流。相比上游的升温范围（150米），下游的升温范围要远得多（550米）。在背景风的横向方向上，空气和树叶的增温范围每边大概是250米。

- 第二章节：通量传输：我们使用了所谓的四象限-孔方法分析量化了风机运行对垂直热通量传输的影响。运行期间的通量传输主要由下扫和上喷运动主导。暖空气的下沉和冷空气的上升流虽然是间歇性的，但在垂直热交换中非常有效。通过引发这些湍流下扫和上喷的运动，风机在增加植被树冠区域的温度以缓解霜冻损害方面非常有效。
- 第三章节：数值模型的开发：我们开发了一个数值模型来模拟风机对果园树冠的升温效果。该模型基于大涡模拟（LES）方法，结合了植被树冠模型、空气-植物组织热交换模型和风机模型。模拟结果与在9米高塔和6.75公顷果园上的水平测量平面上获取的测量结果进行了比较。数值模型很好地再现了风机运行在果园树冠中观察到的气混合和加热效果，为风机在果园中的操作提供了一个有用的室外实际替代模型。因此，该模型可以用于未来的敏感性和情景研究，以探索风机操作的优化方案。

在第四章中，我们还进行了另一项研究，我们使用直接数值模拟（DNS）来数值表示草地树冠。对不同树冠密度情况的模拟表明，树冠密度对近地表速度剖面有显著影响。随着密度增加，树冠顶部的风切变增加，而近地表的风切变则减小。此外，阻力参数化随着树冠密度的变化而变化，稀疏树冠的风速与阻力呈二次关系，而密集树冠则呈线性关系。我们诊断了所谓的“有效混合长度”，这是一个常用于树冠模型参数化中的概念，用来参数化雷诺应力。混合长度尺度在树冠高度的一半附近表现出局部最大值，而在树冠顶部附近表现出局部最小值。因此，这些发现质疑了常假设的“常数树冠混合长度”的使用。此外，垂直混合过程的局部性也值得质疑，其中非局部的下扫和上喷活动可能起着重要作用。

本学位论文的工作在量化、理解和预测风机在果园中的加热效果方面做出了贡献。户外实验的数据可以用于未来的建模研究，以基准化其结果与实地数据的比较。同样，新的数值模型可以用于探索各种霜冻缓解方案。总之，本论文为使用风机缓解农业中的霜冻损害提供了宝贵的见解和实际建议。我们希望本论文所呈现的结果和见解能帮助农民和农业部门有效管理霜冻损害并增强作物保护。

# 1

## INTRODUCTION



“Vineyards in France suffer at least €1 billion in damage after spring freeze; the biggest disaster in a quarter century say vintners” <sup>1</sup>

---

<sup>1</sup>This is a news article from [scott news](#) in 2017. Photo courtesy of Christian Hartmann.

## 1.1. FROST AND FROST MITIGATION

Technically, the word ‘frost’ refers to the formation of ice crystals on a surface (e.g., a car, ground, plant tissue) when the air cannot hold more moisture as the temperature decreases. In the context of agriculture, frost is a meteorological phenomenon that can cause significant damage to crops and fruit plants. During winter, frost events are common, and plants protect themselves by entering a dormant stage, a period of arrested growth. This natural defense mechanism prevents plant damage. However, in spring, plants resume growth and actively transport water and sugars, making them vulnerable to unexpected frost. Fruit frost damage occurs when ice crystals form on or within the plant tissues, disrupting cellular structure and leading to reduced crop yield and quality.

Spring frost events cause substantial economic damage to agricultural sectors. The 2007 spring frost in the US cost 2 billion dollars in the agricultural industry (Liu et al., 2018). In 2017, spring frosts across Europe caused 3.3 billion euros of losses (Lamichhane, 2021). In France, at least half of the 680 km<sup>2</sup> of vineyards were damaged due to frost events in 2021 (Liubchenkova, 2021). Frost events not only cause huge economic losses, but also have further implications on local communities and ecosystems. The farm workers (e.g., fruit pickers, processors) lose their jobs if there is zero or low yield (Snyder et al., 2005). Inouye, 2008 found that frost damage reduces the plant population and further affect pollinators, herbivores that rely on them. Furthermore, due to global warming, bud blooming tends to occur much earlier, while the probability of single frost nights in spring remains approximately the same (Liu et al., 2018; Siegmund, 2022). Consequently, there is an increasing exposure of crops to frost events, which makes frost mitigation more important than ever. Effective methods for frost damage mitigation remain essential to prevent crop damage.

Many passive and active methods are used to mitigate frost damage (Snyder et al., 2005). Passive methods include managing cold air drainage, grass removal, and planting frost-tolerant crops. Active methods include crop heating, sprinkling and air mixing by wind machine operations or by flying helicopters over the field.

### Passive methods:

- Cold air drainage: This method requires a rigorous study of the topography of the orchard to identify cold spots where cold air accumulates. Fruit trees are then planted in the relatively safe spots.
- Grass removal: Bare soil absorbs more heat during the day than a grass-covered surface (insulator). This heat is released during the night, helping to raise the temperature of the orchard.
- Planting frost-tolerant crops: Some crops are more resistant to frost than others. Planting frost-tolerant crops can reduce the risk of frost damage.

### Active methods:

- Heaters: Heaters increase the ambient temperature using warm air blowers or heat pots that warm the environment through radiation and convection. Although effective, heaters are costly, energy-intensive, and labor-intensive (See the cover of the introduction). Furthermore their efficiency is low because most heat is lost through buoyant convection into the open sky.

- Sprinkling: Increasing moisture in the air provides latent heat to plants when the water freezes on plants and reduces outgoing longwave radiation, helping to raise the temperature of the orchard. However, this method requires a large amount of high-quality water (Evans, 2000) and is labor intensive due to the frequent need to check the system.
- Helicopters: These mix warmer air from above with colder air near the surface. This method is effective but very expensive and consumes a lot of energy.
- Wind Machines: Wind Machines mix warmer air from above with colder air near the surface and machines are powered by the diesel engine. This method is automatic and requires very little labour and has the potential of being cost effective and energy-efficient, as it utilizes the thermal heat of the environment itself for crop warming.

Among various mitigation methods, wind machines are potentially cost-effective and energy-efficient. However, little is known about the warming effectiveness of wind machines and the physical mechanisms behind the warming process. Hence the general motivation of this thesis is to investigate whether wind machines are effective warming devices for future frost damage mitigation. We investigate this issue based on field experiments and numerical simulations. We aim to quantify the warming effects by measuring the temperature responses around the wind machine. Based on the physical insights from the field experiments, we aim to develop a numerical model that can simulate the warming effects of wind machines on plant tissue and near-canopy air. The combination of field experiments and numerical simulations will provide a general guideline for wind machine operations under different atmospheric conditions. The following Section 1.2 provides a brief historical review of wind machines for frost damage mitigation.

## 1.2. WIND MACHINES FOR FROST DAMAGE MITIGATION <sup>2</sup>

Since the 1950s, wind machines have been increasingly used in the agricultural community to mitigate the damage of frost events (Evans, 1999; Frith, 1951). A typical anti-frost wind machine comprises a large propeller with blades of  $\sim 5$ -meter diameter, a rotating hub, an engine to power the propeller, and a  $\sim 10$ -meter tower to support the propeller (Fig. 1.1). These anti-frost machines are theoretically designed to erode near-surface thermal inversions during radiative frost nights (Bates, Lombard, et al., 1978; Perry, 1998). During frost nights, the propeller thrusts large amounts of warm air downwards with a slight tilt angle to the horizontal. The warm jets create turbulent mixing along the angle of attack (Beyá-Marshall et al., 2019; Fisher, 2009). As the hub rotates, turbulent mixing erodes the inversion around the wind machine, mixing warm air aloft with colder air in the canopy. Consequently, the temperature of the affected air at canopy height rises significantly. Also, the vegetation warms as a result of the increased turbulent heat exchange between the plant tissue and the ambient air (Boekee et al., 2023).

Little is known about the warming effectiveness of the wind machines. Quantifying warming effects of the wind machines requires understanding the processes of vertical

<sup>2</sup>Parts of this section are based on Dai et al., 2023 and 2023

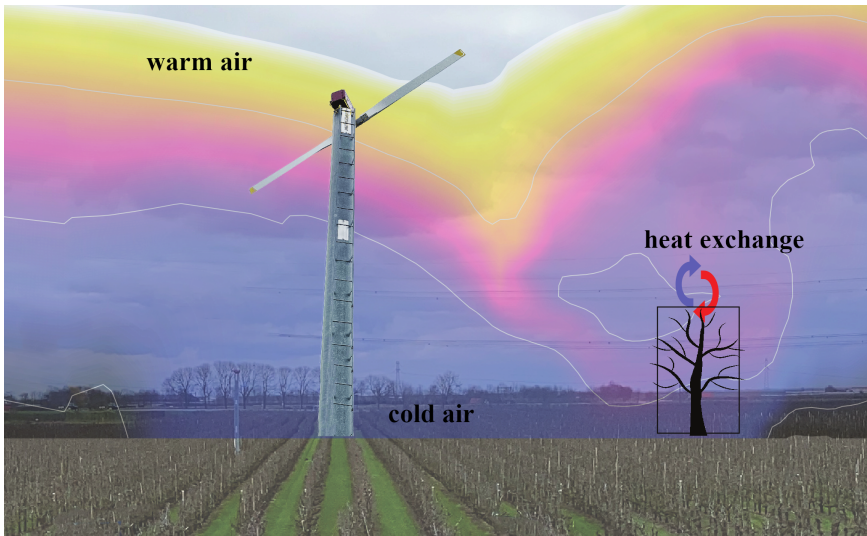


Figure 1.1: An 'artist impression' of frost mitigation by air mixing with a wind machine. The background colors represent different air temperatures layers, with the yellow color indicate the warmer temperatures. When warmer (less dense) air overlies colder (dense) air near the surface, we call this a 'temperature inversion'. This term is used because it is opposite to the daytime/normal temperature stratification with warm air near the ground driving thermal convection.

air-to-air mixing and local plant-air heat exchange. The air-to-air mixing effects highly depend on machine type (e.g., power, blades, hub height), operational settings (e.g., rotation period, tilting angle), and atmospheric conditions (e.g., inversion strength, ambient wind speed). Air-to-air mixing effects are spatially and temporally complex due to 360° rotation of the WM and interaction between the generated turbulent warming plumes and the non-uniform canopy structure. Locally, heat exchange processes depend on in-canopy air temperature, wind velocity and canopy characteristics. Furthermore, the distribution of mean wind and turbulence within the canopy airspace is also closely linked to the canopy structure and geometry. As a result, assessing the warming impact of the wind machines across the orchard is a challenging task.

Current physical understanding of machine-induced warming remains limited. Experimental studies often face challenges with the coverage and resolution of measurements, which are typically insufficient to fully capture the temporal and spatial variability of machine-induced air mixing in orchards (e.g., [Battany, 2012](#); [Beyá-Marshall et al., 2019](#); [Kimura et al., 2017](#); [Ribeiro et al., 2006](#)). Furthermore, there are only a few numerical studies available. The preliminary study of [Heusinkveld et al., 2020](#) in our group simulated machine-induced air mixing using an actuator disk model and estimated air warming based on Gaussian curve fittings. Yet their study did not incorporate canopy effects, such as canopy drag and canopy-air heat exchange. The dynamic interplay between turbulent warming plumes and canopy structure, as well as the heterogeneous plant-air heat exchange in the orchard, has not been investigated numerically so far.

### 1.3. RESEARCH TOOLS AND QUESTIONS

We address the above-mentioned challenges (Section 1.2) in terms of measurements (Chapter 2) and numerical modeling (Chapter 3). In addition to many meteorological observational instruments, we employed the technique of Distributed Temperature Sensing (DTS) to measure the spatial and temporal temperature responses before and after the wind machine operation. The DTS technique is a fiber optic-based sensing technique that can measure temperature at high spatial (sampling at 0.25 m) and temporal (10 s) resolution along the fiber optic cables. The detailed explanation of the DTS technique is provided in Section 2.1. Based on physical insights from quasi-3D temperature measurements over 6.75 ha, we developed a numerical model that simulates the warming effects of wind machines on plant tissues and near-canopy air (Chapter 3). The strong jet motions induced by the wind machine are simulated using an actuator disk parameterization model. To incorporate the effects of the orchard canopy, we employed a canopy parameterization model from E. G. Patton et al., 2016. To further diagnose the plant-tissue warming process, we integrated a conceptual plant-air heat exchange model developed in our group into the canopy module (Boeke et al., 2023). The detailed descriptions of the numerical model are provided in Section 3.2.

Based on the literature review of Section 1.2, research questions we address and corresponding chapters in this thesis are summarized as follows:

- are wind machines effective in warming fruit orchards and if so, can we measure the warming range and intensity? (Chapter 2)
- is the mixing and warming pattern different upwind and downwind from the wind machine, can we explain this difference? (Chapter 2 and 3)
- can we quantify the momentum and heat transport during wind machine operation? what are the main turbulent motions during operation? (Chapter 2)
- is it possible to build a numerical model of the full system, that is both realistic in comparison with observation, but also simple in its process descriptions? (Chapter 3)

In Chapter 3, the boundary condition of the ground surface is based on a simple energy balance closure. In reality, this boundary condition may be more complex due to the presence of orchard canopy and the land cover between fruit trees (e.g., grass, bare soil). The representation of the thermal properties of the surface grass layer may play a significant role in the orchard heat budget. However, very little is known about the air-plant exchange at the scale of this thin grass layer. Therefore, in Chapter 4, we explore whether direct numerical simulation of a thin grass layer is possible, so that in the future in-depth studies on grass thermodynamics are possible.

In Chapter 5 we reflect on the main findings and provide an outlook for further research.



# 2

## A QUANTITATIVE 3D INVESTIGATION BASED ON OBSERVATIONS



“I installed these wind machines to protect my crops from frost. They turn on automatically when the temperature drops below a certain level. But, I still come here every night to check if they are working”

Vogelaar, Fruit farmer  
05-07-2021, Krabbendijke

---

**The second chapter is based on the articles:**

Dai, Y., Boekee, J., Schilperoort, B., ten Veldhuis, M.-C., & van de Wiel, B. J. (2023). Wind machines for frost damage mitigation: A quantitative 3d investigation based on observations. *Agricultural and Forest Meteorology*, 338, 109522. <https://doi.org/10.1016/j.agrformet.2023.109522>

## 2.1. INTRODUCTION

Spring frost events have caused substantial economic losses in agricultural sectors. In 2017, spring frosts caused 3.3 billion euros of losses across Europe (Lamichhane, 2021). In France, at least half of the 680 km<sup>2</sup> of vineyards were damaged due to frost events in 2021 (Liubchenkova, 2021). Due to global warming, bud blooming tends to occur much earlier, while the probability of single frost nights in spring remains the same (Liu et al., 2018; Siegmund, 2022). Consequently, crop vulnerability is increasingly coinciding with the frost season. Effective methods (e.g., sprinkling, wind machines, paraffin pots) for frost mitigation remain essential to prevent crop damage.

Since the 1950s, wind machines have been increasingly used in the agricultural community to mitigate the damage of frost events (Evans, 1999; Frith, 1951). A typical anti-frost wind machine comprises a large propeller with blades of ~ 5-meter diameter, a rotating hub, an engine to power the propeller, and a ~ 10-meter tower to support the propeller. These anti-frost machines are theoretically designed to erode near-surface thermal inversion during radiative frost nights (Bates, Lombard, et al., 1978; Perry, 1998). During frost nights, the propeller thrusts large amounts of warm air downwards with a slight tilt angle to the horizontal. The warm jets create turbulent mixing along the angle of attack (Beyá-Marshall et al., 2019; Fisher, 2009). As the hub rotates, turbulent mixing erodes the inversion around the wind machine, mixing warm air aloft with colder air in the canopy. Consequently, the temperature of the affected air at canopy height rises significantly. Also, the vegetation warms as a result of the increased turbulent heat exchange (Boekee et al., 2023).

In practice, a general guideline for wind machine operations under different atmospheric conditions is yet to be developed. The difficulties are threefold. First, the magnitude and area of warming caused by machine operations are influenced by multiple factors. The warming effect is not only a function of the wind machine type (e.g., power, blades, hub height) but also depends on its operational settings (e.g., rotation period, tilting angle) and the atmospheric conditions (e.g., strength of local inversion, magnitude of wind drift) (See in Table 2.1). For example, Brooks et al., 1952 and Rhoades et al., 1955 found that a minimum power is required to break the inversion. The inversion strength, defined as the maximum temperature difference in the atmospheric surface layer, represents the maximum “heat reservoir” for wind machines to operate (Bates, Lombard, et al., 1978; Hu et al., 2018). Several studies attempted to relate the temperature response over the particular area of interest to the strength of the ambient temperature inversion near the surface (Davis, 1977; Goodall et al., 1957; Rhoades et al., 1955; Ribeiro et al., 2006). Second, in addition to the multi-factor scenarios mentioned above, warming due to air mixing under one machine type and condition exhibits a high degree of spatial-temporal variability. For example, the warming magnitude decreases with distance from the machine (Davis, 1977) and the affected area is non-symmetric due to background wind. Even with very light winds, this asymmetry can be significant as shown by Goodall et al., 1957 and Heusinkveld et al., 2020. Third, the complexities increase when a different indicator (e.g., plant temperature) is considered. The warming effects at the plant-scale depend on the heat exchange between air and plants. A detailed discussion on air-plant heat exchange during wind machine operation can be found in a companion study (Boekee et al., 2023). Our study will use air temperature as

Table 2.1: The warming effectiveness of horizontal-axis wind machines from previous studies. Note that N as Newton is unit of force. Please note the 50% warming in Heusinkveld et al., 2020 was the maximum relative warming, rather warming area in 3–5 ha.

Studies	Types of wind machine	Diameter of blade [m]	Hub height [m]	Tilting angle [°]	Rotation period [mins]	Inversion	Effectiveness		
							Defined range [m]	Strength [K]	Position / Area
Brooks et al., 1952	1068N thrust	2.74	9.75	7.5	4.5	2.1–12.2	3.3	at 2.1 m height, 36.5m downwind	42%
	4671N thrust	6.20					3.8	from 61 m upwind to 122 m downwind	29%
Rhoades et al., 1955	1246N thrust	2.70	12.80	7.5	4.0	3–15	3.30	no warming detected	0
	1512N thrust	3.7						0.73 ha	17%
Davis, 1977	Tropic Breeze Model S-391	5.30	10.40	7.0	4.5	1.5–18	6.40	3.4 ha; 2.1 ha; 0.8 ha	19%; 30%; 65%
Ribeiro et al., 2006	Mecagri 19 France	5.40	10.50	7.0	4.3	1.5–15	3.00	at 1.5 m height 30m away	67%
							1.70		41%
Battany, 2012	Portable Low Crop Model; two blades	5.00	5.90	6.0	4.5	1.1–10	1.85	at 1.1 m height 36 m away	80%
Beyá-Marshall et al., 2019	Gas V10 model, two solid fiberglass blades	6.00	10.67	6.0	4.5	1.5–15	3.50	at 1.5m height 5.30 ha; 2.67ha	30%; 50%
Heusinkveld et al., 2020	Orchard-Rite; double blades	5.00	10.50	7.0	5.0	1–10.5	3.00	at 1m height; 3–5 ha	50% (max)
The present study	Orchard-Rite; double blades	6.00	10.70	8.0	5.0	1–10.7	8.00	at 1m height; 0.46, 2.52ha	30%, 50%

the indicator for frost protection (Perry, 1998) and focus on the first two complexities.

We tackle the aforementioned complexities in two sequential studies. The present study measures the warming effects (i.e., magnitude and area) and the spatial-temporal variability of air warming under one machine operation and atmospheric condition. A sequel study simulates various potential machine operating scenarios numerically and assesses the impact of local warming effects. The criteria of this assessment are based on the physical insights obtained in this study.

Previous studies have quantified the warming effects by a single horizontal-axis wind machine (summarized in Table 2.1). The magnitude of warming (hereafter effectiveness) is often defined as the reduction of thermal inversion strength (Battany, 2012; Heusinkveld et al., 2020). Most studies estimated warming magnitude and area based on several point sensors (Brooks, Schultz, et al., 1958; Brooks et al., 1952), logging at coarse intervals (1954; Rhoades et al., 1955), and using interpolation (Beyá-Marshall et al., 2019; Goodall et al., 1957; Kimura et al., 2017; Ribeiro et al., 2006). Their estimations require further confirmation. The warming effectiveness depends on the interaction between the machine-ejected warming plumes and the surroundings (e.g., canopy, background wind) during 360° rotation. However, few studies have addressed the spatial-temporal variability of air mixing/warming processes or the shape of warming plumes. Using fiber optic cables, Heusinkveld et al., 2020 measured the evolution of warming plumes based on only one vertical and two horizontal profiles. They estimated the maximum warming magnitude and range based on curve fittings to a Gaussian model. While these studies provided insight into spatial-temporal variability of warming, a full picture of warming effectiveness requires measurements with wide coverage and high resolution. The underlying air mixing/warming processes remain poorly understood. Thus, the objectives of the present observational study are (1) quantifying the magnitude and area of air warming (effectiveness) by a wind machine; (2) identifying the characteristic mixing processes downwind and upwind; (3) quantifying the turbulent transport during

the machine operation, an aspect not addressed in previous studies.

The measurement technique used for quantification of air mixing/warming is so-called Distributed Temperature Sensing (DTS), consisting of a network of fiber optic cables. Fiber optic cables can measure the temperature at a high spatial (sampling at 0.25 m) and temporal (10 s) resolution. We aimed to obtain quasi-3D temperature responses caused by machine operation in a 6.75 ha orchard (details in Section 2.2). We deployed a total length of 9 km optic cable laid out in two horizontal planes at 1 and 2 m height above the ground surface, and three vertical profiles. To analyze the measured temperature responses, we selected the operation period (on mode) and reference period (off mode) based on the general weather conditions during the experiment (Sec. 2.3). The warming magnitude and area caused by air mixing are demonstrated in a time-averaged view (Sec. 2.3). The characteristic mixing processes downwind and upwind are identified in the view of vertical and horizontal temperature evolution (Sec. 2.3 and 2.3). Furthermore, the distribution of turbulent transport is quantified using Quadrant-Hole analysis at two points (Sec. 2.3). We obtain a three-dimensional view of temperature and flux responses caused by wind machine operation from the orchard scale to the point scale.

## 2.2. EXPERIMENTAL SETUP

### EXPERIMENT SITE AND WIND MACHINE

The field experiment was conducted on May 7–8, 2021, in a pear orchard in Krabbendijke, Zeeland, the Netherlands. Our experimental site (Fig. 2.1) is close to the site studied by 2020 yet in a different orchard block. The row orientation of the block is  $10^\circ$  West of North. The height of the trees and spacing of tree rows are 3 m. The tree rows 80 m west to the wind machine have double trees in one row, and others have single. In the center of the experimental block, a wind machine manufactured by Orchard-Rite was installed in November 2018. The hub height of this wind machine is 10.7 m. The rotor is composed of two straight blades and has a diameter of 6 m. A 126 KW engine Caterpillar 7.1 powered the propeller. When the wind machine operates, the rotor tilts  $8^\circ$  downward and rotates around its vertical axis with a user-specified period of 5 min.

### INSTRUMENTATION

This study used Distributed Temperature Sensing (DTS) technique to quantify the spatial and temporal variation of the temperature responses around the wind machine (Thomas et al., 2012). A typical DTS system consists of a laser controller, which shoots laser pulses through fiber-optic cables. The inhomogeneous properties of the cables result in different forms of scattering. The DTS machine can detect two distinct backscattered signals: Stokes and anti-Stokes scattering. The temperature of the cable sections can be estimated based on the intensity ratio of Stokes to anti-Stokes scattered signals after calibration to certain reference sections. The reference sections were submerged in two well-mixed cold and warm baths, and the temperature of these baths was tracked with two Pt100 temperature probes. A python package, dtscalibration v1.0.2 (B. F. des Tombe & Schilperoort, n.d.), was used to calibrate the measurements (B. des Tombe et al., 2020). A

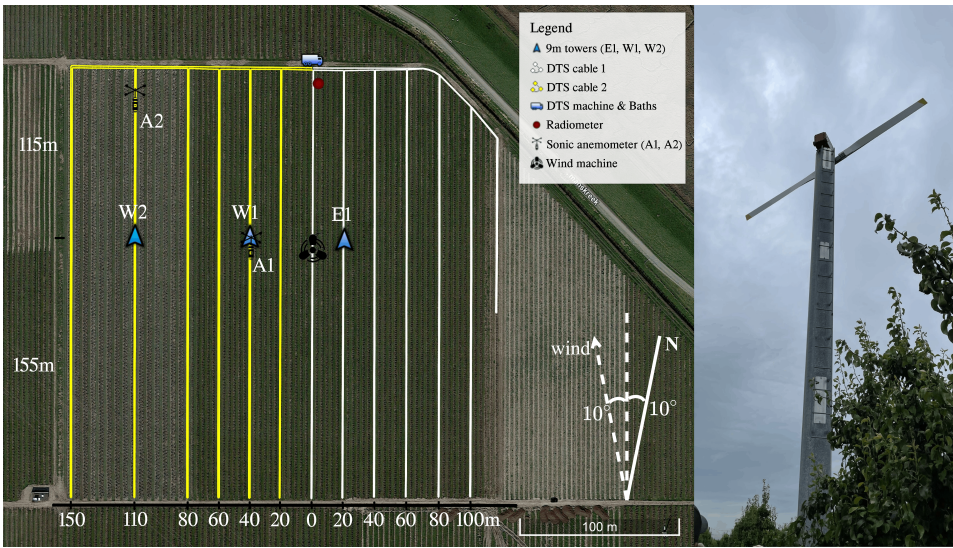


Figure 2.1: The top-down view of the experimental setup (left panel). The distance of the cables relative to the wind machine and the background wind direction are indicated. The same type of cables are indicated in two colors, each approximately 4.5 km. Note that in reality each line is doubled: at 1 and 2 m height above the surface. The tree rows 80 m west to the wind machine have double trees in one row, and others have single. The wind machine in the orchard (right panel).

double-end configuration was employed to better estimate uncertainty in (anti-) Stokes signals.

Fiber optical cables were connected to a Silixa Ultima-M DTS system. This system measured the cable temperatures with a reported sampling resolution of 25 cm. The integration time of measurement is set to 10 s.

In our setup depicted in Fig. 2.1, two fiber optic cables with a total length of 9 km and a diameter of 1.6 mm were installed along every seventh tree row to form horizontal planes at 1 and 2 m height. The horizontal spacing between the cables was 20 m, up to 30 and 40 m for the western most two rows (Fig. 2.1). In addition to horizontal planes, fiber optic cables were mounted to three 9m telescopic masts. Two vertical profiles were set up on 40m, 110m West of the wind machine (hereafter W1, W2), and one at 20 m East (hereafter E1). Through this DTS setup, a meshed grid over 6.75 ha is obtained with an along the cable resolution of 0.25 m. The accuracy of the cable temperature is 0.1 K. This setup ensures high spatial and temporal resolution of the temperature dynamics at the orchard scale.

In our study, air temperature dynamics are *approximated* using the measured cable temperature. During nighttime, cable temperature can be lower than the air temperature due to cable longwave radiation (Schilperoort et al., 2020). We argue that our findings based on the approximated air temperature hold because relative effects are examined. We provide an estimate of the potential errors of the approximation in A.1. The error of relative warming magnitude (an indicator defined in Sec. 2.3) lies within the

range of  $(-2.5\%, +4.5\%)$ .

In addition to the temperature measurements, two ultrasonic anemometers of model YOUNG 81000 were installed at 3 m height (Fig. 2.1, hereafter A1 and A2, A1 is the same position as W1). The anemometers logged the wind speed at 10 Hz with a resolution of  $0.01 \text{ ms}^{-1}$ . Based on the measurements from the anemometers, the distribution of the momentum and heat flux during the wind machine operation is quantified using Quadrant-Hole analysis (more detail in A.2). Furthermore, the incoming and outgoing short- and longwave radiation were measured using a CNR4 radiometer (Kipp & Zonen) installed at 2 m height (See Fig. 2.1).

## 2.3. RESULTS AND DISCUSSION

### GENERAL WEATHER CONDITIONS AND WIND MACHINE OPERATION

Prior to discussing the temperature responses caused by the operation, it is important to detail the weather conditions during the experiment. A diurnal temperature cycle of about  $12^\circ\text{C}$  was reported by an undisturbed weather station 1 km from the experimental orchard (not shown in the setup Fig. 2.1). During the day, the 1.5 m air temperature rose to  $15^\circ\text{C}$  due to clear sky solar radiation. After sunset, the temperature started to cool rapidly. With near-freezing temperature, the machine started warming up at 23:00 hours (with two initial cycles) and operated at full power from 23:40 hours for 80 minutes. In the later stage of operation, some thin clouds passed over the orchard. In Fig. 2.2, these clouds are indicated by the large fluctuations in net longwave radiation. To avoid the influence of clouds, the first part of the operation period (23:40–00:20, dashed lines in Fig. 2.2) is selected as “on” mode. During this period, minor fluctuations in the net radiation result from the period canopy warming by the wind machine. The period prior to operation between 22:20–23:00 is selected as undisturbed “off” mode (also shown in Fig. 2.6). Throughout the experiment, the background wind velocities were below  $0.3 \text{ ms}^{-1}$ , measured at 3 m height, wind direction South-East. The average relative humidity was 90%.

### AIR MIXING EFFECTS IN A TIME-AVERAGED VIEW

Figure 2.3 presents the mean and spread of the temperature profiles before (off mode) and during (on mode) wind machine operation. The impact of machine operation is clearly visible in the vertical temperature profile at tower W1 (Fig. 2.3a) and the horizontal temperature distribution along the background wind direction (Fig. 2.3b). In Fig. 2.3a, prior to the operation, a strong inversion of 8 K near the canopy top formed due to radiative cooling of the ground surface. The uniform temperatures within the canopy (0–2.5 m) are likely a result of radiative energy redistribution. During operation, the strong inversion was eroded by turbulent mixing, resulting in a relatively uniform vertical temperature profile. Due to periodic rotation, the spread around the mean increased in on-mode as air mixing at the sensor varied over time. The average in-canopy temperature increment induced by air mixing amounted to 3 degrees over 40 minutes. A similar change in the shape of the vertical profile was found by Heusinkveld et al., 2020,

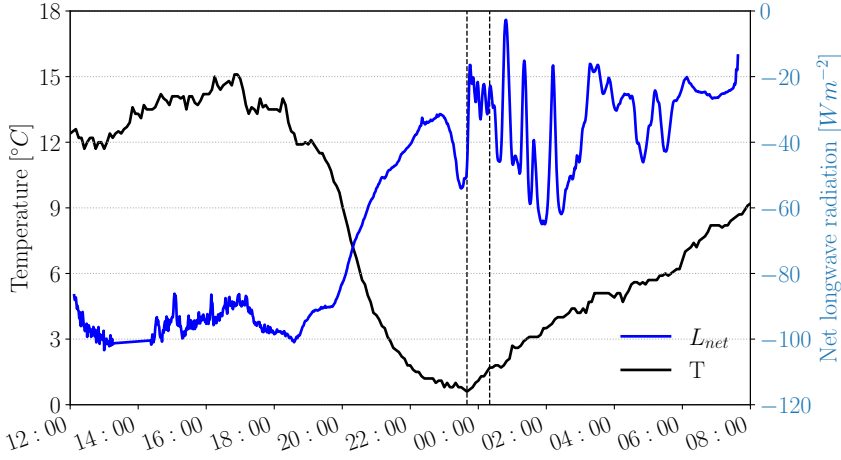


Figure 2.2: Diurnal temperature cycle (black line) measured at 1.5 m height by an undisturbed weather station. Please note the observed temperature after midnight rose. The net radiative budget (blue line) on May 7–8 observed by 3 m radiometer. The selected operation period of the wind machine is indicated with the dashed lines.

although the shape change at the canopy top was less pronounced. Their experiment was conducted in wintertime, within a bare canopy. As a result, the initial inversion at the top of the canopy is much weaker than in our case, which is more typical for late spring conditions.

The horizontal distribution of temperatures at 2 m along the background wind direction shows a strong asymmetry in Fig. 2.3b. We attribute this to background wind advection, with a maximum velocity of  $0.30\text{ms}^{-1}$ . The maximum warming spot at 2 m height drifted 50 m downwind. This is explained by the mass, momentum and heat advection by background wind during the rotation. In a 5 minutes revolution of the turbulent jet, the background air mass at 3 m height has been replaced over a maximum distance of 90 m. Interestingly, it can be observed that even in off mode (blue) the temperature along the horizontal is nonuniform over the field. This can be caused by either local field properties or by non-uniform surroundings. A relatively higher temperature around the orchard edges might be caused by local heat exchange from the sides, although this is difficult to substantiate with our data. The sudden peak at 70m downwind likely resulted from the planting arrangement in double-tree rows.

As different studies on air mixing by wind machines are subjected to different background inversions, usually the *normalized warming* (NW)  $\Delta T / \Delta T_{\max}$  in Eq. 2.1 is considered to quantify the temperature responses. It is the ratio between the actual temperature increment induced by the wind machine ( $\Delta T$ ) and the maximum increment ( $\Delta T_{\max}$ ) that can be ideally achieved (Beyá-Marshall et al., 2019; Heusinkveld et al., 2020).

$$\frac{\Delta T}{\Delta T_{\max}} = \frac{[T_{on}(\vec{r}, h, t) - T_{off}(\vec{r}, h, t)] - [T_{on,ref}(h, t) - T_{off,ref}(h, t)]}{T_{hub} - T_{off}(\vec{r}, h, t)} \quad (2.1)$$

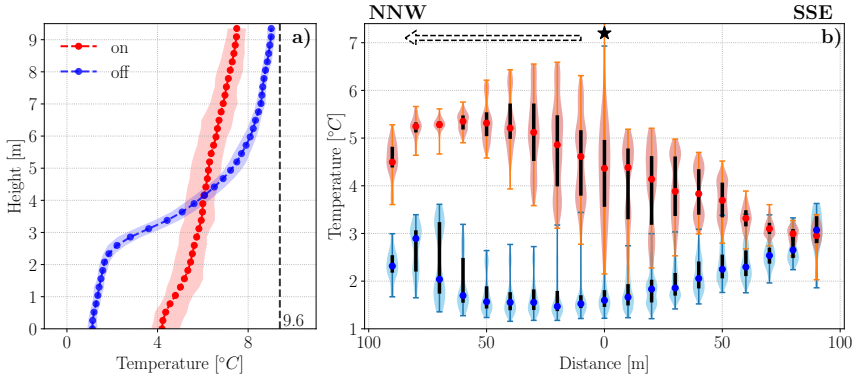


Figure 2.3: **a** The mean and spread of vertical temperature profile during the 40 minutes of on (red) and off (blue) mode at tower W1. The dashed line indicates the extrapolated temperature  $9.6^{\circ}\text{C}$  at hub height 10.7 m. **b** The on (red) and off (blue) mode horizontal temperature distribution at 2 m height along the direction of the background wind, which is indicated by a dashed arrow (SSE to NNW). The distance is relative to wind machine location (black star). The median temperature is marked with dots. The 25% and 75% percentiles are indicated with black solid lines.

where  $h$  is the height and  $\vec{r}$  is horizontal location vector. The normalizer  $\Delta T_{\max}$  is compared to the temperature at hub height,  $T_{hub}$ . In Fig. 2.3a,  $\Delta T_{\max}$  is the difference between the black dashed line  $T_{hub}$  and the blue dotted line  $T_{off}$ .  $\Delta T$  is the difference between the red and blue dotted lines. However, the temperature difference between these two modes might result from the warming by air mixing and (or) the nighttime cooling. To compute the actual temperature responses by the wind machine, the overall nighttime cooling trend needs to be accounted for. The cooling effects over the field are corrected by subtracting the temperature difference in the reference section  $[T_{on,ref}(h, t) - T_{off,ref}(h, t)]$ . In our case, the reference section is chosen as the undisturbed cable section at the southeast corner.

Fig. 2.4 shows horizontal contours of the *normalized warming* during operation. The contours are averaged over a 40 minutes operation period. To the best of our knowledge, the present study is the first to measure a full picture of warming effectiveness with a high resolution over such a large area. Normalized warming  $\geq 50\%$  is achieved over an area of 0.42 and 0.46 ha at 2 and 1 m height, respectively. For 30% normalized warming, the area extends to 2.81 and 2.52 ha, respectively. The coverage area is comparable smaller than reported in the literature (See Table 2.1) due to the exceptionally large inversion strength (8 K) in our measurement night. The non-symmetrical shape of the averaged warming plume is explained by the background wind drifting, resulting in a larger warming area downwind. The drifting effect is more pronounced at 2 m, closer to the top of the canopy.

The relationship between the *normalized warming* and the corresponding warming area is summarized in Fig. 2.5. As expected, the cumulative warming area monotonically decreases with increasing warming magnitude. Note that the definition of Eq. 2.1 (illustrated in Fig. 2.3) prevents a normalized warming of 100% even in case of perfect mixing. This is due to the fact that the canopy temperature can never reach the hub

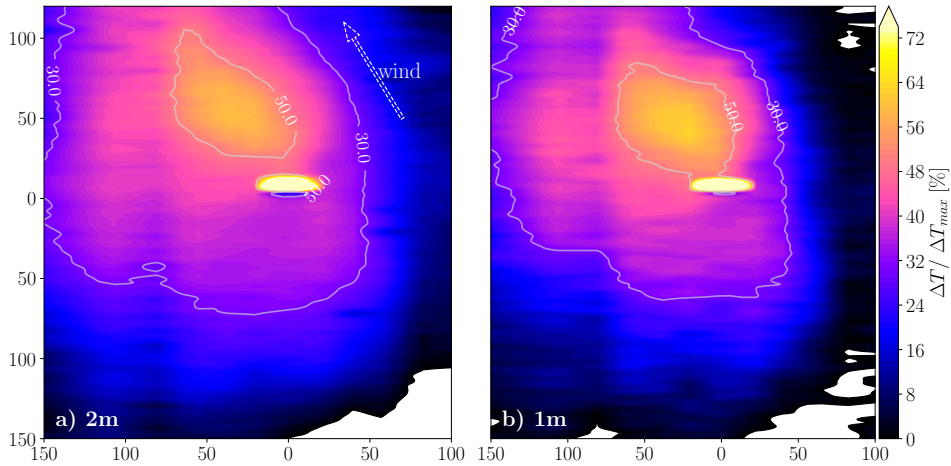


Figure 2.4: Planar view of the time-averaged normalized warming in the upper and lower canopy at 2 and 1 m height. The *normalized warming* contours of 50% and 30% are indicated with white contour lines. The wind machine was located in the middle of the field, where the high temperature spot was. This is caused by the heat and radiation emission of the machine engine. The background wind direction is indicated with the white dashed arrow (maximum 0.30 m/s at 3 m).

height temperature as the cold air below is thermodynamically distributed over the lowest 10 m. Hence, the after-mixing temperature will always be lower than the initial hub height temperature. The warming area at two heights was similar for higher warming magnitudes ( $\geq 35\%$ ). For relative lower warming, a larger area is affected at 2m. This is expected because the plume has to penetrate from above. Since our DTS network does not fully cover the warming plume (see 30% contour line in Fig. 2.4), the areas of normalized warming below 30% are slightly underestimated.

### AIR MIXING PROCESSES: VERTICAL TEMPERATURE EVOLUTION

The temperature time series at 1 and 9 m height of tower W1 are shown in Fig. 2.6a and the corresponding temporal variation of the profile is shown in Fig. 2.6b. During off mode, a strong thermal inversion is established, with sharp gradient at the canopy top (see also Fig. 2.3). The formation of the cold canopy layer prior to motor operation likely results from longwave cooling redistribution by the tree elements and blocked turbulent exchange with the 'open air' due to tree confinement. Next, as the temperature approached the freezing point, the machines started to operate in an intermittent (warm-up) mode. The warming effect of the first two rotations is remarkably strong, with instantaneous warming of 4 and 6 °C during the first and second cycle. The relatively warmer plumes originate from the undisturbed warmer air at the upper height. After the start-up mode, the wind machine entered the full operation mode and started rotating. Now the air is mixed each time the jet passes by. As a result, the temperature becomes more uniform (Fig. 2.6a): the air temperature within the canopy increases at the expense of the air above the canopy. Furthermore, Figure 2.6a (blue line) shows that

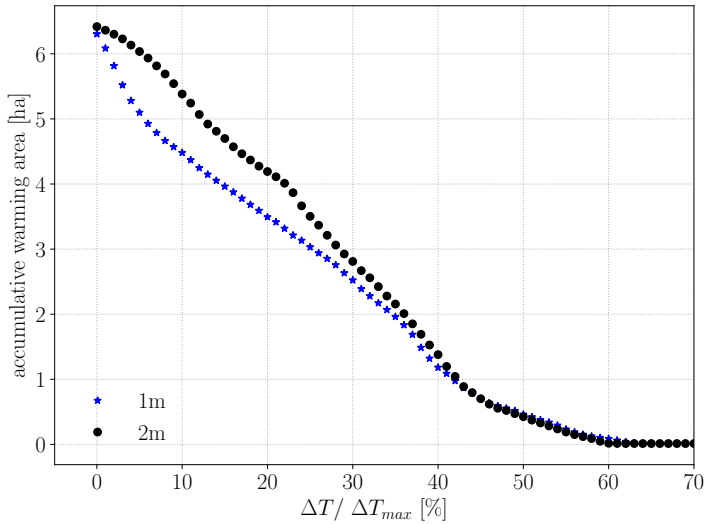


Figure 2.5: The relationship between time-averaged *normalized warming* and accumulative warming area at two heights. Notice that the results for the different heights are comparable, with the warmed area a little larger at 2m.

the rotation time is short enough to keep the in-canopy temperatures above  $5^{\circ}\text{C}$  for the remaining period.

Phase-averaged temperature profiles at three towers are shown in Fig. 2.7. These profiles are aligned relative to the time of wind machine jet passage, when the maximum wind velocity occurs. When the jets blow against the background wind at tower E1, the warming plumes arrive after jet passage. This delay time is probably caused by the wind drag. In contrast, the downwind masts (W1, W2) experience warming before the jet (core) arrives. We attributed this early warming to the advection of earlier warmed sections. As a result of advection, the warming magnitude is larger at tower W1 than at E1, even though tower E1 is closer to the wind machine. This difference indicates the plumes penetrate deeper and get better mixed along the background wind direction. In contrast to the downwind area, the warming plumes upwind (tower E1) were *uplifted* by the weak background wind (flow convergence). Furthermore, a second warming plume seems to develop right after the central plume at E1 (black dashed line in Fig. 2.7a). This secondary warming plume indicates the formation of turbulent vortices, which act to recirculate the uplifted warming plumes down. Those effects were found in numerical simulations of the present case, which will be presented in follow-up work.

The spatial-temporal autocorrelation function is used to detect the thermal periodicity and coherence induced by the wind machine. By definition, the self-correlation function characterizes the spatial and temporal similarity of the observations with its

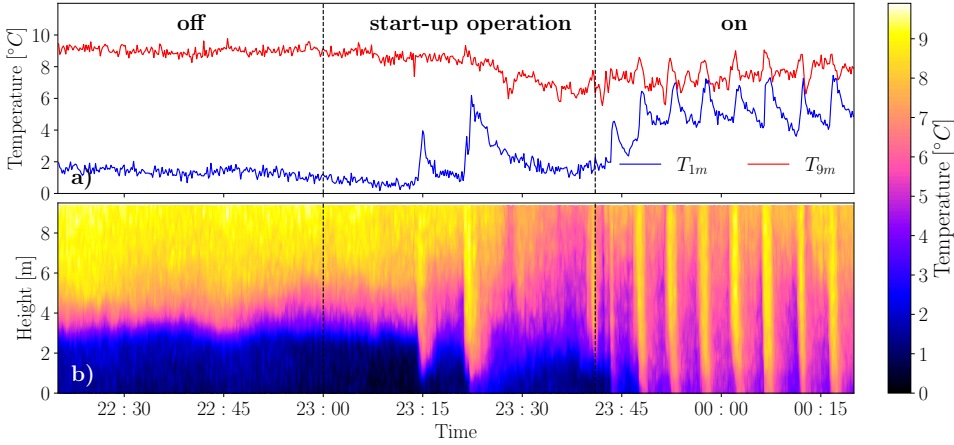


Figure 2.6: **a** The time series of the 9 m and 1 m temperature at tower W1. **b** The contour plot of temporal temperature variation at tower W1. Three phases of the wind machine operation are indicated: off, start-up operation (intermittent), and fully on period.

delayed copy. The normalized correlation function for a variable  $\varphi$  is defined as

$$R(\Delta x, \Delta t) = \frac{\overline{\varphi'(x, t)\varphi'(x + \Delta x, t + \Delta t)}}{\sqrt{\overline{\varphi'(x, t)^2}} \cdot \sqrt{\overline{\varphi'(x + \Delta x, t + \Delta t)^2}}} \quad (2.2)$$

Where  $\varphi'(x, t)$  is the fluctuation with respect to the mean of quantity  $\varphi(x, t)$ . The autocorrelation of the temperature time series gives information about the structure of thermal plumes. Furthermore, the integral time scale  $T_{int}$  in Eq. 2.3 can be estimated by integrating the correlation coefficient at a fixed location  $R(\Delta x = 0, \Delta t)$  with respect to the time lag  $\Delta t$  direction.

$$T_{int} = \int_0^{\infty} R(\Delta x = 0, \Delta t) d\Delta t \quad (2.3)$$

As to avoid the periodic influence of the wind machine,  $T_{int}$  here is approximated with the integral up to the first zero-crossing point.  $T_{int}$  indicates the characteristic decorrelation time at one measurement point (Oliver, 2012). Specifically in this study, it is the characteristic travelling time of the dominant features through the measurement points.

In this study, temperature time series at each height during the operation (on-period in Fig. 2.6) are taken as input for the autocorrelation function (Eq. 2.2). Fig. 2.8 shows the contours of the correlation coefficient at three towers. Larger absolute correlation coefficients indicate stronger periodicity. Hence, the color's shade represents the strength of the autocorrelation, indicating the rotating plumes' periodic effects. As depicted in Fig. 2.8bc, the clear periodicity in the downwind western masts directly results from the wind machine operation. In contrast, the periodicity on eastern mast is absent at higher

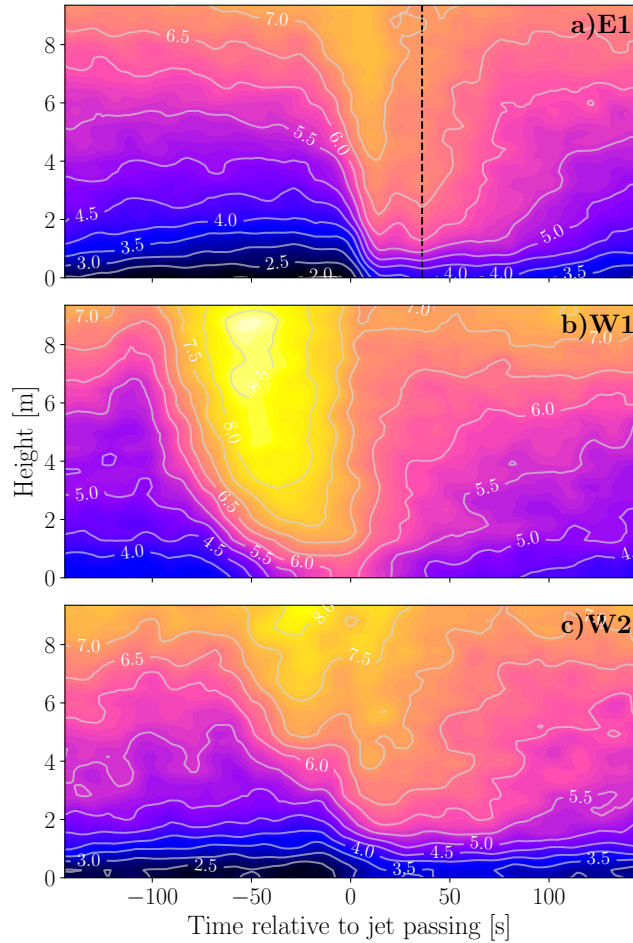


Figure 2.7: As a function of time: the phase-averaged temperature profile at tower **a** E1, **b** W1, and **c** W2. The temperature magnitude is indicated by the contour lines and the labels. The dashed black line in **a** indicates the formation of a secondary warming plume.

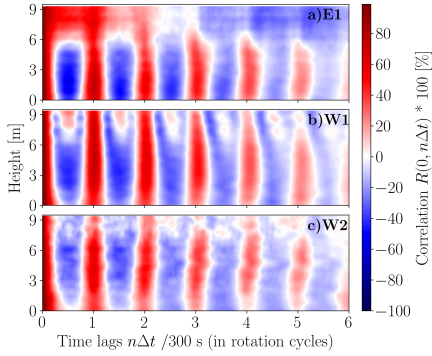


Figure 2.8: The contours of the correlation coefficient for all height along the towers

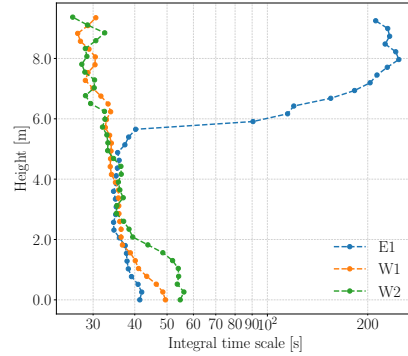


Figure 2.9: The profiles of the integral time scale  $T_{\text{int}}$  at three towers.

heights (Fig. 2.8a). This disparity might be attributable to the plumes blowing against the background wind. We speculate that the ambient wind uplifts and recirculates these warm plumes. As also shown earlier (Fig. 2.7a), the formation of the second warming plume was found in the phase-averaged temperature signals. The autocorrelation function did not clearly detect these circulated plumes near E1, likely due to its irregular pattern and relative low-temperature magnitude at higher heights. Signs of similar vortex-wave structures were detected further downwind. These signs are apparent in Fig. 2.8bc but obscured in Fig. 2.7bc. At the higher height of W1, for example, the warming waves recurred at half of the rotation cycle. At 110m downwind (Tower W2), the signals of the warming plumes and recirculated vortex were both weakened because of diffusion over distance.

The integral time scale is calculated from Eq. 2.3, by integrating  $R(\Delta x = 0, \Delta t)$  up to the first zero-crossing point (See Fig. 2.8). Fig. 2.9 shows the profiles of the integral time scale at three towers. The integral time scale gives an indication of the contacting time of the rotating warming plume at the measurement points. Here this characteristic contact time seems to be around 36 seconds. The integral time scale had similar profiles downwind (W1, W2) except for the region within the canopy (lower 3 m). The traveling speed of thermal plumes slowed down from top to bottom due to vertical momentum diffusion (canopy drag). The thermal plumes at W1 traveled faster than at W2 because warm plumes diffused/broadened over distance. For the tower upwind (E1), a similar behaviour is observed below 6 m. However, higher up at E1, the integral time scale was particularly large due to non-periodic mixing.

### AIR MIXING PROCESSES: HORIZONTAL TEMPERATURE DISTRIBUTION

Where an overall time-averaged perspective of warming plumes is presented in Fig. 2.4, instantaneous movies of the warming plume show an interesting spiral type of behavior (shown in supplementary material). Here, snapshots of warming plumes are *phase-averaged* to emphasize statistical significance. Four representative moments (jets downwind, upwind, left, and right cross-wind) of the phase-averaged *normalized warming* are

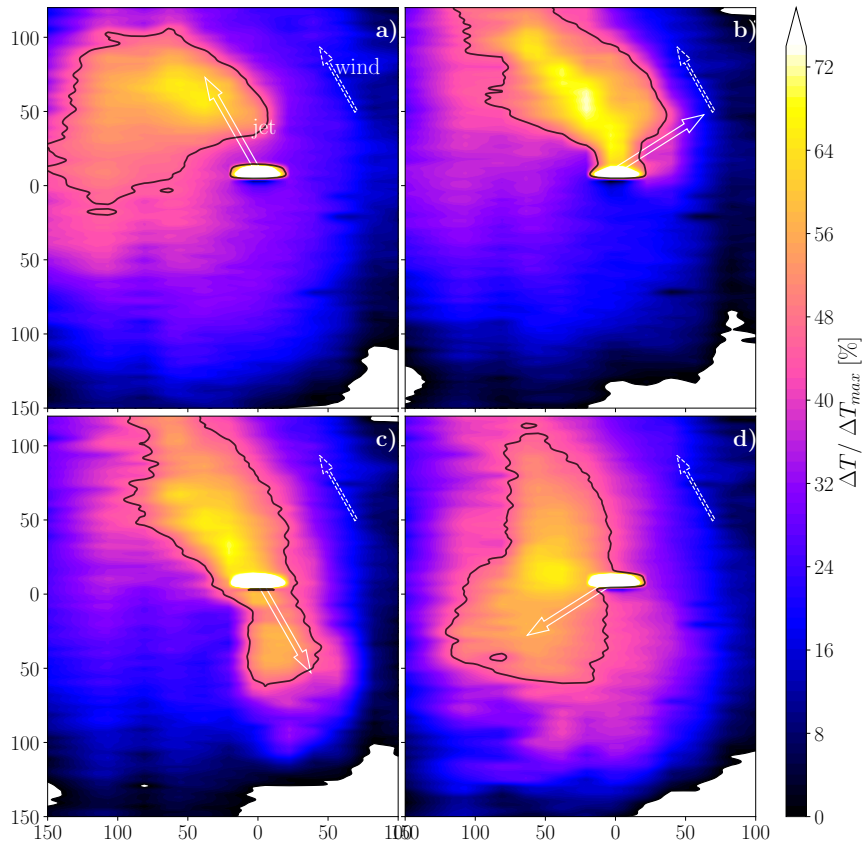


Figure 2.10: Four moments of the phase-averaged *normalized warming* at 2 m height: jet (large white arrow) **a** downwind, **c** upwind, **b** right and **d** left of the cross-wind relative to the background wind direction (small dashed arrow). The black contour line indicates a 45% reduction of the ambient inversion.

displayed in Fig. 2.10. The shape of the warming plumes was initially hypothesized to be a spiral (Brooks et al., 1952) and later on an expanding toroidal ring (Brooks, Schultz, et al., 1958). When the jet blows along the background wind, the shape of the warming plume likely matches the shape of a spiral. In other cases, we observed that the plume shape was distorted by the background wind and the warming air was drifted downwind. As a result, warming plume tends to accumulate downwind, resulting in a larger warming area. Furthermore, there is a time delay between the wind jet and the warming plume due to background wind. This delay feature was also shown in Fig. 2.7.

To show the mixing processes along the horizontal profiles, Fig. 2.11 documents the temporal variation of the normalized warming along and across the background wind direction, respectively. On top of the temporal variation plots, the integral time scale is plotted as a function of distance. Based on Fig. 2.11a, the influenced distance ranged from 80 m upwind to more than 130 m downwind. The relatively larger time scale down-

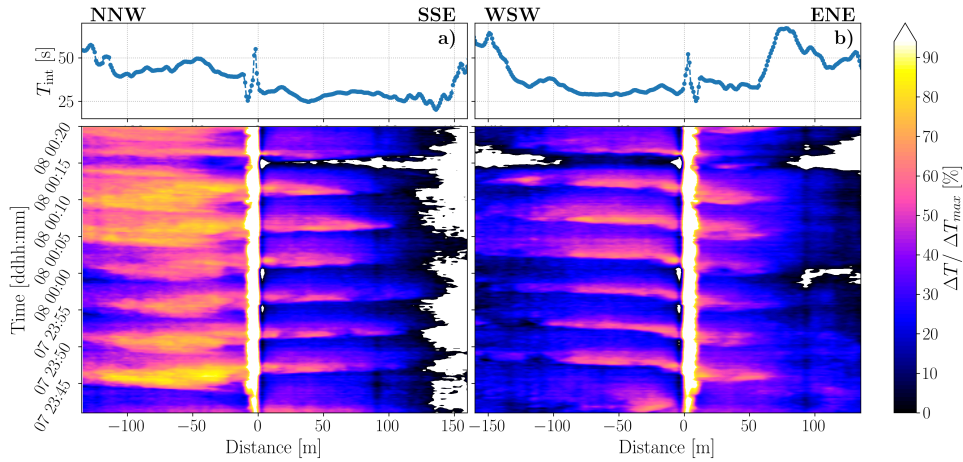


Figure 2.11: Left panel: **a** Along the wind direction: normalized warming. Right panel **b** Across the wind direction: normalized warming. In the upper panel the integral time scale as a function of distance is displayed (Eq. 2.3).

wind is the result of slow and irregular plume accumulation due to horizontal advection. Along the cross-wind direction, the warming plumes cover the range of 120 m left to 60 m right. We attribute this cross-wind asymmetry to the rotation direction of the wind machine. When the plume reaches the leftmost side, the plume prior to this time-step undergoes an acceleration process. This results in a longer reaching distance to the left. Conversely, the plume is decelerating before the plume reaches the far right and therefore has a relatively short reaching distance.

### AIR MIXING PROCESSES: TURBULENT TRANSPORT DISTRIBUTION

To characterize local air mixing processes, so-called Quadrant-Hole (hereafter QH) analysis is performed on the turbulent flux. Specifically, we use QH analysis to compare the relative distribution of vertical momentum and heat fluxes before and after the wind machine operation at two anemometer locations (Fig. 2.1, A1 and A2). The technique of QH analysis has been used in canopy studies to investigate the turbulent transport of momentum, heat, and moisture (see a list of applications in Brunet, 2020, Chapter 3.1). Since the method of QH analysis is well described in the literature (Lu & Willmarth, 1973; Yue et al., 2007), we succinctly illustrate it here with an example. More details can be found in A.2.

In Fig. A.1, the events of x-component momentum flux defined by QH are “outward interaction” (Q1), “ejections” (Q2), “inwards interaction” (Q3), and “sweeps” (Q4), respectively. For instance, the sweep events are characterized by fast air parcels ( $u' > 0$ ) transporting downwards ( $w' < 0$ ). The events of heat flux in Q1, Q2, Q3, and Q4 are defined as “warm updraft”, “cool updraft”, “cool downdraft”, and “warm downdraft”, respectively. The flux values in each quadrant are sampled with H-th percentile of its distribution. As the hole size H increases, the flux events are more extreme and its frequency

Table 2.2: Parameters related to the Quadrant-Hole analysis for sensible heat flux at sonic anemometers A1 and A2.

Cases	A1-on	A1-off	A2-on	A2-off
$(S_{2,0} + S_{4,0}) / (S_{1,0} + S_{3,0})$	1.81	1.62	3.99	0.82
$S_{4,0} / S_{2,0}$	1.25	1.02	1.41	1.04
$H'$	3.1	3.1	3.0	2.0
$\sum_{i=1}^4 t_{i,H'}$	0.069	0.078	0.078	0.136
$S_{4,H'} / S_{2,H'}$	2.23	1.21	1.99	0.67

decreases. The intensity and frequency of flux events are quantified using the *value fraction*  $S_{i,H}$  and *duration fraction*  $t_{i,H}$ , respectively (A.2).

The *values fraction*  $S_{i,H}$  is computed in the on and off mode. Fig. 2.12 presents the *values fraction* of sensible heat flux (upper panel) and x-component momentum flux (lower panel) at the positions A1 (left panel) and A2 (right panel) (Fig. 2.1). For sensible heat flux (upper panel) during the operation, a larger proportion of warm downdraft motions (Q4) contributed to the total heat transport at both A1 and A2. This is due to the fact that the jet is included slightly downward and also likely due to (KH-type of) flow instabilities induced by the jet. For cool updraft motions (Q2), the relative ratio increased in A2 and decreased in A1. As A1 is closer to the machine, one speculation is that the air plumes perceived at A1 diffused less and still kept the direction of the rotor (i.e., 8° downward tilting). Then, there is relatively less contribution of cold updraft motion at A1.

The motions of warm downdraft and cool updraft can be beneficial for the erosion of thermal inversion. The parameter  $(S_{2,0} + S_{4,0}) / (S_{1,0} + S_{3,0})$  in Table 2.2 indicates the ratio between stratification eroding (Q2 and Q4) and stratification restoring (Q1 and Q3) motions. It is not surprising that  $(S_{2,0} + S_{4,0}) / (S_{1,0} + S_{3,0})$  was more significant during the on mode. Furthermore, the warm downdraft motions ( $S_{4,0}$ ) contributed more than the motions of cool updraft ( $S_{2,0}$ ) during the on mode at both positions. This higher proportion becomes more pronounced when only the most intensive events are considered ( $S_{4,H'} / S_{2,H'}$ ), where  $H'$  is the hole size where half of the flux occurs. The heat flux with a magnitude larger than hole size  $H' > 3$  accounted for only 7 % of the time ( $\sum_{i=1}^4 t_{i,H'}$ ). The distribution indicates that the heat transport processes caused by wind machine operation are efficient and intermittent. Similar conclusions were drawn in the presence of canopy (Raupach, 1981; Raupach et al., 1986).

Since the findings of momentum flux are quite similar to heat flux, we will discuss it succinctly. During wind machine operation, the motions of sweeping and ejection ( $(S_{2,0} + S_{4,0}) / (S_{1,0} + S_{3,0})$  in Table 2.3) dominated the momentum transport. There appears to be a strong similarity between the behaviour of downward heat and momentum fluxes. Due to the machine operation, the air mixing processes mainly developed with fast air parcels sweeping downward and slow air parcels ejecting upward. Correspondingly, in the presence of inversion, there are downdrafts of warm air and updrafts of cool air. In summary: the Quadrant-Hole analysis shows that there is a dominant role of

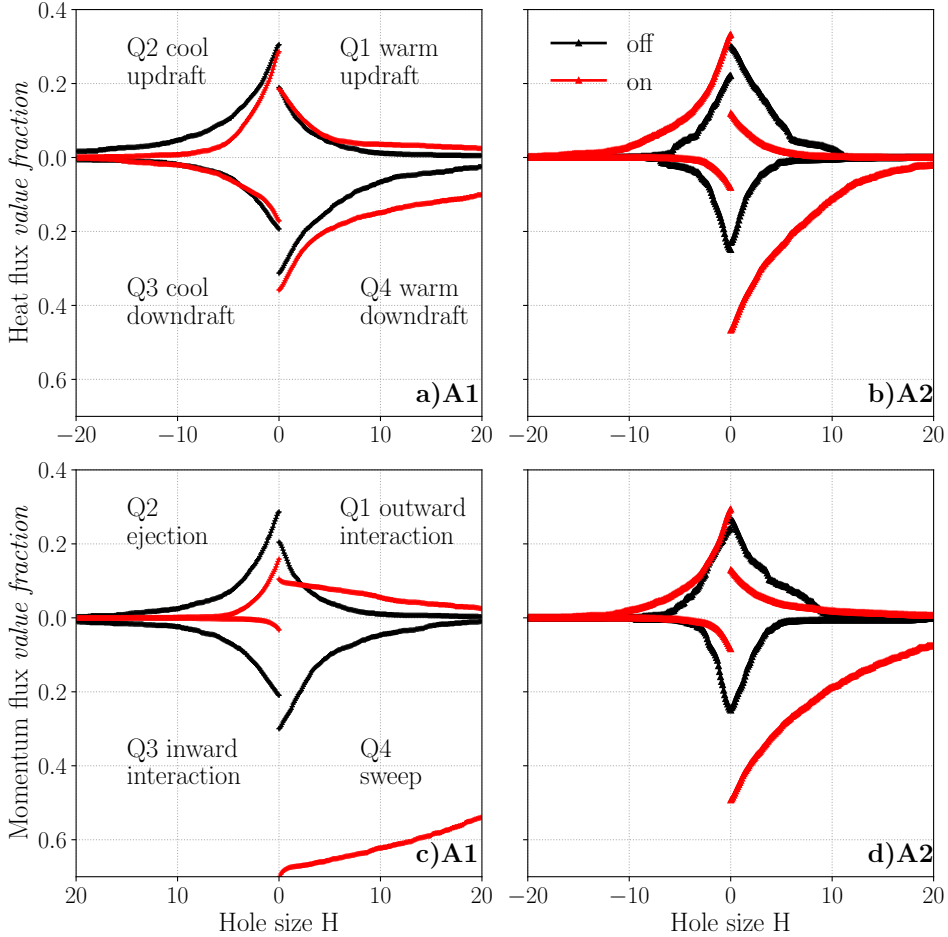


Figure 2.12: The quadrant analysis of *value fraction* of the heat flux (upper panel) and momentum flux (lower panel) at positions of sonic anemometers A1 (left panel) and A2 (right panel). The red and black lines represent the on and off mode respectively.

Table 2.3: Parameters related to the Quadrant-Hole analysis for momentum flux (x-component) at sonic anemometers A1 and A2. Note that there were no ejections larger than half the hole size for S1 during on mode, which results in an infinite  $S_{4,H'}/S_{2,H'}$ .

Cases	A1-on	A1-off	A2-on	A2-off
$(S_{2,0} + S_{4,0}) / (S_{1,0} + S_{3,0})$	6.28	1.41	3.69	0.94
$S_{4,0}/S_{2,0}$	4.44	1.05	1.68	1.01
$H'$	19.9	2.7	3.6	2.0
$\sum_{i=1}^4 t_{i,H'}$	0.011	0.094	0.061	0.145
$S_{4,H'}/S_{2,H'}$	inf	1.27	3.30	0.72

wind-machine-induced downward sweeps in transporting both heat and momentum.

## 2.4. CONCLUSION

The present study aims to quantify the warming effects (i.e., magnitude and area) of wind-machine induced air mixing, identify the characteristic mixing processes downwind and upwind, and quantify the turbulent flux during the wind machine operation. Using a total length of 9 km fiber optic cable, we measured quasi-3D temperature responses at 25 cm sampling and 10 s temporal resolution over a 6.75 ha orchard. We summarized the characteristics of air mixing in a time-averaged and an instantaneous view. The flux distribution caused by wind machine is quantified using Quadrant-Hole analysis. We conclude:

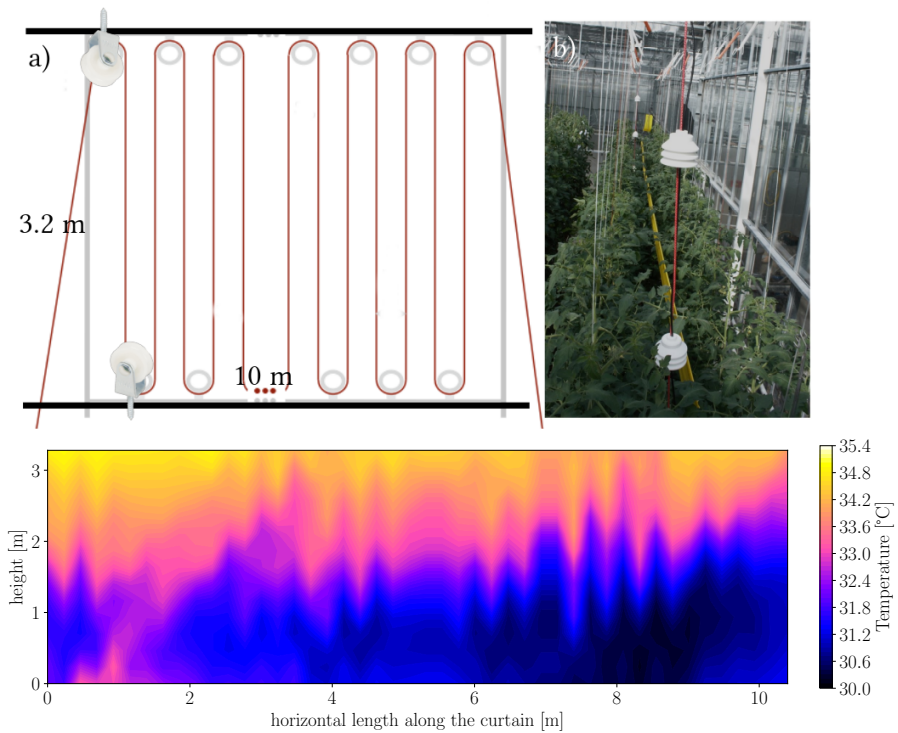
- The warming effects caused by wind-machine induced air mixing shows a high degree of spatial-temporal variability. We found a 50% reduction of the local inversion strength ( $8^{\circ}\text{C}$ ) over 0.42 ha at 1 m and 0.46 ha at 2 m height. For a 30% reduction, the coverage area spread to 2.81 and 2.52 ha, respectively. On average, wind machine operation raised in-canopy temperature by 3 K, during a period of 40 minutes.
- As the propeller rotates  $360^{\circ}$ , the weak background wind substantially impacts the air mixing processes downwind and upwind. When jets blow along with background wind, the warming plumes arrive earlier than the jet due to horizontal advection from earlier warmed sections. The warming plumes consequently accumulate downwind and penetrate deep into the canopy. In contrast, in upwind processes, wind drag resistance is felt and warming plumes arrive later than the jet. We speculate that these warming plumes are uplifted due to flow convergence and then recirculated by the ambient wind.
- Quadrant analysis reveals that flux transport during operation is dominated by sweeping and ejection motions. Intermittent downdrafts of warm air and updrafts of cool air result in efficient vertical heat exchange. This feature makes wind machines highly effective in increasing canopy airspace temperature to mitigate frost damage.

In this study, we only investigated the spatial-temporal variability of air warming under one machine type and one specific, given weather condition (possible thin-cloud condition). While the observed features like “inversion erosion” and “plume drifting” agree with the literature, we hope to provide more experimental evidence for various night conditions in future studies. In addition, more wind field measurements coupled with temperature data will help to understand the heat exchange between air and plant tissue (Boekee et al., 2023).

In a companion study, we simulate various potential operation scenarios (e.g., tilting angle, rotation period) numerically and assess the impact of local warming effects. Along with the present observational study, an enhanced physical understanding of the turbulent mixing processes in a complex environment may help to assess both the potential and the limitations of this emerging frost mitigation method.

## Intermezzo: Ventilation for Hot fruit?

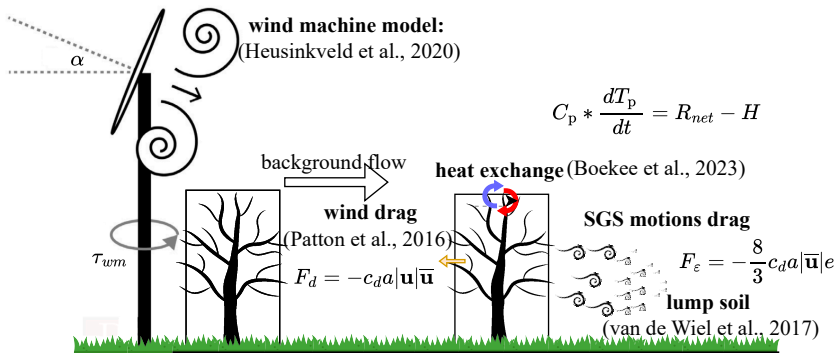
Air mixing is not only important for frost damage mitigation but also for climate control within greenhouses. In a close environment like a greenhouse, the temperature can become very high during summer days, and moisture can accumulate, potentially limiting plant evaporation and growth. In this Intermezzo, a collaborative study conducted at Delphy laboratories in Randwijk will be discussed. We investigated the air temperature distribution in a 150m<sup>2</sup> greenhouse using the Distributed Temperature Sensing (DTS) system (the method described in Section 2.2). Fiber optic cables were installed in the shape of two vertical “curtains” (shown in Fig. a and b), along with autonomous shielded temperature sensors (shown in Fig. b). The top of tomato canopy is approximately 2 m high.



The figure shows temperatures measured from one of the vertical curtains at 14:04 on 2022-08-25. A strong temperature inversion of about 5 degrees Celsius was observed within and above the canopy layer. This temperature inversion limits air mixing and moisture exchange between the canopy and the outside air, which further restricts plant evaporation and growth. One of the end goals of this project is to design an effective ventilation system to improve air mixing in the greenhouse. The DTS system will be helpful in monitoring the heat flow and air mixing processes in the greenhouse under different ventilation scenarios.

# 3

## AN INTEGRATED LARGE-EDDY SIMULATION FOR MODELING PLANT-TISSUE WARMING



“The integrated model is able to predict the plant-tissue temperature during wind machine operation in orchards”

Yi Dai

09–05–2023, EMS conference, Bratislava

### The third chapter is based on the articles:

Dai, Y., van Hooft, A., Patton, E. G., Boeke, J., van der Linden, S., ten Veldhuis, M.-C., & van de Wiel, B. J. (2024). Integrated large-eddy simulation for modeling plant-tissue warming induced by wind machines in an orchard canopy. *Agricultural and Forest Meteorology*, 356, 110175. <https://doi.org/10.1016/j.agrformet.2024.110175>

### 3.1. INTRODUCTION

Spring frost events can lead to significant economic losses in the agricultural sector (Lamichhane, 2021). To combat frost damage, wind machines (hereafter WMs) have become increasingly popular (Frith, 1951). During radiative frost nights, WMs generate strong jets and erode the near-surface thermal inversion through air mixing. This mixing process enhances both vertical air-to-air and local plant-air heat exchange, resulting in elevated plant-tissue temperatures. Understanding the dynamics of air mixing and their effects on plant-tissue temperatures is essential for optimizing WM operations.

Quantifying warming effects on plant tissues requires understanding the processes of vertical air-to-air mixing and local plant-air heat exchange. The air-to-air mixing effects highly depend on machine type (e.g., power, blades, hub height), operational settings (e.g., rotation period, tilting angle), and atmospheric conditions (e.g., inversion strength, wind speed) (Table 1 in Dai et al., 2023). Air-to-air mixing effects are spatially and temporally complex due to 360° rotation of the WM and interaction between the generated turbulent warming plumes and the non-uniform canopy structure. Locally, heat exchange processes depend on in-canopy air temperature, wind velocity and canopy characteristics. Furthermore, the distribution of mean wind and turbulence within the canopy airspace is also closely linked to the canopy structure. As a result, assessing the warming impact on plant tissues across the orchard is a challenging task.

Current physical understanding of the complex interactions of machine-induced warming of plant tissues remains limited. Experimental studies often face challenges with the coverage and resolution of measurements, which are typically insufficient to fully capture the temporal and spatial variability of machine-induced air mixing in orchards (e.g., Battany, 2012; Beyá-Marshall et al., 2019; Kimura et al., 2017; Ribeiro et al., 2006). Furthermore, there are only a few numerical studies available. Heusinkveld et al., 2020 simulated machine-induced air mixing using an actuator disk model and estimated air warming based on Gaussian curve fittings. Yet their study did not incorporate canopy effects, such as canopy drag and canopy-air heat exchange. The dynamic interplay between turbulent warming plumes and canopy structure, as well as the heterogeneous plant-air heat exchange in the orchard, has not been investigated numerically so far.

The field experiment conducted by our group (Dai et al., 2023) measured the air mixing effects of WM operation in a 6.75 ha orchard block. 2023 obtained quasi-3D air temperature responses with spatial-sampling and temporal resolution of 25 cm and 10 s, respectively, before and during WM operation. The current study is complementary to the field study: it aims to develop a numerical model for quantifying warming effects on plant tissues as well as resolving the dynamic interplay between turbulent rotating plumes and canopy structure. We implement an integrated model in a large-eddy simulation and validate the model against the field observations (2023). The integrated model incorporates a canopy model, an air-plant-tissue heat exchange model, and a wind machine model. The canopy model parameterizes the effect of orchard tree lanes on flow dynamics. We adapted the parameterization for horizontally-homogeneous canopies from E. G. Patton et al., 2016. We integrate a conceptual energy balance model to investigate the local air-plant-tissue heat exchange processes and to simulate plant-tissue temperature dynamics (Boekee et al., 2023). Additionally, the WM operation is parameterized using an actuator disk approach following Heusinkveld et al., 2020. A detailed

description of the LES and the integrated model is provided in Section 3.2. The simulation settings for reproducing the experimental conditions are explained in Section 3.3. We compare the simulated results with field data previously reported in Dai et al., 2023. Using a total of 9 km of fiber optic cable, their study measured quasi-3D temperature responses with a spatial sampling of 25 cm and a temporal resolution of 10 s over a 6.75 ha orchard. Specifically, we compare simulation results with measurements taken at a 9 m tower and a horizontal slice over a 6.75 ha orchard at 2 m height. The comparison between the measurements and simulation results is presented in Section 3.4. To further explore the air mixing effect across the orchard, simulated temperature and wind profiles are examined in Section 3.4. Section 3.4 explores the mixing dynamics up- and down-stream. The conclusion and recommendation for future work are given in Section 3.5.

## 3.2. THE INTEGRATED MODEL

### THE LARGE-EDDY SIMULATION

The large-eddy simulation is based on Basilisk, a partial-differential-equation solver, which solves the equations of atmospheric boundary layer under the Boussinesq approximation on adaptive Cartesian grids. The application of adaptive mesh refinement (AMR) for studying turbulent atmospheric flows is well-documented in the literature (Heusinkveld et al., 2020; van Hooft et al., 2019; Van Hooft et al., 2018). The AMR method dynamically refines and coarsens the grid size in space and time based on the characteristics of the local flow field. Specifically, the mesh adjusts its refinement levels by comparing the local discretized error to a prescribed refinement threshold. The AMR method in Basilisk used for current study is expected to resolve the presence of orchard tree lanes and the WM using minimum grid size, while coarsening the grid in the less turbulent areas. Thus, employing AMR is expected to enhance computational efficiency (Heusinkveld et al., 2020; Van Hooft et al., 2018). The grid setting near the canopy and WM is detailed in Fig. 3.2, Section 3.3. The LES filtered equations for momentum  $\mathbf{u} = (u_1, u_2, u_3)$  in  $(x, y, z)$  directions and buoyancy ( $b$ ) are solved numerically. Parameterization of canopy processes ( $F_d, S_b$ ) and the WM forcing ( $U_M$ ) are discussed in Sec 3.2 and 3.2, respectively.

$$\frac{\partial \tilde{u}_i}{\partial t} + \frac{\partial \tilde{u}_j \tilde{u}_i}{\partial x_j} = -\frac{\partial \pi}{\partial x_i} + \tilde{b} \delta_{i3} - \frac{\partial \tau_{ij}}{\partial x_i} - \frac{\partial p_{LS}}{\partial x_i} + F_d + U_M, \quad (3.1)$$

$$\frac{\partial \tilde{b}}{\partial t} + \frac{\partial \tilde{u}_j \tilde{b}}{\partial x_j} = -\frac{\partial B_j}{\partial x_j} + S_b, \quad (3.2)$$

where the tildes denote the spatial filtered variables.  $\pi$  represents the modified pressure and  $\delta_{i3}$  is the Kronecker delta. The large-scale forcing is imposed by the pressure ( $p_{LS}$ ) gradient term. The Coriolis force is not included. We adhere to the Basilisk convention for solving buoyancy terms ( $b$ ), which is the same as solving for potential temperatures  $\theta$  as they vary linearly,

$$b = \frac{g}{\theta_{\text{ref}}} (\theta - \theta_{\text{ref}}), \quad (3.3)$$

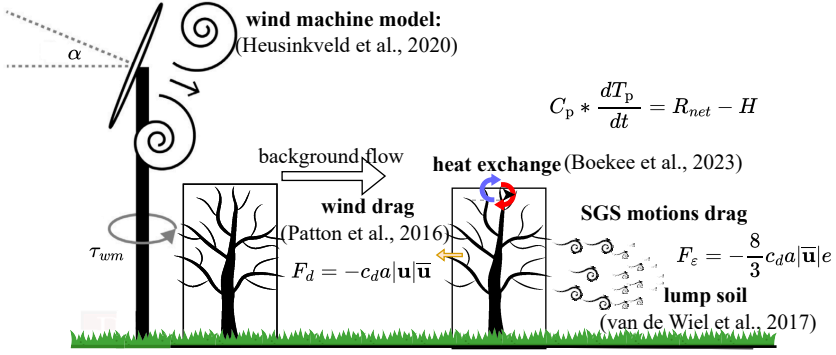


Figure 3.1: The map illustrates physic modules integrated in the LES: the canopy model, the air-plant-tissue heat exchange model, the wind machine model, and the lump soil model. The setting of the grid where these parameterizations are applied are detailed in Section 3.3.

where  $\theta_{\text{ref}}$  is a reference potential temperature and  $g$  is the constant gravitational acceleration. The subfilter-scale momentum  $\tau_{ij}$  and buoyancy flux  $B_j$  are parameterized using a subfilter-scale (SFS) turbulent kinetic energy (TKE) scheme (Deardorff, 1980). In Heus et al., 2010, the prognostic equation for SFS-TKE  $e$  with a canopy-drag force on SGS motions is ( $F_\epsilon$  as explained in Sec 3.2),

$$\begin{aligned} \frac{\partial e^{1/2}}{\partial t} + \tilde{u}_j \frac{\partial e^{1/2}}{\partial x_j} = \frac{1}{2e^{1/2}} \left[ K_m \left( \frac{\partial \tilde{u}_j}{\partial x_i} + \frac{\partial \tilde{u}_i}{\partial x_j} \right) \frac{\partial \tilde{u}_i}{\partial x_j} - K_h \frac{\partial \tilde{b}}{\partial z} \right] \\ + \frac{\partial}{\partial x_j} \left( 2K_m \frac{\partial e^{1/2}}{\partial x_j} \right) - \epsilon - F_\epsilon, \end{aligned} \quad (3.4)$$

The first right-hand-side term contains SFS shear production and the buoyancy term.  $K_m$  and  $K_h$  are the turbulent eddy viscosities/diffusivities that vary spatially as a function of the SFS-TKE  $e$  (Deardorff, 1980). The SFS diffusion is the second right-hand-side term. The dissipation  $\epsilon$  is parameterized in terms of  $e$  and a characteristic mixing length scale  $\lambda$ . Here we use a modified formulation of mixing length scale accounting for the near-surface effects (Dai et al., 2021).

### CANOPY PHYSICS

The sink and source terms induced by canopy elements arise as a result of the implicit filtering associated with discretizing the equations on a grid. In Eq. 3.1, 3.2, 3.4,  $F_d$ ,  $S_b$ , and  $F_\epsilon$  represent the forcing and source terms attributable to the presence of the canopy (See Fig. 3.1). On grids without a tree, these terms equal zero. Within the canopy, the flow feels canopy influences through a combination of pressure drag and viscous drag  $F_d$ , through enhanced dissipation  $F_\epsilon$  associated with the fine-scale boundary-layers forming on the individual canopy elements, and through buoyancy forces associated with leaf-air temperature differences  $S_b$ . Our study follows the parameterization of  $F_d$  and

$F_\epsilon$  in [E. G. Patton et al., 2016](#) (Fig. 3.1). The buoyancy force in the canopy model is incorporated with an air-plant-tissue heat exchange model, which was tested previously for this orchard ([Boekeke et al., 2023](#)). This model calculates the plant-tissue temperature  $T_p$ , which results from the net effect of radiative cooling  $R_{\text{net}}$  and turbulent warming  $H$  (forced convection/advection by the WM),

$$C_p \frac{dT_p}{dt} = R_{\text{net}} - H, \quad (3.5)$$

where  $C_p$  is the plant-tissue heat capacity.  $R_{\text{net}}$  is calculated based on the Stefan-Boltzmann law, taking into account the temperatures of the sky, ground surface, and plants. The turbulent heat flux  $H$  between the leaves and the air in contact with them equals to,

$$H = \frac{\rho c_p (T_p - T_a)}{r_b}, \quad (3.6)$$

where  $\rho$ ,  $c_p$ ,  $T_a$  are the air density, heat capacity and temperature, respectively.  $r_b$  is the tissue boundary layer resistance for heat, which depends on the local Nusselt number, via the so-called ‘air-refreshment velocity’ (See [2023](#)). This velocity scale combines the effects from both free and forced convection ([Schuepp, 1993](#)). Based on the energy conservation within one grid-cell, the sensible heat source terms of the plant tissues  $H$  ( $\text{W m}^{-2}$ ) and the air  $S_b$  ( $\text{m s}^{-3}$ ) are related following,

$$S_b = \frac{g}{\theta_{\text{ref}}} \frac{Ha}{\rho c_p} \quad (3.7)$$

where  $a$  ( $\text{m}^2 \text{m}^{-3}$ ) is the plant area density (PAD).

### WIND MACHINE PARAMETERIZATION

This section succinctly describes the wind machine parameterization [Heusinkveld et al., 2020](#). The WM is idealized as an actuator disk. At each numerical time-integration step, we assume uniform distribution of momentum injected by the rapidly rotating blades across the disk. In the context of this study, which focuses on quantifying warming effects on plant tissues, detailed modeling of blade rotation effects is overly complex and computationally expensive. For future studies, it might be worthwhile to explore the impact of the blade characteristics using an actuator line model, similar to those used in wind turbine studies (e.g., [Martinez et al., 2012](#); [Troldborg et al., 2007](#)). Additionally, the drag influence of the tower is considered to be negligible and is not included in the simulation.

The momentum forcing  $U_M$  injected at the exit of the numerical disk is calculated based on the work-energy principle: the power of the WM ( $P$ ) is used to increase the kinetic energy of the air, which leads to an increased ‘exit velocity’. From the appendix B1 of [Heusinkveld et al., 2020](#), assuming a zero entrance velocity, the momentum forcing  $U_M$  is approximated as,

$$U_M = \hat{n} \left( \frac{3Pl}{m} \right)^{1/3} \quad (3.8)$$

where  $\hat{n}$  is a unit vector normal to the numerical disk.  $m$  is the air mass and  $l$  is the disk thickness. Note that we do not explicitly model the thermodynamic effect of the engine heat that escapes due to motor inefficiency (2020). However, in reality, this factor is observed to influence the temperature field locally (see Fig. 3.6). We intend to include only the most prominent physical mechanisms to simulate air mixing effects of the WM and avoid confounding effects. The height of the numerical disk is  $h_{wm}$ . The disk rotates with a prescribed rotation period per cycle ( $\tau_{wm}$ ) and it tilts slightly downward at an angle ( $\alpha$ ) of 8 degrees. The drag effect of the tower is ignored in the simulation.

### THE LAND-SURFACE MODEL

The coupling between the atmosphere and land surface is realized using a simplified surface-energy balance (van Hooft et al., 2019). This model calculates the sensible heat flux at the ground surface through the balance with net radiation and ground heat flux. The net radiation  $Q_s$  can be prescribed with a function during the course of simulations (e.g., a characteristic diurnal pattern as in 2019). During our short simulation period, we prescribe  $Q_s$  as a constant. The ground buoyancy flux  $G$  is parameterized using a lumped parameter model (B. J. Van de Wiel et al., 2017),

$$G = \Lambda(b_{\text{surf}} - b_{\text{soil}}), \quad (3.9)$$

where  $\Lambda$  denotes the lumped parameter, representing the feedback between the characteristic soil temperature  $b_{\text{soil}}$  and ground-surface temperature  $b_{\text{surf}}$ , expressed using their buoyancy equivalents (Eq. 3.3). The soil is simplified as a homogeneous layer with a constant temperature. The interaction between the land surface and machine-induced air mixing plays a crucial role. Before the WM operation,  $b_{\text{surf}}$  is lower than  $b_{\text{soil}}$ , resulting in a positive ground heat flux for the surface layer. During the WM operation, the ground heat flux is reversed as the surface layer is warmed by the WM mixing effects. Normally,  $b_{\text{surf}}$  is determined using a Monin–Obukhov boundary condition. However, this approach results in extremely low values of  $b_{\text{surf}}$  in the presence of strong surface temperature gradients that occur during the WM operation. Moreover, Monin–Obukhov boundary conditions are often not well-defined within the canopy layer. Therefore, a simplified approach is employed: when the jet passes over the surface (indicated by a surface friction velocity exceeding 0.01 m/s), the boundary condition is set to the temperature at the first grid level. If not, the boundary condition is adjusted to 90% of the temperature at the first grid level. Note that this land surface model is a simplification of the more complex reality. Such a simplification is chosen to balance the model complexity and physical realism. While this simplified approach captures essential dynamics (see Section 3.4), it is possible to incorporate more detailed models, such as a multi-layer soil scheme and/or a grass heat transfer model (van der Linden et al., 2022).

### 3.3. SIMULATION SETTINGS

The integrated model simulates the scenario from May 7, 2021 (Dai et al., 2023), where quasi-3D temperature responses to WM operation were measured in a pear orchard (Fig. 3.2c). The simulation includes a neutral spin-up period (200 mins) followed by a period of surface cooling (50 mins). The relatively long spin-up period is necessary to

ensure the model reaches observed initial condition and the turbulence development under a very stable condition. The cooling phase begins with a 10-minute window without WM operation, followed by a 40-minute window with WM operation, featuring 8 rotation cycles, each lasting around 5 minutes. The computational domain spans (2048, 2048, 2048)-m in  $(x, y, z)$  directions.  $x$  and  $y$  are horizontal streamwise and cross-stream directions, respectively.  $z$  represents the height from the surface (vertical axis).

Using the AMR method, the refinement levels vary from 5 to 11, corresponding to grid-element sizes of 64 m and 1 m, respectively. Cartesian grids dynamically refine or coarsen between these numbers of levels based on a specified refinement criterion. Error thresholds for wind velocities and buoyancy (in temperature value) are set at 0.3 m/s and 0.35 K, respectively. A minimum grid size of 1 m is set near the canopy and disk to ensure fully resolved features. Fig. 3.2a illustrates the grid structure on an  $x$ - $z$  slice at  $y = 1024$  m, mirroring the layout of the experimental pear orchard (See Fig. 3.2c) described in 2023. In this orchard, the height of trees  $h$  and spacing of tree rows  $r_{tr}$  are 3 m. The orientation of tree lanes to the background wind during the experiment is roughly  $45^\circ$  to the east. To configure such a layout in the simulation, the numerical tree lanes are implemented with a conditional function  $TL(x, y, z)$ ,

$$TL(x, y, z) = \begin{cases} 1, & \text{mod}(|x - y|, 4) = 0 \text{ and } z \leq h \\ 0, & \text{otherwise} \end{cases} \quad (3.10)$$

where  $\text{mod}$  is a modulus operator. Canopy effects are applied to the *tree-grids* where  $TL > 0$ . With 1 m grid size near the canopy,  $r_{tr}$  equals 2.82 m (Fig. 3.2b). The canopy is vertically resolved by 3 grid points with a constant PAD profile  $a$  ( $\text{m}^{-2} \text{m}^{-3}$ ) of 1.20 over height. This constant PAD over height is an empirical setting based on trial and error by checking if the spin-up temperature profiles reach a quasi-steady state and align with observations (results not shown). The drag coefficient  $c_d$  quantifies the efficiency of momentum absorption by canopy elements whose varies slightly with wind speed (E. Patton & Finnigan, 2013). Brunet et al., 1994 address the height-dependency of  $c_d$  for a wheat-model in a wind tunnel. Furthermore, even assuming  $c_d$  is constant, its value is reported to vary across different settings and applications (see Table. 3.1). For simplicity,  $c_d$  is set as a constant of 0.20 in this study. The appropriate parameterization of  $c_d$  for the current application requires thorough experimental design and numerical investigation, which is beyond the scope of this study.

Leaf temperatures are modeled at the *tree-grids* by solving Eq. 3.5. The simulated leaf temperatures will be compared with measurements from Boekee et al., 2023. The air-plant-tissue heat exchange model allows for other tissue types by modifying the characteristics of the plant tissue. The parameters for three tissue types including the leaf can be found in 2023. The leaf temperature profile is initialized as a constant temperature of  $T_p = 6^\circ \text{C}$  within the canopy.

The numerical disk description mimics the real outdoor WM Dai et al., 2023 and has the dimensions of a 6 m diameter located at 10.5 m (hub) height. The disk is placed at location of (500, 1024, 10.5)-m in the  $(x, y, z)$  directions (Fig. 3.2a). The tilting angle  $\alpha$  is  $8^\circ$ . The rotational period  $\tau_{wm}$  is found to be 288 s based on numerical testing, which is slightly shorter than the user-specified setting (300 s). The WM-power to the air mass ratio  $P/m$  is set as  $3000 \text{ m}^2 \text{ s}^{-3}$  based on a technical report from the manufacturer.

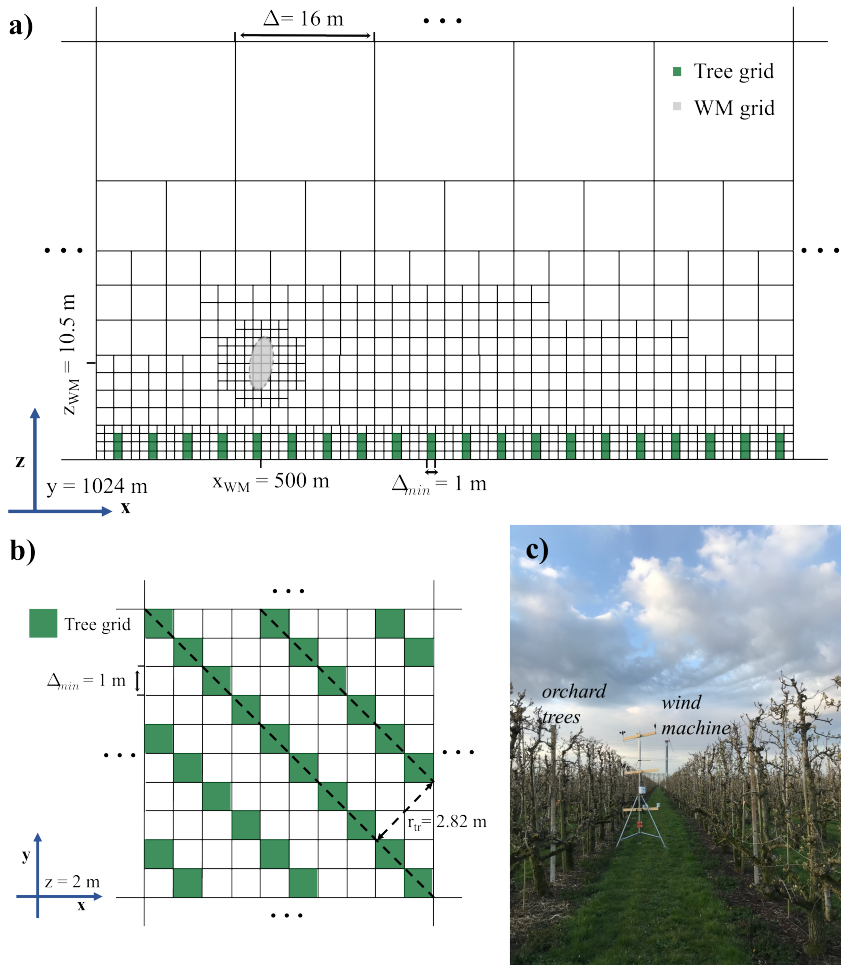


Figure 3.2: The illustration shows a sample grid structure on two planes: the x-z plane at  $y = 1024$  m (panel a) and the x-y plane at  $z = 2$  m (panel b). The grid structures in panels a and b are from specific sections, visualized at different scales for clarity. In panel a, the WM-grids are shown when the numerical disk aligns with the x direction. The resolved WM-grids adapt with the WM's rotation. Additionally, panel c shows the experimental site, including the wind machine, tree lanes and weather station.

Table 3.1: This table aims to show a range of drag coefficient  $c_d$  values from some applications, rather than to explain the reasons for these specific values.

Studies	application	drag coefficients
Raupach et al., 1986	vertical aluminium strips in a wind tunnel	1.6
Dwyer et al., 1997	following Shaw et al., 1988	0.15
Katul et al., 2004	eight terrestrial plant types	0.10 - 0.30
Finnigan et al., 2009	following Brunet et al., 1994	0.47
Chahine et al., 2014	a vineyard	0.20
Torkelson et al., 2022	a model of the vineyard canopy in a wind-tunnel	0.50
The present study	a pear orchard	0.20

Winds were very light during the experiment. The pressure gradient force in the direction of the mean wind is estimated based on the surface friction (Eq. 2 from B. Van de Wiel et al., 2003). The measured friction velocity at the canopy top is  $0.0335 \text{ m s}^{-1}$ . The calculated pressure gradient force is in the order of  $\mathcal{O}(-7)$  to  $\mathcal{O}(-6) \text{ m s}^{-2}$ . This value is extremely small and results are not sensitive to this value based on numerical testing. The bulk Richardson number is around 3, which suggests a very stable condition. The initial conditions of wind and air temperature are based on the fifth generation of global climate reanalysis data, ERA5 (Hersbach et al., 2023). A constant air temperature of  $9.5 \text{ }^\circ\text{C}$  is initially set from the surface up to 100 m height and then linearly increasing with a constant rate of  $3 \text{ }^\circ\text{C km}^{-1}$ . The initial wind profile  $u$  is a function of the height  $z$ ,

$$u = \begin{cases} 0.25 \ln(z/z_{0m}) \text{ m s}^{-1}, & z < 300 \text{ m} \\ (1.6 + 0.01(z - 300)) \text{ m s}^{-1}, & 300 \text{ m} \leq z < 1024 \text{ m} \\ 9 \text{ m s}^{-1}, & 1024 \text{ m} \leq z < 2024 \text{ m} \end{cases} \quad (3.11)$$

where the aerodynamic roughness length  $z_{0m}$  equals 0.1 m. The initial profile of SGS-TKE ( $e$ ) is set as constant  $5 \times 10^{-5} \text{ m}^2 \text{ s}^{-2}$ . In the surface layer, the characteristic lumped parameter  $\Lambda$  is set as  $0.0035 \text{ m s}^{-1}$ , in equivalent to  $4.6 \text{ W m}^{-2} \text{ K}^{-1}$ , which is an average value during the night time condition based on data obtained at Cabauw (van Hooft et al., 2019). A summary of the parameters used in this study is presented in Table 3.2.

To prevent the formation of gravity waves at the top boundary, a sponge layer is applied in the upper half of the domain (Klemp & Lilly, 1978). In our simulation, dealing with the complex effects of tree lanes and the WM requires careful consideration of lateral boundary conditions. To dampen wave effects by the WM, a buffer/absorbing layer is applied near lateral boundaries. In this layer, the standard practice is to nudge the flow fields towards a predefined solution. However, such fixed and homogeneous solution conflicts with the heterogeneous cooling effects from tree lanes and the surface. Another alternative is radiation boundary conditions, which allows wave movement out of the simulation domain. In our implementation, this also proved challenging because the vertical velocity is quite sensitive to the presence of irregular tree lanes. To overcome this issue, we set periodic lateral boundary conditions in a large-size domain. This set-

Table 3.2: A summary of the parameters used in this study. The values inside of brackets are their buoyancy equivalents.

Symbols	variables	values
$C_p$	leaf heat capacity	$2E6 \text{ J m}^{-3} \text{ K}^{-1}$
$c_d$	drag coefficient	0.20
$a$	plant area index	$1.2 \text{ m}^{-2} \text{ m}^{-3}$
$c_p$	air heat capacity	$1005 \text{ J kg}^{-1} \text{ K}^{-1}$
$P/m$	the power of the WM per air mass	$3000 \text{ m}^2 \text{ s}^{-3}$
$l$	the thickness of WM disk	0.3 m
$h_{wm}$	height of the WM	10.5 m
$U_M$	WM momentum forcing	$13.92 \text{ m s}^{-1}$
$\alpha$	tilting angle of the WM	$8^\circ$
$Q_s$	net radiation at the ground surface	$-7.2 \text{ W m}^{-2}$ $(-0.00024 \text{ m}^2 \text{ s}^{-3})$
$\Lambda$	the characteristic lumped parameter	$4.0 \text{ W m}^{-2} \text{ K}^{-1}$ $(0.0035 \text{ m s}^{-1})$
$b_{soil}$	the lump soil temperature	$2.7 \text{ }^\circ\text{C}$ $(0.1 \text{ m s}^{-2})$

ting means that even though the focus of this work is on a single orchard, the simulation actually reflects flow over an infinitely repeating set of orchards. We show in A.3 that the wave effect has diminished below our specified refinement criterion before exiting the downwind domain boundary and re-entering the upwind boundary. For future studies, more dynamic and flexible technique of lateral boundary conditions by Araya et al., 2011; Munters et al., 2016 can be employed for the application of multiple-WMs.

The simulation required 75.5 wall-clock hours utilizing 1024 computer cores. The number of numerical grid cells is around  $4.4E7$ , which is around 0.5 % of the total  $2048^3$  grid points that would have been used with uniform Cartesian grids. After the spin-up period, 3D snapshots of wind velocities ( $u_1, u_2, u_3$ ), buoyancy term ( $b$ ), and leaf temperatures ( $T_p$ ) on adaptive grids are dumped at a logging interval of 4 s (Fig. 3.2ab). The average size of each snapshot is approximately 2.6 GB, totalling 1.95 TB of output data. For ease of comparison with field observations, output fields from grid cells larger than the minimum grid size of 1 m are interpolated onto regular Cartesian grids with a uniform grid size of 1 m. The simulation data, near a 9 m tower located 30 m downstream, are logged at a frequency of 1 s.

### 3.4. RESULTS AND DISCUSSION

Here, we focus on the comparison between the simulation and measurements, and the physical interpretations of the measurements are detailed in Dai et al., 2023.

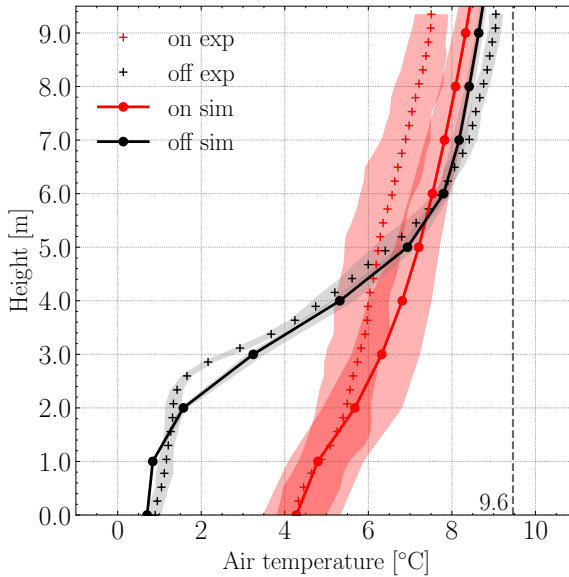


Figure 3.3: Comparison of measured (plus markers) and modeled (solid lines with circle markers) time-averaged vertical temperature profiles during the on (red) and off (black) mode at tower W1. The standard deviation of the air temperatures is included with shaded contours.

### COMPARISON WITH EXPERIMENTAL DATA

Time-averaged vertical temperature profiles before and during the operation period along tower W1 are presented in Fig. 3.3. Before the WM operation, a strong temperature inversion forms just above the canopy as a result of the longwave radiative cooling. Within the canopy, the temperature profile is nearly neutral. The canopy model simulates the temperature profile before WM operation well. During WM operation, air mixing caused by the WM erodes the temperature inversion. The model is capable of simulating the warming within the canopy, whereas temperatures above the canopy are slightly overestimated compared to observations. The discrepancy can be explained by the fact that in reality the WM had a start-up period of about 45 minutes, where it had two ‘intermittent/irregular’ cycles. During this period the system already cooled. However, the simulation excluded this non-stationary period (only regular cycles were considered), and therefore the additional cooling was not accounted for (Fig 6 of 2023).

Fig. 3.4 compares the measured (a) and modeled (b) time height plot of air temperatures at tower W1. Panel c shows observed and modeled temperature time series at heights of 1 m and 9 m. During WM operation, the warm plumes periodically penetrate from the top into the canopy. As a result, the canopy airspace temperatures briefly rise and the temperatures start to drop after warm plumes pass by. Simulation results capture the periodic warming-cooling pattern and magnitude well. The model slightly overestimates air temperatures at 9 m height. Similar to Fig. 3.3, this is likely due to the exclusion of the start-up period from the simulation. Before WM operation, tempera-

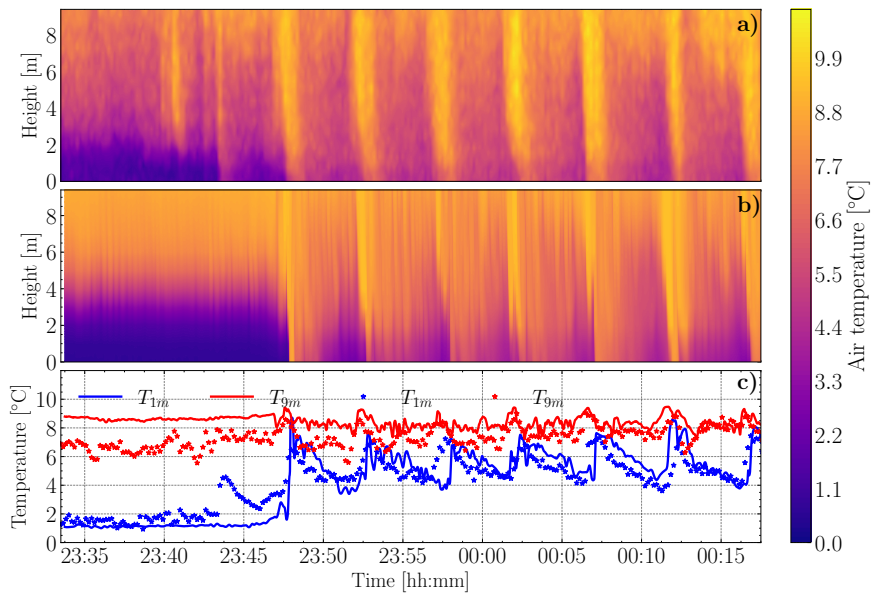


Figure 3.4: Observed (a) and modeled (b) time height plot of air temperatures at tower W1. Panel c shows time series of 1 m (blue) and 9 m (red) air temperatures from the simulation (solid lines) and measurements (star markers).

ture signals show canopy-induced wave-like fluctuations near the canopy top, similar to the observations in a forest canopy (Lee & Barr, 1998). These fluctuations are less pronounced in the measurements, possibly due to the higher logging frequency in simulations (1 s) compared to the measurements (10 s).

Fig. 3.5 displays measured (a) and simulated (b) time series of air and leaf temperatures over 8 rotation cycles. The model captures the dynamics of air and leaf temperatures well, specifically the periodic warming-cooling pattern and air-leaf temperature magnitude. Prior to operation, simulated leaf-air temperature differences are around  $0.5\text{ }^{\circ}\text{C}$  larger than measured differences (around  $1\text{ }^{\circ}\text{C}$ ). This could be attributed to the leaf energy budget representation (e.g., net radiation), which is highly simplified. Similar overestimation of leaf-air temperature differences was observed after the warming plumes pass by. During the rotation cycle, as the jets pass by, leaf temperatures closely follow the air temperatures, indicating a strong coupling due to effective heat exchange, which was also reported in the observational study of Boeke et al., 2023. Just before the arrival of the jet, a relatively larger difference between air and leaf temperatures is observed in both the simulation and measurement. This is due to radiative cooling by the leaf.

Time-averaged air temperature changes before and during operation over a horizontal plane at 2 m height from measurements (a) and simulation (b) are shown in Fig. 3.6. Overall, the simulated temperature change agrees remarkably with measurements in terms of the magnitude, coverage and shape. In the area of warming larger than  $4\text{ }^{\circ}\text{C}$ ,

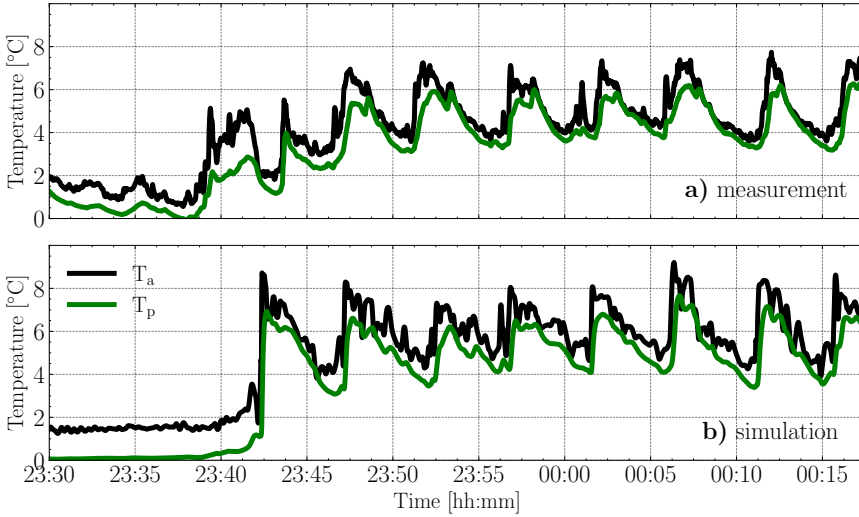


Figure 3.5: Observed (a) and modeled (b) time series of air ( $T_a$  in black) and leaf ( $T_p$  in green) temperatures over 8 rotation cycles.

the warming shape is slightly different from the measurements and the magnitude of simulated warming is larger than measured warming. Additionally, both simulated and observed warming plumes are observed to drift downstream relative to the WM (see instantaneous movies of the warming plumes in supplementary material). This results from the advection of the plumes by the wind similar to drifts reported in other studies (e.g., [Beyá-Marshall et al., 2019](#); [Dai et al., 2023](#); [Heusinkveld et al., 2020](#)). In measurements (panel a), the white spot near the WM indicates the heat emission by the engine. This aspect is not included in our simulation for simplicity and to prevent overlapping of physical effects.

Table 3.3 summarizes the statistics of the total wind speed  $M$  at tower W1 during on and off modes. Overall, there is a good agreement between the measurements and simulation, except for the underestimated minimum wind speed during operation. Fig. 3.7 compares phase-averaged wind velocities over 8 rotation cycles between the simulation and measurements. A similar underestimation of minimum wind speed just before operation is observed, likely due to the more idealized nature of the simulation compared to physical reality. When the jet passes by, and after it has passed the tower, the simulated wind speed aligns closely with the measurements.

### SIMULATED VERTICAL, STREAMWISE AND CROSS-STREAM PROFILES

Figure 3.3 shows that simulated temperature profiles agree with measurements at tower W1. To understand the WM influence across the field, wind and temperature profiles are binned by their radial distance from the WM and profiles within each bin are averaged. In Fig. 3.8, radially averaged wind (a) and air temperature (b) vertical profiles reveal two distinct mixing zones influenced by the WM's operation: the near-jet and far-

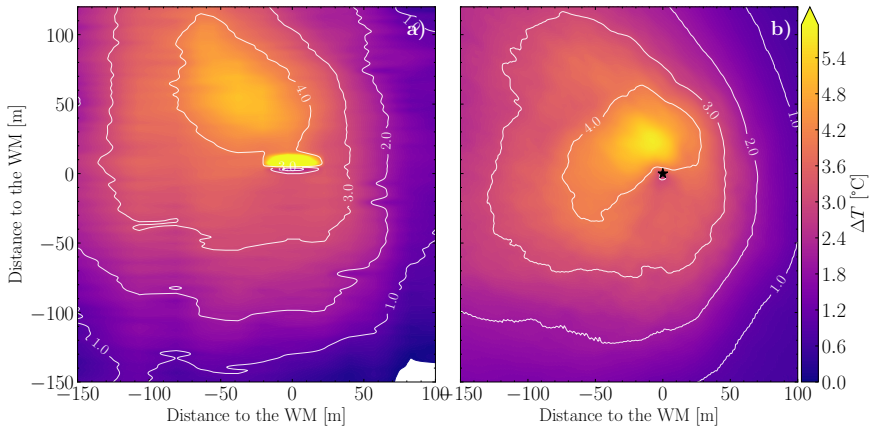


Figure 3.6: Comparison of measured (a) and modeled (b) time-averaged air temperature changes over a horizontal plane at 2 m height. The slice from simulation is rotated  $45^\circ$  to align with the measurements. The WM is located at (0, 0). The heat plume emitted by the engine is only visible in the measurements.

Table 3.3: Descriptive statistics of observed and simulated wind speed  $M$  ( $\text{m s}^{-1}$ ) during on and off modes at tower W1. The frequency of the measured wind speed is 10 hz and it is sampled in the same frequency as the simulation output 1 s.

	Measurement ( $\text{m s}^{-1}$ )	Simulation ( $\text{m s}^{-1}$ )
$\overline{M_{off}}$	0.44	0.47
$\sigma_{M_{off}}$	0.06	0.04
$\max(M_{off})$	0.60	0.58
$\min(M_{off})$	0.30	0.38
$\overline{M_{on}}$	1.08	0.88
$\sigma_{M_{on}}$	1.01	0.81
$\max(M_{on})$	7.76	7.99
$\min(M_{on})$	0.54	0.11

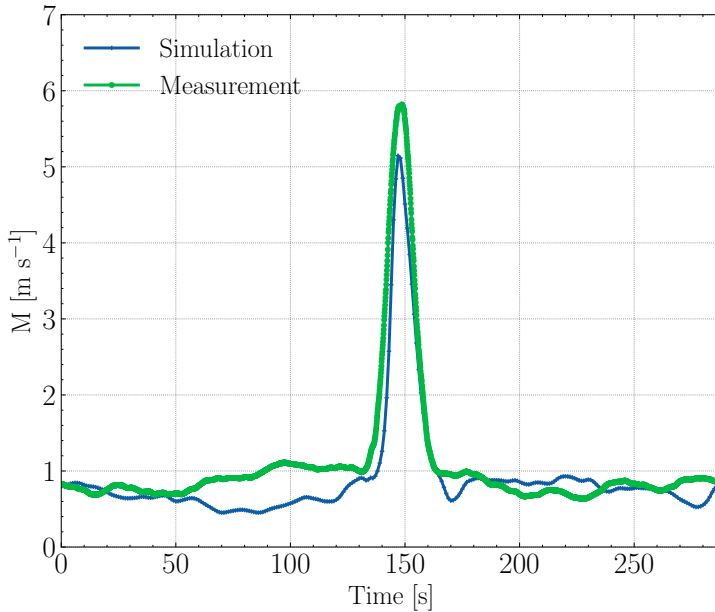


Figure 3.7: Comparison of measured and modeled phase-averaged wind velocities over 8 rotation cycles.

jet mixing zones. The near-jet mixing zone, characterized by high wind velocities up to  $9 \text{ m s}^{-1}$  at 1 m from the WM at hub height, extends up to about 20 m from the WM location, which is a length of 3 – 4 rotor diameters. The range of the near-jet mixing zone is defined by regions where the wind profile exhibits a clear jet-like shape. Wind velocities decrease rapidly with increasing radial distance from the WM. Similarly, air temperatures adjacent to the WM at lower heights exhibit increased warming because of the direct jet-mixing effects. This effect is most pronounced around 20 meters from the machine (the black dashed profile). Interestingly, the temperature profile near the WM (red dashed line) shows a decrease at hub height relative to areas farther from the WM. This suggests that maximum warming near the surface at around 20 m from the WM is caused by downward mixing of warmer above-canopy air at the hub height of the WM.

The air mixing zone beyond 20 m away from the WM is labeled as the far-jet mixing zone, featuring contrasting changes in wind and temperature profiles. This sharp transition of wind profiles beyond the near-jet mixing zone shows the strongly reduced influence of mechanical propeller rotation. This is not only the result of canopy drag, but also of momentum conservation, as with increasing radius more air is entrained into the jets. Notably, in the absence of direct jet mixing and with a mean wind velocity of  $0.2 \text{ m s}^{-1}$  within the canopy, the air temperature warming remains and decreases gradually with increasing distance from the WM. This sustained warming is likely due to the advected warming air induced by the jets, which is demonstrated in the supplementary material. The upper bounds of the far-jet mixing zone are 150 m upstream and 550 m downstream, respectively (discussed in Fig. 3.9). For better interpretations and under-

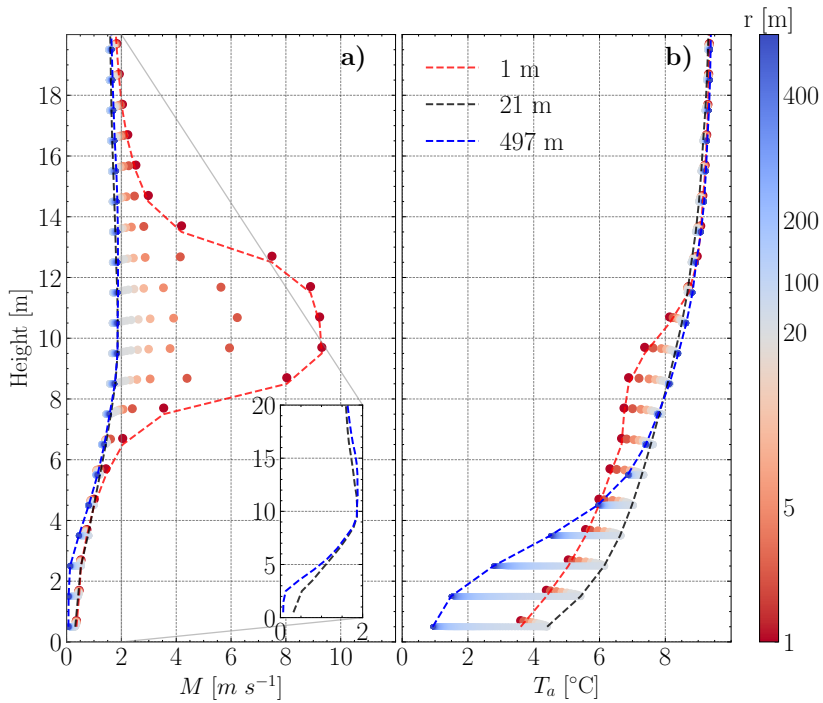


Figure 3.8: Distribution of vertical profiles of wind velocity  $M$  (a) and air temperature  $T_a$  (b) with increasing distance  $r$  [m] from the wind machine. The distance is marked by the color bar. Three profiles at 1, 21 and 499 m away from wind machine are lined. The dots of profile from 1 to 21 m are artificially elevated by 1 cm to avoid overlapping. A zoom-in window in panel a illustrates the canopy-influenced wind profile (blue dashed line) at further distance and the differences to the profile at 21 m (black dashed line).

standing, the mixing zones are labeled as direct-jet and far-jet mixing. In future studies, it is recommended to explore the quantitative definition of mixing zones and the relationship to the WM thrust, the atmospheric stability and canopy characteristics.

To further investigate the range of warming in horizontal directions, we space-time-average air and leaf temperature profiles along *streamwise* ( $x$ ) and *cross-stream* ( $y$ ) directions. In Fig. 3.9a, in the *streamwise* direction, the temperatures within the canopy ( $z \leq 3$  m) are first averaged over  $y$ - $z$  slices and then averaged for both off and on periods. During the operation, enhanced warming of the air and leaves is observed to extend further downstream than upstream, with the maximum warming occurring at around 20 meters downwind. Considering the error threshold for the air temperature being 0.35 K, we estimate the warming ranges between roughly 150 meters upstream and 550 meters downstream. This asymmetry in warming is caused by the weak background wind ( $0.2 \text{ m s}^{-1}$  within the canopy), which hinders or helps the development of the warming plume upstream or downstream, respectively. The same phenomenon is reported in Dai et al., 2023; Heusinkveld et al., 2020. It is noteworthy that the simulated warming range 550 m downstream is larger than the limited measurement range of 130 m in Dai et al., 2023. In the *cross-stream* direction (Fig. 3.9b),  $x$ - $y$  slices are averaged. The cross-stream picture is much more symmetrical, because the direct influence of the background wind is limited. Warming ranges for both air and leaves extend to approximately 250 meters on each side.

Near the WM, leaf temperatures closely follow air temperatures in both *streamwise* and *cross-stream* directions. In contrast, at greater distances from the WM, the difference between leaf and air temperature is about 1 degree. This variation in distances is linked to the WM-induced air warming and air-leaf heat exchange dynamics (Fig. 3.9bd). Near the WM, the turbulent heat flux  $H$  increases (negatively) due to elevated air temperature and wind speed, thus raising the leaf temperature. Even though radiative cooling intensifies with leaf warming, turbulent warming is predominant except where leaf and air temperatures are nearly equal. This is because  $H$  linearly relates to the temperature difference between the leaf and air. At a further distance from the WM, both air and leaf temperatures are approximately  $0.35 \text{ }^\circ\text{C}$  higher during operation than in the off period, which seems inconsistent with the negative leaf energy budget. The overestimated warming is likely due to the machine-induced warming circulated within the periodic domain, but its magnitude is relatively minor compared to the error threshold of  $0.35 \text{ }^\circ\text{C}$ .

### SIMULATED PHASE-AVERAGED STREAMWISE SECTIONS

Two instances of phase-averaged air temperature (in contours) and wind (in arrows) sections are shown in Fig. 3.10 to illustrate the mixing dynamics between warm plumes and ambient wind. The interactions are shown in opposing (a) and aligning (b) directions. These sections are taken from the midpoint of the *cross-stream* direction. In panel a, where the jet flows against the background wind, wind arrows depict a convergence pattern upwind of the WM. This is due to the collision between the decelerating jet and the background airflow. This agrees with the second warming plume measured in 2023. When the jet flows with the background wind (panel b), warming plumes travel further, creating wave-like patterns downstream. As a result of the background wind advection,

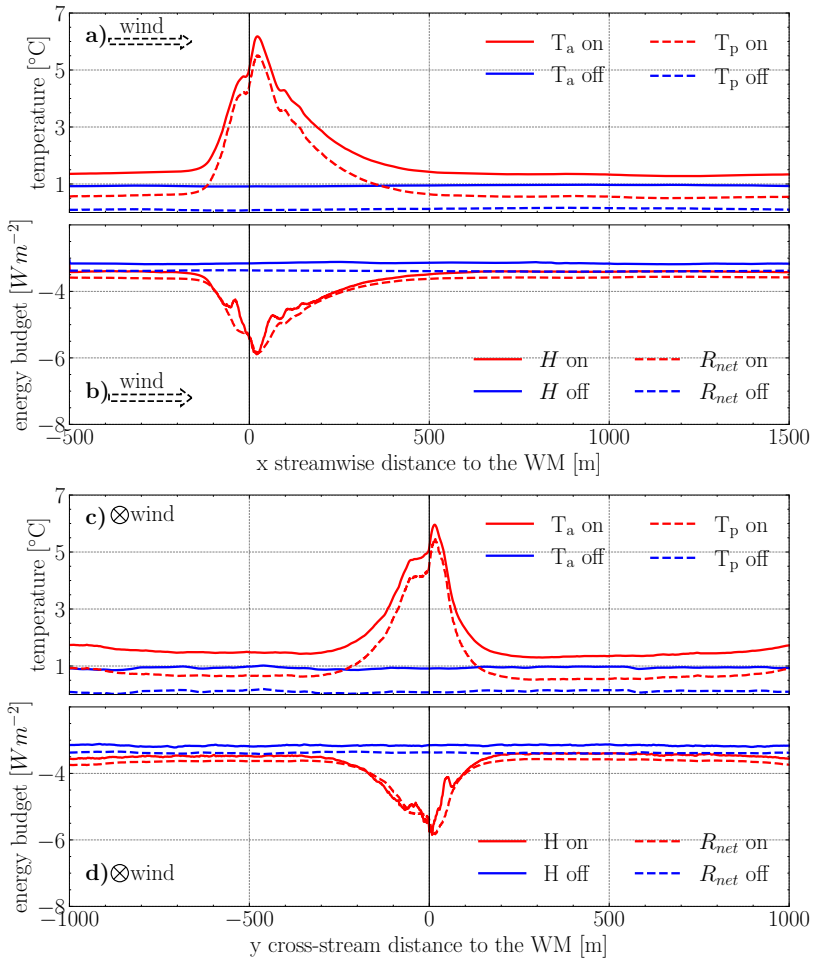


Figure 3.9: The spatial-time-averaged air ( $T_a$  in solid lines) and leaf ( $T_p$  in dashed lines) temperature profiles along *streamwise* (a panel,  $z = 1024$ ) and *cross-stream* (c panel,  $x = 500$ ) directions. Averaged periods of on and off modes are represented by red and blue lines. The corresponding leaf energy budgets of the turbulent heat flux  $H$  and net radiative cooling  $R_{net}$  are shown in other two panels. The wind machine location  $(0, 0)$  in  $(x, y)$  direction is indicated with black solid lines.

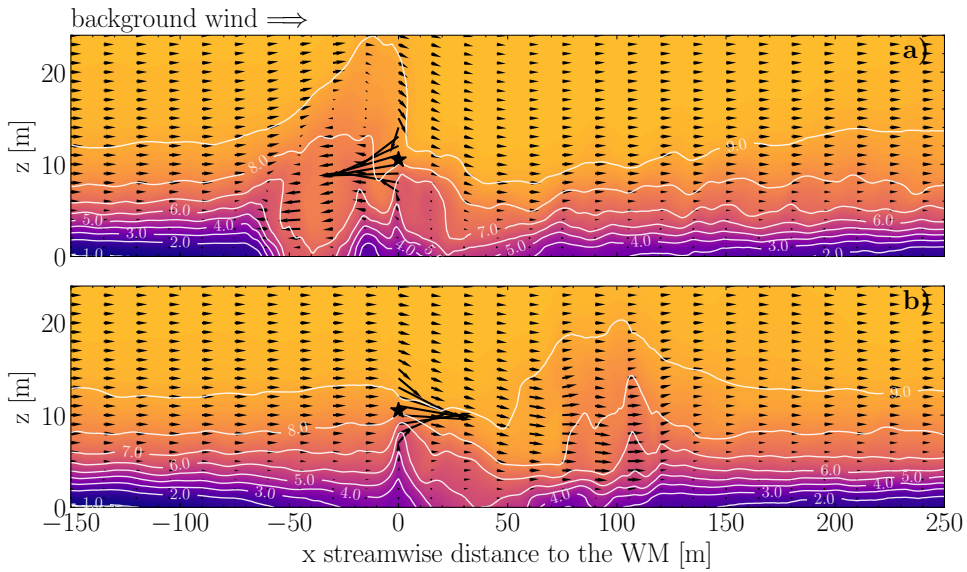


Figure 3.10: Phase-averaged air temperatures (in contours) and wind (in arrows) along the *streamwise* section. The section is taken from the center of the *cross-stream* direction. Two instances are presented when the jet flows against (a) and aligned with (b) the background wind. In panel a, a convergence vortex structure develops upwind of the WM. The center location of the wind machine hub is marked with a black star.

downstream warming extends to a greater distance than the warming upstream (Fig. 3.6 and 3.9). Instantaneous movies of the warming plumes in supplementary material show the dynamic interactions between the jet and the background wind.

### 3.5. CONCLUSION

The present study implements an integrated model in LES to quantify the warming effects of WM operation on plant tissues. For the first time, this model integrated in LES incorporates an air-vegetation energy exchange model and a highly dynamic driver of atmospheric disturbance (the wind machine). We compare simulation results with quasi-3D temperature measurements based on 9 km of fiber optic cables over a 6.75 ha orchard 2023. Our integrated model can reproduce the complex mixing and warming effects of the WM operation observed in the field.

Based on the numerical simulation,

- during WM operation, two distinct mixing zones are present: near-jet and far-jet mixing zones. The near-jet mixing zone extends up to about 20 m from the WM location, a length of 3–4 rotor diameters. This zone is predominantly influenced by direct mixing of the jet. We found that the maximum warming near the surface at around 20 m from the WM is caused by downward mechanical mixing of warmer above-canopy air at the hub height of the WM. In the absence of direct jet mixing, the air warming decreases gradually with distance from the WM in the

far-jet mixing zone. This sustained warming is likely due to the advected warming air induced by the jets.

- The background wind despite being light ( $0.2 \text{ m s}^{-1}$ ) causes a strong difference in the warming of air and leaves upstream and downstream of the WM. When jets flow against the background wind, the wind depicts a convergence pattern. When jets flow along the background wind, warming plumes travel further, creating wave-like patterns downstream. As a result, the downstream warming range extends much further than the upstream range (550 m compared to 150 m). In cross-stream direction, both warming ranges for air and leaves extend to approximately 250 meters on each side.
- Within these warming ranges, leaf temperatures closely follow air temperatures due to strong turbulent heat exchanges. Outside the warming zone, radiative cooling prevails, returning the leaf-air temperature difference to approximately 1 degree.

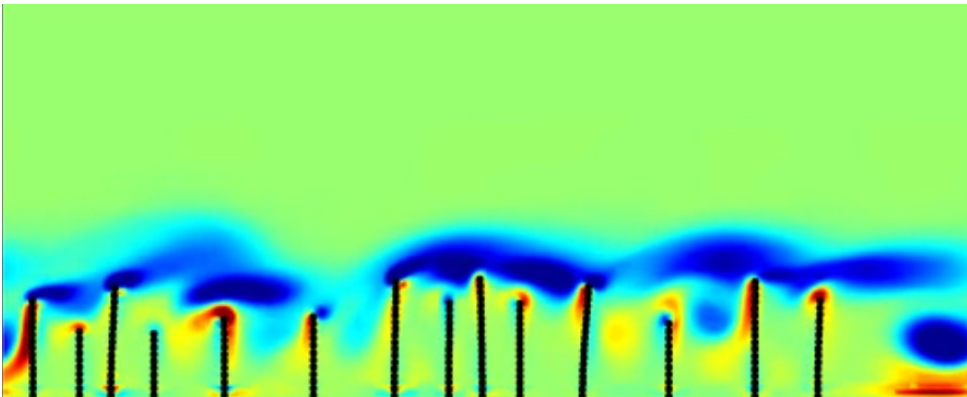
While our integrated model is able to reproduce air mixing effects observed in an experiment (2023), there is potential for further improvement of the model. Before the WM operation, simulated leaf-air temperature differences are around  $0.5 \text{ }^\circ\text{C}$  larger than measured differences (around  $1 \text{ }^\circ\text{C}$ ). We attribute this to the leaf energy budget representation, which is highly simplified. Currently, the leaf energy balance model calculates the radiation budget within canopy based on a Stefan–Boltzmann law. For future studies, it is recommended to incorporate the scattering and reflection of radiation using a canopy radiation model (Guenther et al., 2006; E. G. Patton et al., 2016).

Furthermore, it is realized that our model is only compared to a single observational case, which may limit the generality of the outcome. In future studies, we aim to conduct more field experiments for model development. The development of the fiber-optic sensing technique (Freundorfer et al., 2021; van Ramshorst et al., 2020) enables obtaining temperature and wind speed measurements at high resolutions and over large spatial areas. Additionally, various types and operations of wind machines should be investigated. Our study finds that the warming plumes travel further with the help of the background wind. This may suggest that other WM operational modes (e.g., sweeping half circles along the wind) may perhaps be equally or more efficient. This needs to be investigated.

Overall we conclude that the model provides a useful surrogate of outdoor reality with respect to wind machine operation in orchards. As such, it can be used to explore various scenarios to further optimize the efficiency of WM operation under various conditions. For instance, apart from testing the  $180^\circ$  rotation of WMs, the combined warming effects of WMs and heaters can be numerically investigated. It enables possibilities for the development of anti-frost wind machines and new frost mitigation methods. Overall, this numerical study confirms that the WMs are able to significantly change the local climate in orchards as to mitigate frost damage over several hectares. As such, numerical models such as presented here may help to improve understanding of machined-induced plant warming systems.

# 4

## FROM SMOOTH WALL FLOW TO GRASS-CANOPY FLOWS



“understanding the processes controlling vegetation–atmosphere exchange is of critical importance for weather, climate, and environmental forecasting as well as for agricultural and natural resource management. ”<sup>1</sup>

---

<sup>1</sup> Patton, E., & Finnigan, J. (2013). Canopy turbulence, chap. 24. In *Handbook of environmental fluid dynamics, volume one* (pp. 329–346). CRC Press

## 4.1. INTRODUCTION

Predicting wind flow within and above canopies is crucial for applications such as air quality modeling, weather forecasting, and tracking spore and pollen dispersal. Using a single-column model to simulate wind flow in canopy environments offers the advantage of computational efficiency while providing valuable physical insights of the system. For modeling often some forms of the Reynolds-averaged Navier-Stokes equation is used, where often additional assumptions are made to parameterize the canopy. Assuming horizontally homogeneous canopies, the steady space- and time-average momentum equation is

$$\frac{\partial \langle u \rangle}{\partial t} = -\frac{1}{\rho} \frac{\partial p}{\partial x} - \frac{1}{\rho} \frac{\partial \langle u' w' \rangle}{\partial z} - F_d \quad (4.1)$$

where  $\langle \rangle$  is spatial- and time-averaged operator,  $P_s = -\frac{1}{\rho} \frac{\partial p}{\partial x}$  is the pressure gradient term,  $u$  and  $w$  are the streamwise and vertical velocity respectively. The Reynolds stress  $\langle u' w' \rangle$  is typically parameterized based on gradient diffusion theory and prandtl mixing length hypothesis (Coceal & Belcher, 2004; Watanabe & Kondo, 1990). In the context of atmospheric flows without obstacles, the mixing length scale  $l$  is often parameterized as  $l = \kappa z$ , where  $\kappa$  is the von Kármán constant and  $z$  is the height above the surface. For canopy flows,  $l$  is often assumed to be lifted by the displacement height  $d$  above the ground, in the form of  $l = \kappa(z - d)$  (Wiernga, 1993). Within the canopy, the form of  $l$  is found to be different between studies. Inoue, 1963 assumed a constant value of  $l$  within the canopy to get analytical matching between the logarithmic profiles above the canopy and the exponential shaped profiles inside the canopy. This assumption is followed by many studies (Cionco, 1965; Harman & Finnigan, 2007; Macdonald, 2000). However, numerical and experimental studies suggested that  $l$  is not constant within the canopy (Castro, 2017; Watanabe & Kondo, 1990). As a result, the wind profile within the canopy does not attain an exponential shape. Hence, the validity of K-theory for canopy flows is debated. For example, Li et al., 1985 suggested the flux contribution from non-local flux transport with the presence of canopy. In equation 4.1,  $F_d$  represents the drag force exerted by the canopy elements and is dependent on the canopy density and wind velocity. Castro, 2017; Cheng and Yang, 2023 found the dependent coefficient (drag coefficient) to vary with canopy density and the height within the canopy. Likewise, drag coefficient will vary with the wind speed regime (being turbulent, quas-lamilar, or lamilar). In summary, it is debateable whether the typical parameterizations of drag force and the Reynolds stresses in single-column models are physically based and if they are representative of true 3D flows. Therefore, the motivation of this study is to provide physical insights into the parameterizations of canopy flow based on Direct Numerical Simulations (DNS). The DNSs are performed across a range of canopy densities, including a zero-density limit case (smooth wall flow). Turbulence statistics are analyzed and a new parameterization scheme is proposed. The model description and setup are given in Section 4.2. The results of DNSs are presented in Section 4.3. We discussed some parameterization insights of canopy drag forces and Reynolds stress in Section 4.3 and 4.3. The conclusion and discussion are given in Section 4.4.

Table 4.1: Overview of the simulation runs. The plant area density  $a$  is defined as the ratio of the canopy area to the total domain area, and  $a$  varies from 0 to 3.0 and  $\lambda$  is frontal area density.

cases	cylinder number	inter spacing [m]	$a$ [ $m^{-1}$ ]	$\lambda$ [-]
Smooth Wall flow (SW)	$0 \times 0$	n.a.	0	0
Very Sparse (VS)	$4 \times 4$	1.25000 $h$	0.047	0.006
Sparse (S)	$8 \times 8$	0.62500 $h$	0.189	0.024
interMediate (M)	$16 \times 16$	0.31250 $h$	0.755	0.097
Dense (D)	$32 \times 32$	0.15625 $h$	3.020	0.386

## 4.2. MODEL DESCRIPTION AND SETUP

The DNSs are performed on a open-source code [Basilisk](#), which solves the incompressible Navier-Stokes equations on adaptive Cartesian grids. The application of adaptive mesh refinement (AMR) for studying turbulent atmospheric flows is well-documented in the literature ([van Hooft et al., 2019](#); [Van Hooft et al., 2018](#)). The AMR method dynamically refines and coarsens the grid size in space and time based on the characteristics of the local flow field. Specifically, the mesh adjusts its refinement levels by comparing the local discretized error to a prescribed refinement threshold.

Table 4.1 gives the setup-overview of different canopy density cases. Canopy density is defined as ‘Dense’ (D), ‘interMediate’ (M), ‘Sparse’ (S) and ‘Very Sparse’ (VS). For each case, cylinders are placed evenly over the domain to ensure horizontal homogeneity. Fig. 4.1 illustrates the simulation domain and cylinders arrangement for the Very Sparse canopy density case. The domain size is  $L_x \times L_y \times L_z = 5h \times 5h \times h$ , with  $h = 1.024$  m, the height of the domain and the grid resolution is  $N_x \times N_y \times N_z = 256 \times 256 \times 51$ . The canopy is modeled as a collection of cylinder obstacles with a diameter of  $d = 0.08$  m and the height of canopy  $h_c = h/4$ . The plant area density  $a$  is defined as the total area of the canopy (cylinders) divided by the total volume of the canopy regime. The frontal area density  $\lambda$  is normalized by the area of the horizontal domain. The flow is driven by a constant pressure gradient in the streamwise direction, and the friction Reynolds number  $Re^*$  is set to 360. The simulations are run for a time period of  $32t_*$  to ensure that the flow reaches a statistically steady state ( $t_* = 500s$ ). We follow [Donda et al., 2015](#) to show that the resolution used in current study is sufficient for DNS of a  $Re_* = 360$  flow. In neutral steady state, the dissipation rate is assumed to equal to the average shear production.

$$\langle \epsilon \rangle = \frac{1}{h} \int_0^h u_*^2(z) \frac{\partial U}{\partial z} dz = \frac{1}{h} [Uu_*^2]_0^h - \frac{1}{h} \int_0^h U \frac{\partial u_*^2}{\partial z} dz, \quad (4.2)$$

The first term on the right-hand side drops out since  $u_* = 0$  at the top of the domain and  $U = 0$  at the bottom. Furthermore, the stress divergence term is height-independent:

$$\frac{\partial u_*^2}{\partial z} = \frac{1}{\rho} \frac{\partial P}{\partial x}, \quad (4.3)$$

The average dissipation rate is obtained:

$$\langle \epsilon \rangle \approx -\frac{1}{\rho} \frac{\partial P}{\partial x} \langle U \rangle, \quad (4.4)$$

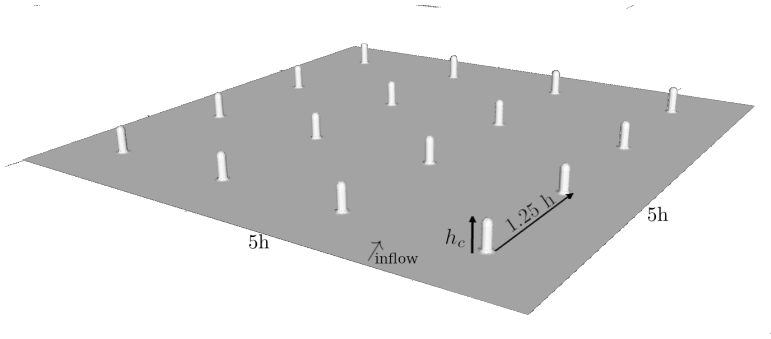


Figure 4.1: The setup of the numerical simulations for the Very Sparse canopy density case. The scale of the domain, including the height, diameter, and interspacing between cylinders.

4

Based on the average dissipation rate, the Kolmogorov length-scale  $\eta$  can be estimated:

$$\eta = \left( \frac{\langle \epsilon \rangle}{\nu^3} \right)^{-1/4} \quad (4.5)$$

The ratio between the domain height and the Kolmogorov length-scale can be estimated as well.

$$\frac{h}{\eta} = \left( \frac{\langle U \rangle}{u_{*ext}} Re_*^3 \right)^{1/4}. \quad (4.6)$$

For all cases,  $Re_* = 360$ . With a typical value for  $\langle U \rangle / u_{*ext} \approx 20$  for the wall flow case, we find  $h/\eta \approx 175$  and  $\Delta/\eta \approx 3.3$ . For canopy cases, the value of  $\langle U \rangle / u_{*ext}$  is around 10, which results in a small value of  $h/\eta \approx 146$  and  $\Delta/\eta \approx 2.8$ . This is at the limit of what we call a DNS (Nieuwstadt, 2005).

### 4.3. RESULTS FROM DNS

The first order variables (e.g.,  $u$ ,  $w$ ) of the flow field are first horizontally averaged and their turbulence fluctuations ( $u'$ ,  $w'$ ) are then calculated. The second order statistics (e.g.,  $u'w'$ ) are computed as the product of these turbulence fluctuations. Then, all statistics are averaged over the last  $2t_*$  period when the flow reaches a statistically steady state (Fig. 4.2).

#### TURBULENCE STATISTICS

First, we show the impact of canopy density on the vertical profiles of normalized velocity and Reynolds stresses. Fig. 4.3a shows that an increasing canopy density leads to a decrease of the overall wind speed, as expected. This reduction in velocities is attributed to the momentum sink effect caused by the drag exerted by the canopy elements. The canopy elements obstruct the flow, leading to a decrease in velocity throughout the profile. Additionally, vertical wind shears are observed to decrease near the surface and increase near the canopy top with increasing canopy density.

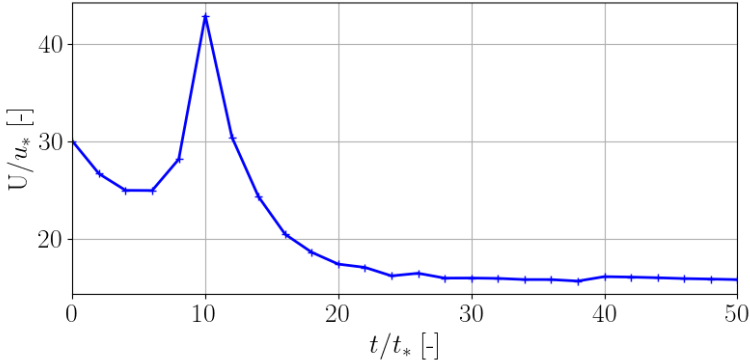


Figure 4.2: Time evolution of the turbulent kinetic energy (scaled by pressure gradient and channel depth)

The total shear stress is the sum of the Reynolds stress and viscous stress. In Fig. 4.3b, for smooth wall flow (red), the normalized Reynolds stress profile  $\langle u'w' \rangle / u_*^2$  depicts a nearly linear shape well above the surface. This can be explained by the force balance in Eq. 4.1. The viscous stress is negligible in this region due to the nearly flattened mean velocity profile and the force exerted by Reynolds stress is balanced by the constant pressure gradient. Getting close to the solid wall-surface, the viscous stress becomes dominant and Reynolds stress are dampened. The net force exerted by the Reynolds stress is negative in the upper half of the canopy height ( $z/h_c > 0.5$ ), which slows down the flow. Near the surface ( $z/h_c < 0.5$ ), the net force is positive, which accelerates the flow.

For canopy flows, the profiles of  $\langle u'w' \rangle / u_*^2$  above the canopy, where  $F_d = 0$ , align closely with the profile of smooth wall flow since this is enforced by the overall momentum balance (Eq. 4.1). However, within the canopy, the profiles of  $\langle u'w' \rangle / u_*^2$  exhibit varying degrees of decay: from the convex shape for the smooth wall and the sparse canopy cases, via semi-linear shape for the intermediate cases, to the concave shape for the dense canopy cases. The more pronounced decay of the Reynolds stress with increasing canopy density is due to the increased drag force exerted by the canopy elements. The form of canopy drag force will be discussed in detail in Section 4.3.

Fig. 4.4a illustrates the influence of the canopy density on horizontal velocity fluctuations ( $\sigma_u / u_*$ ) as a measure of local turbulent intensity. Vertical profiles of turbulence kinetic energy (not shown) have similar shapes as the profiles of  $\sigma_u / u_*$ . Near the surface ( $z/h_c < 0.5$ ), the value of  $\sigma_u / u_*$  from the smooth wall flow case suggest the vibrant fluctuations of streamwise velocity which could be a result of incoming momentum from the overlying atmosphere in combination with the effect that the no-slip surface has on the flow by the viscosity. With increasing canopy density,  $\sigma_u / u_*$  decreases near the surface since the incoming momentum is extracted by increasing canopy elements (Fig. 4.3b) and the effect of viscous stress imposed by the surface is reduced (Fig. 4.3a). However, cases of Sparse and Very Sparse canopy exhibit enhanced  $\sigma_u$  just below the canopy top ( $0.5 < z/h_c < 1$ ). This enhancement might indicate the formation of vortices generated by the canopy elements and in the case of dense canopy, the vortices are limited.

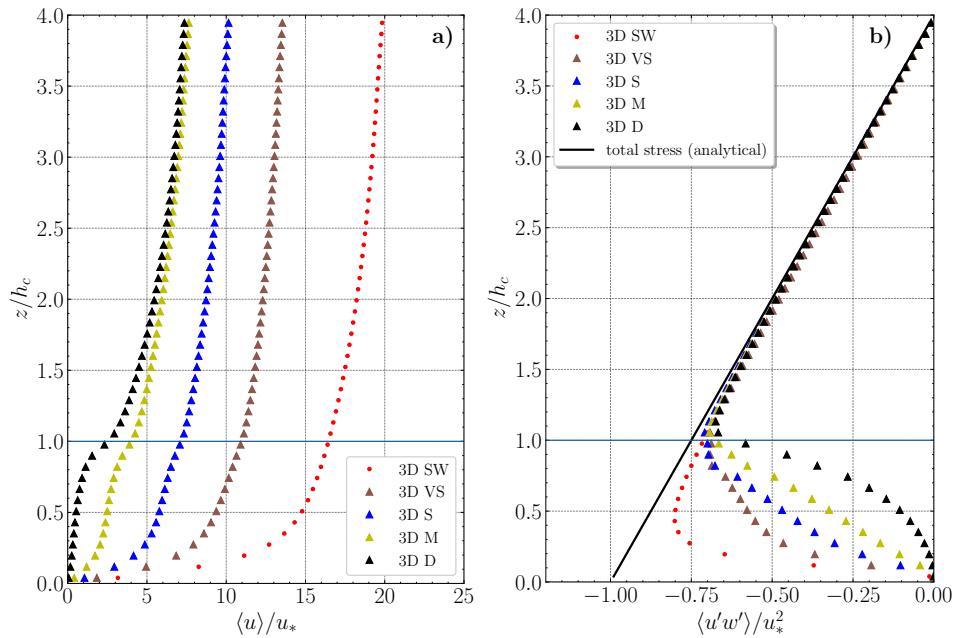


Figure 4.3: Vertical profiles of (a) mean velocity normalized by the surface friction velocity ( $\langle u \rangle / u_*$ ) and (b) mean Reynolds stress normalized by the wall stress ( $\langle u'w' \rangle / u_*^2$ ). The theoretical total stress (turbulent + viscous) is given by the black line.

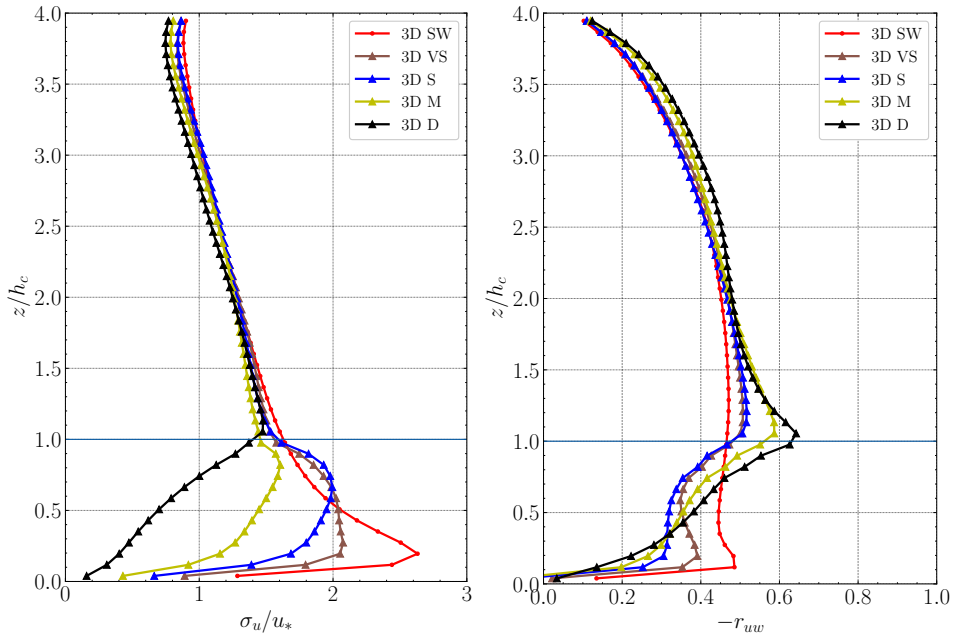


Figure 4.4: Vertical profiles of (a) the standard deviations of streamwise velocity normalized by the surface friction velocity ( $\sigma_u/u_*$ ), (b) the correlation coefficient  $-r_{uw} = -\langle u'w' \rangle / \sigma_u \sigma_w$  as a measure of “transport efficiency”

Vertical profiles of  $\langle u' w' \rangle / u_*^2$  in Fig. 4.3b show the magnitude of vertical momentum transport but not the efficiency. Fig. 4.4b shows the correlation of the horizontal and vertical velocity fluctuation  $r_{uw}$  which can be interpreted as the efficiency of vertical momentum transport. Inside the canopy ( $z/h_c < 0.5$ ), the correlation decreases with increasing canopy density. This is because obstacles block the flow and extract horizontal momentum. As such vertical velocity fluctuations do not necessarily correlate with horizontal ones. At the top of the canopy ( $0.5 < z/h_c < 1.5$ ), however, there is a strong vertical wind shear that promotes vertical momentum transport. The denser the canopy, the more prominent this effect is.

The Reynolds stress can be decomposed into four quadrants based on the sign of fluctuations: outward (Q1), ejection (Q2), inward (Q3), and sweep (Q4) (See A.2). An ejection event gives a relatively 'slow' air package from below, hence decelerates the local flow. The event of a relatively 'fast' air package going downwards is a sweep event, hence accelerating the local air flow. The ejection and sweep events are the most important events in terms of flux contribution and time fraction and as a result the mean Reynolds stress is negative (Fig. 4.3). As shown in Fig. 4.5, the relative importance of  $Q_2 + Q_4$  over other two quadrants in terms of flux contribution (S) and time fraction (D) is indeed larger than 1 for all cases. In the smooth wall flow case, the flux fraction of  $Q_2 + Q_4$  shows a peak just above the surface due to the strong wall shear stress. With increasing canopy density, the wall shear stress decreases (Fig. 4.3d), as a result, the flux fraction of  $Q_2 + Q_4$  decreases near the surface ( $z/h_c \sim 0.1$ ). In contrast, the flux fraction of  $Q_2 + Q_4$  increases near the canopy top ( $z/h_c \sim 1$ ). Due to the presence of canopy elements, the ejection and sweep events are more frequent and intense near the canopy top compared to the smooth wall flow case.

The impact of canopy density on the relative importance of sweeps, as compared to ejection events is shown in Fig. 4.6. In the smooth wall flow case (red line), ejection motions are slightly more intense and less frequent than sweep motions well above the surface ( $z/h_c > 0.2$ ). The relative slow air motions coming from below decelerate the flow, which corresponds to the negative force imposed by the Reynolds stress (Fig. 4.3b). In contrast, the sweeping motions are more intense and less frequent near the surface ( $z/h_c < 0.2$ ). This indicates the incoming fast air motions from above which accelerate the local flow. With increasing canopy density, the sweeping motions become more intense but less frequent within the canopy ( $0 < z/h_c < 1$ ). This could be attributed to how large scale turbulence interacts with the canopy. One hypothesis is that due to the obstruction of the canopy elements the probability of fast air motions going downwards is reduced. However, the presence of obstacles creates a shear layer where velocity rapidly increases with height. The pressure drop behind an obstacle stimulates occurrence of downdrafts with therefore a significant velocity increase.

#### ESTIMATED DISPLACEMENT HEIGHT

It is straightforward that the wind speed should be zero at the ground surface or at the height of roughness elements  $z_0$ . In the case of canopy flows, the zero wind speed plane is displaced at height  $d$  above the ground surface. The displacement height can be also interpreted as the apparent height of the surface as the flow experiences it (Moene & Van Dam, 2014). A rule of thumb for the displacement height is  $d = 2/3 h_c$ . However,

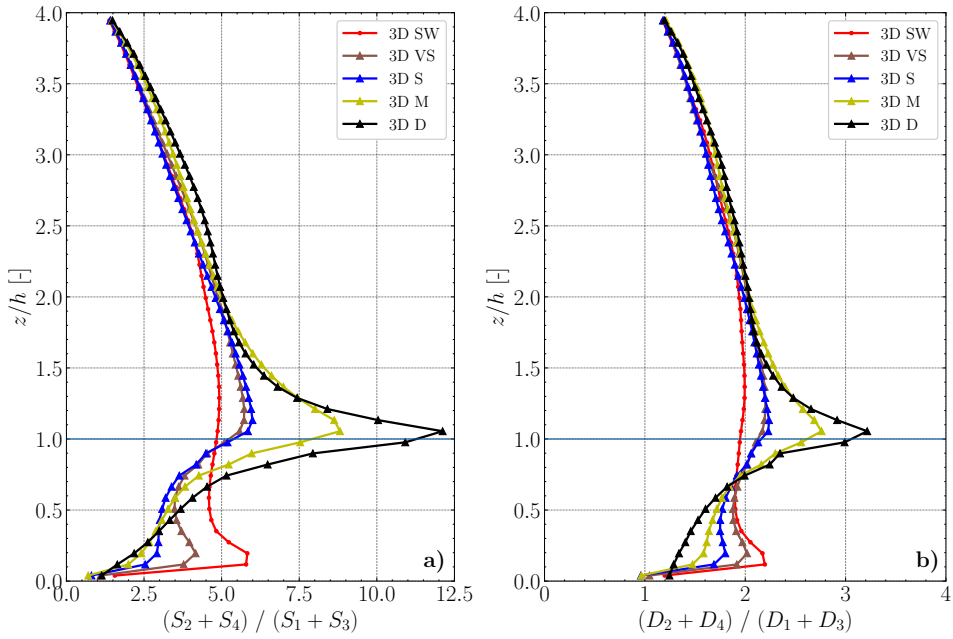


Figure 4.5: The relative importance of ejection and sweep ( $Q_2 + Q_4$ ) events over outward and inward ( $Q_1 + Q_3$ ) events in terms of flux contribution and time fraction: (a) *flux contribution* ( $S$ ) and (b) *time fraction* ( $D$ )

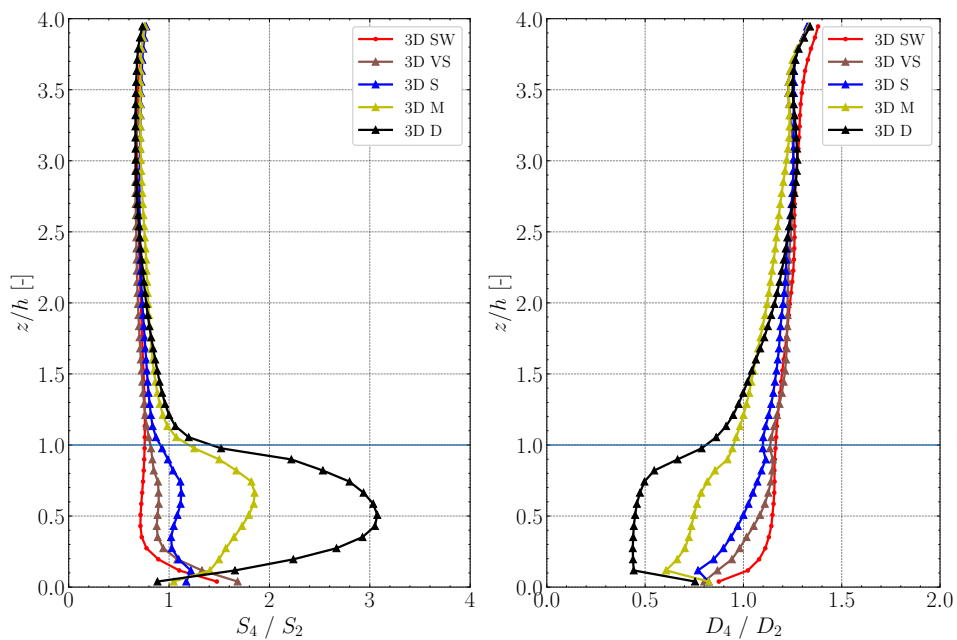


Figure 4.6: The relative importance of sweep ( $Q_4$ ) and ejection ( $Q_2$ ) events in terms of flux contribution and time fraction: (left) flux contribution and (right) time fraction

this empirical formulation does not hold for all type of canopy density, especially for the sparse canopy case. It is key to find out under which canopy density the displacement height concept is valid. The displacement height is estimated based on the validity of the logarithmic law of the wall for the layer well above the canopy layer.

$$u_{z_2} - u_{z_1} = \frac{u_*}{\kappa} \ln \frac{z_2 - d}{z_1 - d} \quad (4.7)$$

where  $z_1$  and  $z_2$  are the height of the two points,  $u_{z_1}$  and  $u_{z_2}$  are the wind speed at the two points. We found that values of displacement height for Sparse and Very Sparse case are invalid. This could be due to the fact that canopy elements are isolated and the flow still feels the presence of the ground surface. The displacement height for the dense canopy case is  $0.5 h_c$ . For other cases, the displacement height is estimated to be a negative value, which is not physically meaningful. This suggests that the displacement height concept is not valid for sparse and very sparse canopy cases.

### CANOPY DRAG FORCES

Inside of the canopy, two actors accelerate the flow: the pressure gradient force and the downward momentum influx from the fast air flowing over the canopy. Two counterforces act to slow down the flow: the viscous force by the deformation of the mean velocity field ('viscous stress') and the drag force exerted by the obstacles.

The drag forces exerted by the canopy elements are composited of the pressure drag (form drag) and viscous drag. When the flow around canopy elements is highly turbulent, the pressure drag is dominant and viscous drag is small. However, when the local flow is almost lamilar, the viscous drag becomes significant. Whether the flow is locally turbulent or not depends on the local Reynolds number and thus on the local, in-canopy wind speed. As the latter is dependent on the canopy density (Fig. 4.3), it becomes clear that the partitioning between viscous and nonviscous drag is also a function of canopy density. In literature of tall canopies (size in the order of  $\mathcal{O}(1)m$ ) or larger usually it is assumed that we are in the turbulent regime and that therefore pressure drag dominates. In a true turbulent regime, the so-called drag coefficient is defined as a constant (Kundu, 2010). Yet, some studies indicate that, even for the turbulent regime, the drag coefficient is dependent on the canopy density (Coceal & Belcher, 2004; Santiago & Martilli, 2010).

The force balance can be diagnosed from DNS results in the steady state (Figure 4.7a). Fig. 4.7a illustrates the force balance from the sparse canopy case. The drag force is computed as the residual of other forces. The drag force above the canopy is zero, and within the canopy, shows a local maximum just below the canopy-top ( $z/h_c = 0.75$ ). Fig. 4.7b shows the drag force normalized by the pressure gradient force for all cases. As expected, the drag force increases with increasing canopy density. The dense and intermediate canopy cases show largest drag at the top of the canopy, because canopy density is high and wind speed as well (Eq. 4.1 and Fig. 4.3a). The drag force is significant near the surface for the sparse and very sparse canopy cases. This is an artifact, due to the fact that the flow is not perfectly resolved in a strict sense (see discussion on Kolmogorov scale and resolution of points in the velocity profile Fig. 4.3a). The velocity profile is convex-shaped, which results in an underestimation of the magnitude of the viscous force in Fig. 4.7a near the surface, which is coming back in a positive residual in Fig. 4.7b.

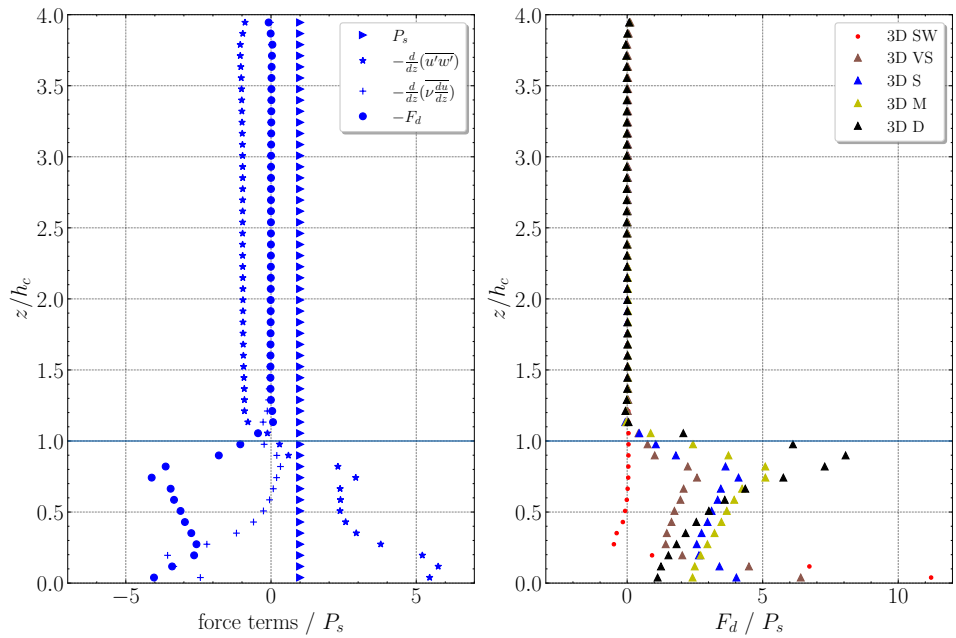


Figure 4.7: The normalized force balance for the sparse canopy case. Positive forces tend to accelerate the flow while the other forces act opposite (a) and the normalized canopy drag force for all cases in (b).

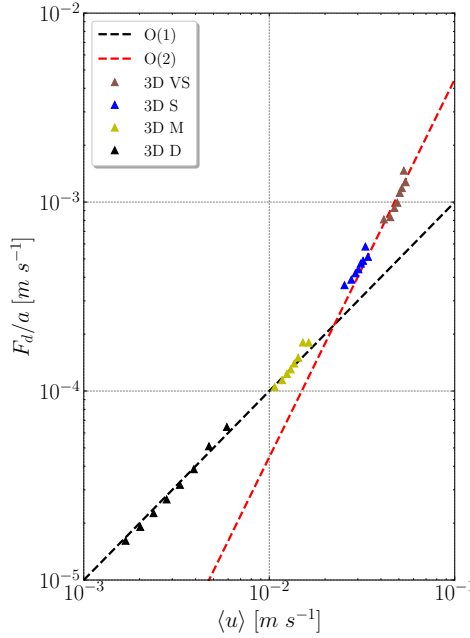


Figure 4.8: The relationship between the drag force  $F_d(z)$  normalized by plant area density  $a$  and within canopy velocity  $\langle u(z) \rangle$ . Part of the data point near the surface ( $z/h_c < 0.1$ ) and close to the canopy top ( $z/h_c > 0.9$ ) are excluded in this figure

It is a common practice to parameterize  $F_d$  in the similar form as:

$$F_d = c_d a \langle u \rangle |\langle u \rangle| \quad (4.8)$$

where  $c_d$  is the drag coefficient. Typically, for turbulent flows the drag force is expected to be a quadratic function of wind speed. Here, we however investigate whether this dependence is truly quadratic. Hence we search for a parameterisation of the form:

$$F_d = c_d a \langle u \rangle^\beta \quad (4.9)$$

where  $\beta$  is the exponent value to be diagnosed in the steady state. Fig. 4.8 illustrates the relationship between  $F_d/a$  and  $\langle u \rangle$  for all cases. For dense canopy case,  $F_d/a \sim \langle u \rangle^1$  and for sparse and very sparse canopy cases,  $F_d/a \sim \langle u \rangle^2$ . The dependence in the intermediate canopy case is in between. This suggests that the drag forced is not strictly quadratically related to the wind speed in all canopy density cases. This means besides pressure drag, also viscous drag forces appear to play a role. This has practical implications as most natural grass fields appear to be dense. Therefore, in contrast to tree canopy parameterisations, grass canopy drag appears to be linearly related to the local wind speed. In the future study, we should explore more to get the correct dependence of drag force on velocity and find the critical canopy density for the dependence transition.

### DIAGNOSING AN EFFECTIVE ‘MIXING LENGTH SCALE’

In many meteorological applications vertical turbulent mixing is parameterized using some form of mixing length theory (Prandtl mixing theory, Eq. 4.10).

$$\langle u'w' \rangle = l^2 \left| \frac{\partial \langle u \rangle}{\partial z} \right| \frac{\partial \langle u \rangle}{\partial z} \quad (4.10)$$

where  $l$  is the mixing length scale. Although a formal basis is lacking - turbulence involves multiple length scales and transport can be local as well as nonlocal - we are tempted to diagnose the ‘effective mixing length scale’ inside the canopy. If we assume validity of Eq. 4.10, the effective mixing length scale can be diagnosed from knowledge on the local fluxes and the mean wind gradients. Fig. 4.9 shows the effective mixing length scale profiles for all canopy cases. Similar to the finding in Urban Canopy modelling Cheng and Porté-Agel, 2021, the mixing length scale is found to have a local maximum near the middle of the canopy height and a local minimum near the canopy top. It is not clear so far why the apparent mixing length scale behaves like this. We hypothesize this could be likely due to the nonlocal mixing by the canopy elements (e.g., the vortices generated on the top of the canopy). We can relate this to less frequent and more intense sweeping motions showing in Fig. 4.6.

4

## 4.4. CONCLUSION AND DISCUSSION

In this study, we gain some physical insights of canopy flows based on Direct Numerical Simulations of a range of plant density cases. We include extreme cases of zero canopy density (smooth wall flow) and dense canopy to understand the impact of canopy density on turbulence statistics. The findings are summarized as follows:

- with increasing plant density, the mean velocity profiles show a systematic decrease of the overall wind speed, an intensified wind shear near the canopy top, and a decreased wind shear near the surface. This finding highlights the importance of studying the impact of canopy density on canopy flows.
- With increasing canopy elements, the ejection and sweep events are more frequent and intense near the canopy top compared to the smooth wall flow case near the surface. The sweeping events are more intense and less frequent within the canopy comparing to ejection events.
- The drag force is not strictly quadratically related to the wind speed in all canopy density cases. For Sparse and Very Sparse canopy cases,  $F_d/a \sim \langle u \rangle^2$  and for Dense canopy case,  $F_d/a \sim \langle u \rangle^1$ .
- The effective mixing length scale shows a local maximum near the half of the canopy height and local minimum near the canopy top. This could be due to the nonlocal mixing by the canopy elements.

The findings of this study provide a physical basis for the parameterization of canopy drag force and Reynolds stress. This study arranges the canopy elements in the regular pattern, which is not the case in reality. In the future study, we will investigate the impact

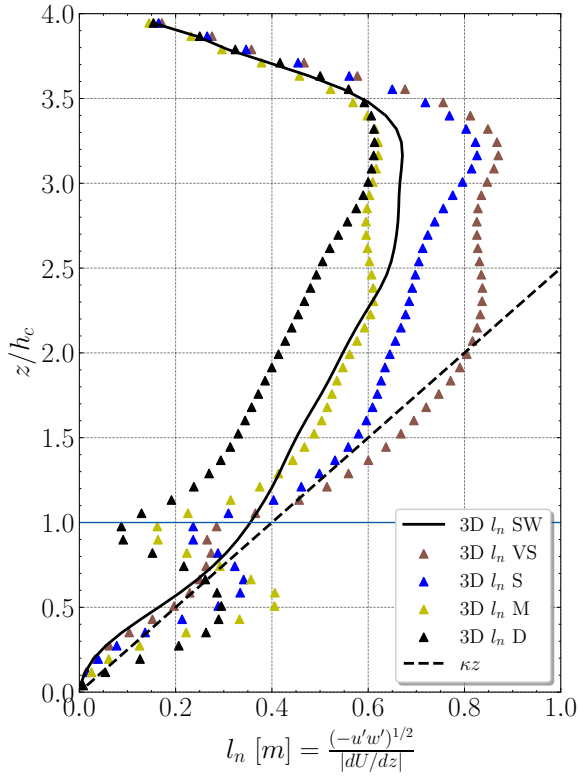


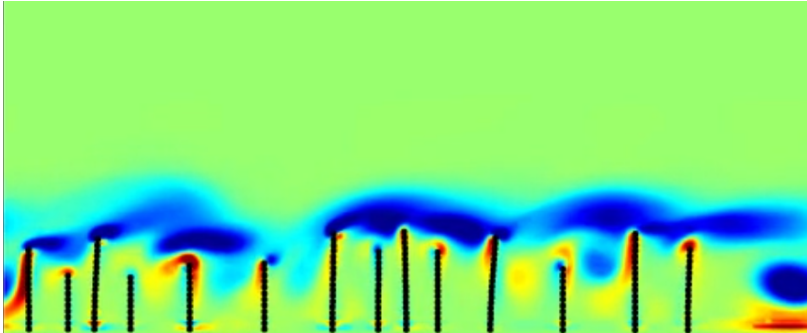
Figure 4.9: Profiles of the effective mixing length scale for all canopy cases.

of canopy element arrangement with different patterns (e.g., orientation, shape of the elements). Furthermore, the nonlocal mixing by the canopy elements is not well understood. We will explore the nonlocal mixing by the canopy elements in the future study. We will explore the possibility of 1D parameterization of canopy flow.

In this study, we investigate the impact of canopy density on turbulence statistics with solid cylinders. In reality, the grass filaments are flexible and can move with the flow. The impact of canopy flexibility on turbulence statistics is not well understood. In the future study, we will investigate the impact of canopy flexibility on turbulence statistics ([Huang et al., 2007](#)).

### Intermezzo: Towards flexible grass simulations

In Chapter 4, we simulated the grass layer with solid cylinders. In reality, grass filaments are flexible and can move with the flow. The impact of canopy flexibility on turbulence statistics is not well understood. In this intermezzo, we show the possibility of simulating flexible grass filaments using the Immersed Boundary Method (IBM). The idea behind IBM is to simulate the flow using Navier-Stokes equations with an additional force term from immersed objects, which in this case are the flexible fibers. The flexible filament is composed of a chain of Lagrangian nodes, which are constrained by multiple forces (e.g., tension forces between nodes, bending forces, gravity forces, and forces imposed by the fluid). This solver is implemented in the open-source code Basilisk based on the work of Huang et al., 2007.



Above, we present an example of a two dimensional vorticity snapshot with multiple grass filaments (dark lines) of different heights. The simulated flow is driven by a constant pressure gradient in the streamwise direction. The top of grass filaments is bending due to the flow forces. This snapshot shows the potential of simulating more realistic fluid-structure interactions in the future studies.



# 5

## CONCLUSION

### 5.1. SUMMARY OF CONCLUSIONS

In this thesis, we investigate wind machines for frost damage mitigation based on observational experiments (Chapter 2) and numerical simulations (Chapter 3). The numerical model in Chapter 3 is developed and validated based on the observational study (Chapter 2). Here, we address the research questions (RQ) put in Chapter 1 and synthesize the main findings of this thesis. After that, we discuss the implications for farmers and provide an outlook for future research.

- **RQ1: are wind machines effective in warming fruit orchards and if so, can we measure the warming range and intensity?**

We provide observational evidence of air and plant warming caused by wind machines induced air mixing (Chapter 2). By measuring the quasi-3D temperature responses over a 6.75 ha orchard, we found a 30% and 50% reduction of the local inversion strength ( $8^{\circ}\text{C}$ ) over 2.66 ha and 0.45 ha, respectively, within the canopy around the wind machine. On average, wind machine operation raised in-canopy temperature by 3 K within 40 minutes from starting machine operation. Furthermore, to the best of our knowledge, Chapter 2 is the first study to detail the dynamic warming effects of wind machines with high resolution over such a large area.

- **RQ2: is the mixing and warming pattern different upwind and downwind from the wind machine, can we explain this difference?**

Both observations and numerical model proved (Chapter 2 and 3) that the background wind despite being very light ( $0.2\text{ m s}^{-1}$ ) causes a strong difference in the warming of air and leaves upstream in comparison to downstream of the WM. First, there is the advection effect, as  $0.2\text{ m s}^{-1}$  implies a 'plume drift' of 60 m over a rotation period of 5 minutes. Also, a warming difference upstream and

downstream occurs due to interaction between the jet and the background wind. When jets flow against the background wind, wind drag resistance is felt, causing a delay in arrival of the warming plumes relative to the jet and convergence of airflows. When jets flow along the background wind, warming plumes travel further, creating wave-like patterns downstream of the wind machine. As a result, the downstream warming range extends much further than the upstream range (550 m compared to 150 m). In cross-stream direction, both warming ranges for air and leaves extend to approximately 250 meters on each side.

- **RQ3: can we quantify the momentum and heat transport during wind machine operation? what are the main turbulent motions during operation?**

We quantified the effect of wind machine operation on flux transport based on Quadrant-Hole analysis (Chapter 2). We found that flux transport during operation is dominated by sweeping and ejections motions. Downdrafts of warm air and updrafts of cool air are intermittent but very effective in vertical heat exchange. This feature makes wind machines highly effective in increasing canopy airspace temperature to mitigate frost damage.

- **RQ4: is it possible to build a numerical model of the full system, that is both realistic in comparison with observation, but also simple in its process descriptions?**

We developed a numerical model to simulate the warming effects of wind machines in orchards (e.g., plant-tissue temperatures) (Chapter 3). The model is based on the Large Eddy Simulation (LES) method and incorporates a canopy model, an air-plant-tissue heat exchange model, and a wind machine model. We compared simulation results with measurements taken at a 9 m tower and a horizontal slice over a 6.75 ha orchard (Chapter 2). The numerical model in Chapter 3 can reproduce the mixing and warming effects of the WM operation observed in the orchard canopy. The model provides a useful surrogate of outdoor reality with respect to wind machine operation in orchards

In Chapter 4, an additional study was conducted to numerically represent a grass canopy using so-called Direct Numerical simulations. Some physical insights are gained from simulations for a range of plant density cases. As expected, we found that with increasing plant density, the mean velocity profiles show a systematic decrease of the overall wind speed, an intensified wind shear near the canopy top, and a decreased wind shear near the surface. Furthermore, we found that the parameterization of the drag force is not strictly quadratically related to the wind speed in all canopy density cases. For Sparse and Very Sparse canopy cases,  $F_d/a \sim \langle u \rangle^2$  (cf. 'turbulent' form drag) and for Dense canopy case,  $F_d/a \sim \langle u \rangle^1$  (cf. viscous drag). The effective mixing length scale used to parameterize the Reynolds stress is found not to be a constant value, which is frequently assumed in the literature. The effective mixing length scale shows a local maximum near the half of the canopy height and local minimum near the canopy top.

## 5.2. IMPLICATIONS FOR THE AGRICULTURAL SECTOR AND FARMERS

As the title of this thesis suggests, the main goal (apart from the science behind it) is to reduce frost damage in agricultural fields by using wind machines. In the course of the research for this book, we came into contact with fruit growers in the Netherlands as well as winegrowers in France and Italy. As shown in the covers of Chapter 1 and 2, these farmers share similar concerns: they worry about frost damage to their crops, question whether the installed wind machines are effective, and wonder how many wind machines are necessary to protect their orchards. The results of this thesis address these concerns and provide valuable insights to help the agricultural sector and farmers make better-informed decisions.

- **Effectiveness of Wind Machines:** Wind machines are indeed *effective* in warming fruit orchards, although their performance can vary with different operational practices and/or under different weather conditions. In Chapter 2 and 3, we observed that the warming spots are mainly located downstream of the wind machine. It is recommended for farmers to place the wind machine in the direction of the prevailing wind during typical cold nights to maximize the warming range. For example, in The Netherlands, clear-sky cold spring nights usually coincide with high-pressure synoptical systems with (light) winds coming from the East or North-East. Farmers should take this in to consideration when installing their wind machines. Using the developed numerical model, we can now test various operational modes of wind machines and provide guidelines for optimal operation in the future.
- **Data of Yield Protection:** To quantify the effectiveness of wind machines on yield protection, farmers using wind machines are encouraged to record yield data relative to the distance from the wind machine, general weather conditions, and the specific wind machine operation mode. This data will significantly contribute to improving wind machine operation for frost damage mitigation and to assess future cost effectiveness.
- **Forecasting and Monitoring:** Accurate prediction of frost events is crucial as it gives farmers time to make decisions and prepare for frost mitigation (e.g., moving mobile wind machines into position ahead of time, adding additional sprinklers). We attempted to forecast frost events using Weather Research & Forecasting Model (WRF; See preliminary results in Fig. 5.1). During the night, temperatures are non-uniform in space and time. It is recommended to use multiple temperature sensors across the field and at different heights. Our project is developing a 3D temperature monitoring system to help farmers make better decisions on where to put extra efforts in reducing the lower temperatures. We illustrate this by showing distributed temperature sensors along a vertical cable in Fig. 5.2. Additionally, it is recommended to monitor plant temperatures alongside air temperatures to decide when to start the wind machines.
- **Misconceptions about Wind Machines:** One common misconception is that wind machine are only effective under strong inversion conditions and otherwise not.

Based on our numerical results (not shown), we found that the warming efficiency of wind machines is not linearly dependent on the inversion strength. Under weak inversion conditions, wind machines can generate strong air jets that accelerate the heat exchange process, even when the temperature of jets sweeping over the plant-tissue is not much higher than the plant-tissue itself. Additionally, weak or zero inversion conditions are often accompanied by cloudy skies. During cloudy nights, plants are less likely to suffer frost damage due to incoming longwave radiation. Furthermore, in very strong inversion conditions, wind machines may not be able to break the inversion layer due to strong buoyancy suppression. In the future, we will investigate the optimal operational modes of wind machines for both very strong and weak inversion conditions.

### 5.3. RESEARCH OUTLOOK

The work in this thesis makes a contribution to quantifying, understanding, and predicting the warming effects of wind machines in orchards (summarized in Sec. 5.1). In general, the measurement data (i.e., the quasi-3D temperature responses over a 6.75 ha orchard) can be used to benchmark future numerical models for wind machine applications (Chapter 2). The numerical model developed can be used to explore various frost mitigation scenarios (Chapter 3). However, several aspects warrant further investigation to enhance our understanding of wind machine operation in orchards and improve frost damage mitigation strategies.

- **More field studies:** Future research should include long-term field studies across diverse orchards and weather conditions. Specifically, it is recommended to employ the 3D temperature-grid system (Fig. 5.2) developed in our project in orchards during frost seasons. This autonomous system can provide detailed 3D temperature data in canopy layers, offering a significant improvement compared to the traditional practice of using a single weather station for the orchard. Additionally, it helps to monitor the temperature responses during wind machine operation over extended periods.

Investigating a range of wind machine types and operational modes will provide a more comprehensive dataset for model development and validation. For example, the Quincy vineyard, which operates about 60 wind machines over an area of 700 hectares (Le Cap, 2023), presents a unique opportunity to study various wind machines, different operational practices, and their combined warming effects.

Moreover, the advancement of fiber-optic sensing techniques enables obtaining temperature and wind speed measurements at high resolutions and over large spatial areas (Freundorfer et al., 2021; van Ramshorst et al., 2020). These coupled measurements will help to quantify the wind structure of the jet from the wind machine and the heterogeneous air-plant heat exchange in orchards. Together this will provide a more detailed validation dataset for model development.

- **Advancing the numerical model:** The numerical model developed in this thesis can be further improved in several aspects. Firstly, the leaf energy balance model

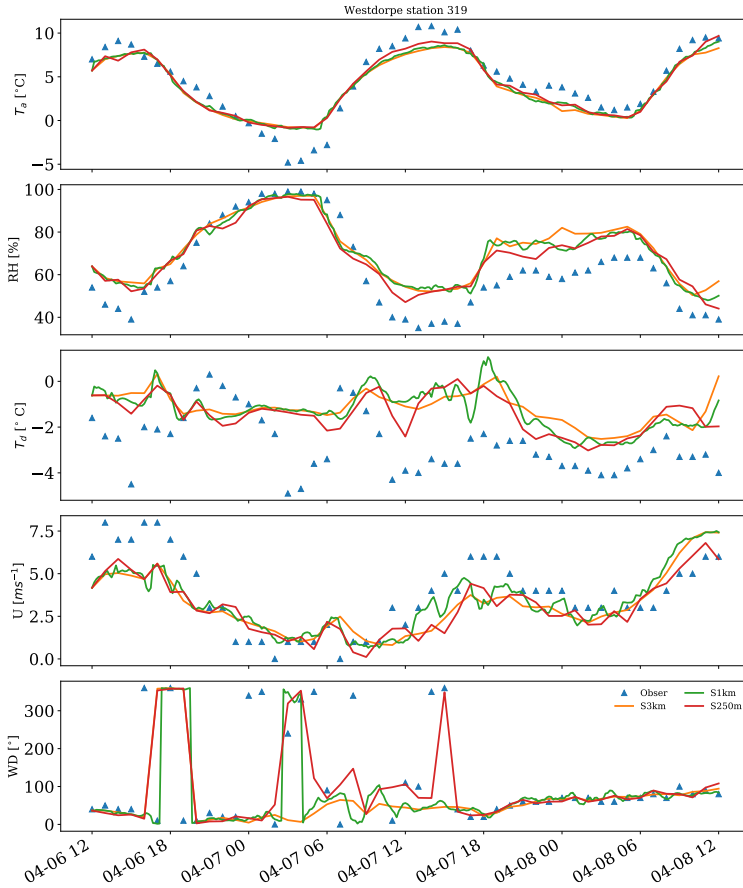


Figure 5.1: The prediction of air temperatures, relative humidity, dew point temperatures, 10 m wind speeds, and 10 m wind directions from the Weather Research and Forecasting (WRF) model were compared with data from Westdorpe weather station operated by Koninklijk Nederlands Meteorologisch Instituut (KNMI) on April 6, 2012, over a two-day period. The WRF simulations were driven by the fifth generation of global climate reanalysis data (ERA5). This plot shows that the modelled results are insensitive to the horizontal grid resolutions (250 m, 1 km, and 3 km). The overall predicted trend by WRF agreed well with the measurements from the weather station, except for extreme low temperatures (i.e., frost events). This discrepancy is likely related to the numerical representation of the surface boundary condition in WRF and the longwave radiation scheme. These results demonstrate the great potential for improving frost prediction in general weather forecast models and highlight the need to understand the frost conditions on a small scale using large eddy simulation models, as discussed in Chapter 3.



5

Figure 5.2: The temperature module, as the prototype of a future full 3D temperature-grid design, is composed of six temperature sensors over 3 m height and a data logger for six sensors. Apart from the module, there is a central data collector to collect data from all modules. The autonomous temperature modules have been tested in the greenhouse environment (Delphy laboratories Randwijk) for three months. Note that maximum temperatures over 50 degrees were recorded. During the testing period, the power unit generates 10mA (in the shade) to 100mA (full sunlight) of current. Additionally, the modules can be remotely monitored and maintained. This promises future low-cost, lower-power, wireless, distributed sensor networks. The hardware part of this temperature module is developed by Lukasz Pakula, with Yi Dai involved in the design, testing and maintenance process.

can be enhanced by incorporating the scattering and reflection of radiation using a more comprehensive canopy radiation model (Guenther et al., 2006; E. G. Patton et al., 2016). Currently, the surface boundary condition used in the model is an empirical prescription rather than the traditional Monin-Obukhov Similarity Theory (MOST), as MOST does not work well with heterogeneous rotating warming plumes during wind machine operation. Future studies should rigorously investigate the surface boundary condition in the presence of nonstationary and heterogeneous heat sources.

Additionally, the wind machine parameterization can be further developed and improved. The current model uses a simple actuator disk model with a uniform force prescribed over the disk. In reality, the force distribution is not uniform and depends on the blade design (e.g., material, shape, pitch angle). Future improvements should incorporate the factors of blade design into the wind machine model, potentially using the actuator line model to simulate blade rotation and force distribution.

- **Options with the numerical model:** The numerical model developed in this thesis can be used to explore various scenarios for frost damage mitigation. From the perspective of improving the warming effectiveness of a single wind machine, this model can investigate different types and operational modes. Our study finds that the warming plumes travel further with the help of the background wind. This suggests that other WM operational modes (e.g., sweeping half circles along the wind) may be equally or more efficient. In Italy and France, the grape fields are mostly located on hillsides. The numerical model can be used to investigate the warming effects of mitigation methods on sloping terrains.

Furthermore, the combined warming effects of multiple wind machines should be investigated to address practical questions such as: How many wind machines are necessary to protect a certain area? What is the optimal distance between wind machines? Do they profit from another wind machine due to plume drift? Furthermore, other frost mitigation methods can be numerically examined. For example, Fig. 5.3 shows a numerical experiment on the warming effects of heaters in orchards using the same model framework. This numerical model opens possibilities for developing anti-frost wind machines and new frost mitigation methods.

With that, we conclude this thesis. I hope that the results and insights presented in this thesis will help frost damage mitigation for farmers and the agricultural sector.

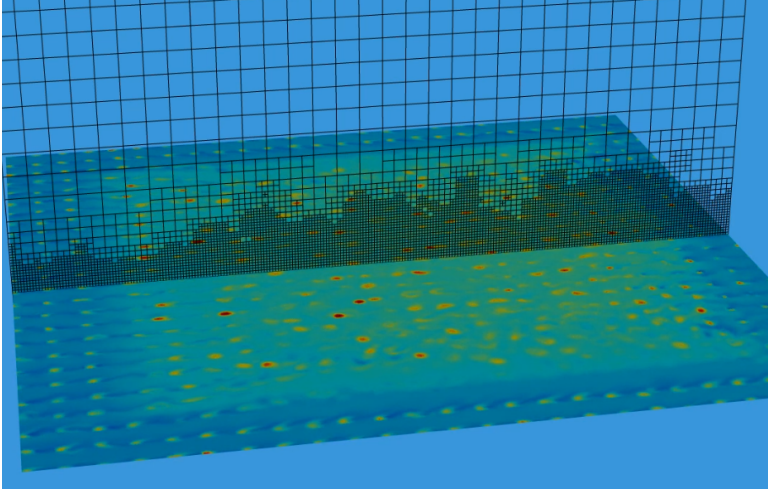


Figure 5.3: An illustration of the numerical experiment on the warming effects of heaters in orchards. The red and blue colors over the horizontal plane indicate the warm and cold air plumes induced by the heaters. The vertical grids show local refinement near the heaters. Our preliminary results show that heaters alone are not effective in warming up the orchard likely due to large heat loss directly to the sky caused by strong buoyancy effects. However, this finding needs further validation in the future studies.

# BIBLIOGRAPHY

- Araya, G., Castillo, L., Meneveau, C., & Jansen, K. (2011). A dynamic multi-scale approach for turbulent inflow boundary conditions in spatially developing flows. *Journal of Fluid Mechanics*, 670, 581–605. <https://doi.org/10.1017/S0022112010005616>
- Bates, E. M., Lombard, P. B., et al. (1978). Evaluation of temperature inversions and wind machine on frost protection in southern oregon. *Oregon Agricultural Experiment Station*.
- Battany, M. C. (2012). Vineyard frost protection with upward-blowing wind machines. *Agricultural and forest meteorology*, 157, 39–48. <https://doi.org/10.1016/j.agrformet.2012.01.009>
- Beyá-Marshall, V., Herrera, J., Santibáñez, F., & Fichet, T. (2019). Microclimate modification under the effect of stationary and portable wind machines. *Agricultural and forest meteorology*, 269, 351–363. <https://doi.org/10.1016/j.agrformet.2019.01.042>
- Boeke, J., Dai, Y., Schilperoord, B., van de Wiel, B. J., & ten Veldhuis, M.-C. (2023). Plant-atmosphere heat exchange during wind machine operation for frost protection. *Agricultural and Forest Meteorology*, 330, 109312. <https://doi.org/10.1016/j.agrformet.2023.109312>
- Brooks, F., Rhoades, D., Leonard, A., et al. (1952). Wind machines: 90 and 15 bhp machines compared for frost protection at riverside. *California Agriculture*, 6(8), 7–8.
- Brooks, F., Rhoades, D., Leonard, A., et al. (1954). Wind machine tests in citrus: Frost protection studies in 1954 confirmed earlier findings next to be investigated in deciduous trees. *California Agriculture*, 8(8), 8–10.
- Brooks, F., Schultz, H., et al. (1958). Orchard heating effectiveness: Protection against radiation frosts by orchard heaters and by wind machines alone and in combination compared. *California Agriculture*, 12(8), 4–13.
- Brunet, Y. (2020). *Turbulent flow in plant canopies: Historical perspective and overview*. Springer.
- Brunet, Y., Finnigan, J., & Raupach, M. (1994). A wind tunnel study of air flow in waving wheat: Single-point velocity statistics. *Boundary-Layer Meteorology*, 70(1-2), 95–132. <https://doi.org/10.1007/BF00712525>
- Castro, I. P. (2017). Are urban-canopy velocity profiles exponential? *Boundary-Layer Meteorology*, 164(3), 337–351.
- Chahine, A., Dupont, S., Sinfort, C., & Brunet, Y. (2014). Wind-flow dynamics over a vineyard. *Boundary-layer meteorology*, 151, 557–577. <https://doi.org/10.1007/s10546-013-9900-4>
- Cheng, W.-C., & Porté-Agel, F. (2021). A simple mixing-length model for urban canopy flows. *Boundary-Layer Meteorology*, 181(1), 1–9.

- Cheng, W.-C., & Yang, Y. (2023). Scaling of flows over realistic urban geometries: A large-eddy simulation study. *Boundary-Layer Meteorology*, 186(1), 125–144.
- Cionco, R. M. (1965). A mathematical model for air flow in a vegetative canopy. *Journal of Applied Meteorology and Climatology*, 4(4), 517–522.
- Coceal, O., & Belcher, S. (2004). A canopy model of mean winds through urban areas. *Quarterly Journal of the Royal Meteorological Society*, 130(599), 1349–1372.
- Dai, Y., Basu, S., Maronga, B., & de Roode, S. R. (2021). Addressing the grid-size sensitivity issue in large-eddy simulations of stable boundary layers. *Boundary-Layer Meteorology*, 178, 63–89. <https://doi.org/10.1007/s10546-020-00558-1>
- Dai, Y., Boeke, J., Schilperoort, B., ten Veldhuis, M.-C., & van de Wiel, B. J. (2023). Wind machines for frost damage mitigation: A quantitative 3d investigation based on observations. *Agricultural and Forest Meteorology*, 338, 109522. <https://doi.org/10.1016/j.agrformet.2023.109522>
- Dai, Y., van Hooft, A., Patton, E. G., Boeke, J., van der Linden, S., ten Veldhuis, M.-C., & van de Wiel, B. J. (2024). Integrated large-eddy simulation for modeling plant-tissue warming induced by wind machines in an orchard canopy. *Agricultural and Forest Meteorology*, 356, 110175. <https://doi.org/10.1016/j.agrformet.2024.110175>
- Davis, R. (1977). An evaluation of frost protection provided by a wind machine in the okanagan valley of british columbia. *Canadian Journal of Plant Science*, 57(1), 71–74.
- Deardorff, J. W. (1980). Stratocumulus-capped mixed layers derived from a three-dimensional model. *Boundary-layer meteorology*, 18, 495–527. <https://doi.org/10.1007/BF00119502>
- des Tombe, B., Schilperoort, B., & Bakker, M. (2020). Estimation of temperature and associated uncertainty from fiber-optic raman-spectrum distributed temperature sensing. *Sensors*, 20(8), 2235.
- des Tombe, B. F., & Schilperoort, B. (n.d.). *Python distributed temperature sensing calibration* (Version v1.0.2). <https://doi.org/10.5281/zenodo.1410097>
- (DHPC), D. H. P. C. C. (2022). DelftBlue Supercomputer (Phase 1).
- Donda, J., Van Hooijdonk, I., Moene, A., Jonker, H., Van Heijst, G., Clercx, H., & Van de Wiel, B. (2015). Collapse of turbulence in stably stratified channel flow: A transient phenomenon. *Quarterly Journal of the Royal Meteorological Society*, 141(691), 2137–2147.
- Dwyer, M. J., Patton, E. G., & Shaw, R. H. (1997). Turbulent kinetic energy budgets from a large-eddy simulation of airflow above and within a forest canopy. *Boundary-Layer Meteorology*, 84, 23–43. <https://doi.org/10.1023/A:1000301303543>
- Evans, R. G. (1999). Frost protection in orchards and vineyards. *Washington State Univ. Coop. Ext. Pullman*.
- Evans, R. G. (2000). The art of protecting grapevines from low temperature injury. *Proc. ASEV 50th Anniversary Annual Mtg., Seattle WA*, 60–72.
- Finnigan, J. J., Shaw, R. H., & Patton, E. G. (2009). Turbulence structure above a vegetation canopy. *Journal of Fluid Mechanics*, 637, 387–424. <https://doi.org/10.1017/S0022112009990589>
- Fisher, K. H. (2009). Reducing cold injury to grapes through the use of wind machines.

- Freundorfer, A., Lapo, K., Schneider, J., & Thomas, C. K. (2021). Distributed sensing of wind direction using fiber-optic cables. *Journal of Atmospheric and Oceanic Technology*, 38(10), 1871–1883. <https://doi.org/10.1175/JTECH-D-21-0019.1>
- Frith, H. (1951). Frost protection in orchards using air from the temperature inversion layer. *Australian Journal of Agricultural Research*, 2(1), 24–42.
- Goodall, G., Angus, D., Leonard, A., Brooks, F., et al. (1957). Effectiveness of wind machines: Frost protection by ramjet or conventional wind machines in deciduous orchards depends on the strength of the inversion. *California Agriculture*, 11(8), 7–9.
- Guenther, A., Karl, T., Harley, P., Wiedinmyer, C., Palmer, P. I., & Geron, C. (2006). Estimates of global terrestrial isoprene emissions using megan (model of emissions of gases and aerosols from nature). *Atmospheric Chemistry and Physics*, 6(11), 3181–3210. <https://doi.org/10.5194/acp-6-3181-2006>
- Harman, I. N., & Finnigan, J. J. (2007). A simple unified theory for flow in the canopy and roughness sublayer. *Boundary-layer meteorology*, 123, 339–363.
- Hersbach, H., Bell, B., Berrisford, P., Biavati, G., Horányi, A., Muñoz Sabater, J., Nicolas, J., Peubey, C., Radu, R., Rozum, I., Schepers, D., Simmons, A., Soci, C., Dee, D., & Thépaut, J.-N. (2023). ERA5 hourly data on pressure levels from 1940 to present. climate change service (C3S) climate data store (CDS) [Accessed on 01-SEP-2023]. <https://doi.org/10.24381/cds.bd0915c6>
- Heus, T., van Heerwaarden, C. C., Jonker, H. J., Pier Siebesma, A., Axelsen, S., Van Den Dries, K., Geoffroy, O., Moene, A., Pino, D., De Roode, S., et al. (2010). Formulation of the dutch atmospheric large-eddy simulation (DALES) and overview of its applications. *Geoscientific Model Development*, 3(2), 415–444. <https://doi.org/10.5194/gmd-3-415-2010>
- Heusinkveld, V. W., van Hooft, J. A., Schilperoort, B., Baas, P., van de Wiel, B. J., et al. (2020). Towards a physics-based understanding of fruit frost protection using wind machines. *Agricultural and Forest Meteorology*, 282, 107868.
- Hu, Y., Asante, E. A., Lu, Y., Mahmood, A., Buttar, N. A., & Yuan, S. (2018). Review of air disturbance technology for plant frost protection. *International Journal of Agricultural and Biological Engineering*, 11(3), 21–28.
- Huang, W.-X., Shin, S. J., & Sung, H. J. (2007). Simulation of flexible filaments in a uniform flow by the immersed boundary method. *Journal of computational physics*, 226(2), 2206–2228.
- Inoue, E. (1963). On the turbulent structure of airflow within. *Journal of the Meteorological Society of Japan. Ser. II*, 41(6), 317–326.
- Inouye, D. W. (2008). Effects of climate change on phenology, frost damage, and floral abundance of montane wildflowers. *Ecology*, 89(2), 353–362.
- Katul, G. G., Mahrt, L., Poggi, D., & Sanz, C. (2004). One-and two-equation models for canopy turbulence. *Boundary-layer meteorology*, 113, 81–109. <https://doi.org/10.1023/B:BOUN.0000037333.48760.e5>
- Kimura, K., Yasutake, D., Nakazono, K., & Kitano, M. (2017). Dynamic distribution of thermal effects of an oscillating frost protective fan in a tea field. *Biosystems Engineering*, 164, 98–109. <https://doi.org/10.1016/j.biosystemseng.2017.09.010>

- Klemp, J., & Lilly, D. (1978). Numerical simulation of hydrostatic mountain waves. *Journal of the Atmospheric Sciences*, 35(1), 78–107. [https://doi.org/10.1175/1520-0469\(1978\)035<0078:NSOHW>2.0.CO;2](https://doi.org/10.1175/1520-0469(1978)035<0078:NSOHW>2.0.CO;2)
- Lamichhane, J. R. (2021). Rising risks of late-spring frosts in a changing climate. *Nature Climate Change*, 11(7), 554–555. <https://doi.org/10.1038/s41558-021-01090-x>
- Le Cap, C. (2023). *Numerical simulations and field measurements of frost events in a vineyard equipped with wind machines: Application to the quincy vineyard* [Doctoral dissertation, Université de Rennes].
- Lee, X., & Barr, A. G. (1998). Climatology of gravity waves in a forest. *Quarterly Journal of the Royal Meteorological Society*, 124(549), 1403–1419. <https://doi.org/10.1002/qj.49712454904>
- Lee, X., & Black, T. A. (1993). Atmospheric turbulence within and above a douglas-fir stand. part ii: Eddy fluxes of sensible heat and water vapour. *Boundary-Layer Meteorology*, 64(4), 369–389.
- Li, Z., Miller, D., & Lin, J. (1985). A first-order closure scheme to describe counter-gradient momentum transport in plant canopies. *Boundary-layer meteorology*, 33, 77–83. <https://doi.org/10.1007/BF00137037>
- Liu, Q., Piao, S., Janssens, I. A., Fu, Y., Peng, S., Lian, X., Ciais, P., Myneni, R. B., Peñuelas, J., & Wang, T. (2018). Extension of the growing season increases vegetation exposure to frost. *Nature communications*, 9(1), 426. <https://doi.org/10.1038/s41467-017-02690-y>
- Liubchenkova, N. (2021). Euronews: 'historic' bout of frost decimates french winemakers' harvest [Accessed: 2022-05-09].
- Lu, S., & Willmarth, W. (1973). Measurements of the structure of the reynolds stress in a turbulent boundary layer. *Journal of Fluid Mechanics*, 60(3), 481–511.
- Macdonald, R. (2000). Modelling the mean velocity profile in the urban canopy layer. *Boundary-Layer Meteorology*, 97, 25–45.
- Martinez, L., Leonardi, S., Churchfield, M., & Moriarty, P. (2012). A comparison of actuator disk and actuator line wind turbine models and best practices for their use. *50th AIAA Aerospace Sciences Meeting including the New Horizons Forum and Aerospace Exposition*, 900. <https://doi.org/10.2514/6.2012-900>
- Moene, A. F., & Van Dam, J. C. (2014). *Transport in the atmosphere-vegetation-soil continuum*. Cambridge University Press.
- Munters, W., Meneveau, C., & Meyers, J. (2016). Turbulent inflow precursor method with time-varying direction for large-eddy simulations and applications to wind farms. *Boundary-layer meteorology*, 159, 305–328. <https://doi.org/10.1007/s10546-016-0127-z>
- Nieuwstadt, F. (2005). Direct numerical simulation of stable channel flow at large stability. *Boundary-layer meteorology*, 116(2), 277–299.
- Oliver, C. (2012). Near field mixing of negatively buoyant jets.
- Patton, E. G., Sullivan, P. P., Shaw, R. H., Finnigan, J. J., & Weil, J. C. (2016). Atmospheric stability influences on coupled boundary layer and canopy turbulence. *Journal of the Atmospheric Sciences*, 73(4), 1621–1647. <https://doi.org/10.1175/JAS-D-15-0068.1>

- Patton, E., & Finnigan, J. (2013). Canopy turbulence, chap. 24. In *Handbook of environmental fluid dynamics, volume one* (pp. 329–346). CRC Press.
- Perry, K. B. (1998). Basics of frost and freeze protection for horticultural crops. *HortTechnology*, 8(1), 10–15.
- Raupach, M. (1981). Conditional statistics of reynolds stress in rough-wall and smooth-wall turbulent boundary layers. *Journal of Fluid Mechanics*, 108, 363–382.
- Raupach, M., Coppin, P., & Legg, B. (1986). Experiments on scalar dispersion within a model plant canopy part I: The turbulence structure. *Boundary-Layer Meteorology*, 35(1), 21–52.
- Rhoades, D., Brooks, F., Leonard, A., Schultz, H., et al. (1955). Frost protection in almonds: Wind machine studies in 1955 frost season indicate protection in mature almond orchards below that obtained in citrus. *California Agriculture*, 9(8), 3–14.
- Ribeiro, A. C., De Melo-Abreu, J. P., & Snyder, R. L. (2006). Apple orchard frost protection with wind machine operation. *Agricultural and Forest Meteorology*, 141(2–4), 71–81. <https://doi.org/10.1016/j.agrformet.2006.08.019>
- Santiago, J., & Martilli, A. (2010). A dynamic urban canopy parameterization for mesoscale models based on computational fluid dynamics reynolds-averaged navier–stokes microscale simulations. *Boundary-layer meteorology*, 137, 417–439.
- Schilperoort, B., Coenders-Gerrits, M., Jiménez Rodríguez, C., van der Tol, C., Van De Wiel, B., & Savenije, H. (2020). Decoupling of a douglas fir canopy: A look into the subcanopy with continuous vertical temperature profiles. *Biogeosciences*, 17(24), 6423–6439.
- Schuepp, P. (1993). Tansley review no. 59. leaf boundary layers. *New Phytologist*, 477–507. <https://doi.org/10.1111/j.1469-8137.1993.tb03898.x>
- Shaw, R., Den Hartog, G., & Neumann, H. (1988). Influence of foliar density and thermal stability on profiles of reynolds stress and turbulence intensity in a deciduous forest. *Boundary-Layer Meteorology*, 45, 391–409. <https://doi.org/10.1007/BF00124010>
- Siegmund, P. (2022). KNMI climate report growing season has longer and longer frost [Accessed: 2022-05-09].
- Snyder, R. L., Abreu, J. d. M., Matulich, S., et al. (2005). Frost protection: Fundamentals, practice, and economics.
- Thomas, C. K., Kennedy, A. M., Selker, J. S., Moretti, A., Schroth, M. H., Smoot, A. R., Tufillaro, N. B., & Zeeman, M. J. (2012). High-resolution fibre-optic temperature sensing: A new tool to study the two-dimensional structure of atmospheric surface-layer flow. *Boundary-layer meteorology*, 142(2), 177–192.
- Torkelson, G., Price, T. A., & Stoll, R. (2022). Momentum and turbulent transport in sparse, organized vegetative canopies. *Boundary-Layer Meteorology*, 184(1), 1–24. <https://doi.org/10.1007/s10546-022-00698-6>
- Troldborg, N., Sorensen, J. N., & Mikkelsen, R. (2007). Actuator line simulation of wake of wind turbine operating in turbulent inflow. *Journal of physics: conference series*, 75(1), 012063. <https://doi.org/10.1088/1742-6596/75/1/012063>
- van Hooff, J. A., Baas, P., van Tiggelen, M., Anson, C., & van de Wiel, B. J. H. (2019). An idealized description for the diurnal cycle of the dry atmospheric boundary

- layer. *Journal of the Atmospheric Sciences*, 76(12), 3717–3736. <https://doi.org/10.1175/JAS-D-19-0023.1>
- van Ramshorst, J. G. V., Coenders-Gerrits, M., Schilperoort, B., van de Wiel, B. J. H., Izett, J. G., Selker, J. S., Higgins, C. W., Savenije, H. H. G., & van de Giesen, N. C. (2020). Revisiting wind speed measurements using actively heated fiber optics: A wind tunnel study. *Atmospheric Measurement Techniques*, 13(10), 5423–5439. <https://doi.org/10.5194/amt-13-5423-2020>
- Van de Wiel, B. J., Vignon, E., Baas, P., Van Hooijdonk, I. G., Van der Linden, S. J., Van Hooft, J. A., Bosveld, F. C., de Roode, S. R., Moene, A. F., & Genthon, C. (2017). Regime transitions in near-surface temperature inversions: A conceptual model. *Journal of the Atmospheric Sciences*, 74(4), 1057–1073. <https://doi.org/10.1175/JAS-D-16-0180.1>
- Van de Wiel, B., Moene, A., Hartogensis, O., De Bruin, H., & Holtslag, A. (2003). Intermittent turbulence in the stable boundary layer over land. part III: A classification for observations during CASES-99. *Journal of the atmospheric sciences*, 60(20), 2509–2522. [https://doi.org/10.1175/1520-0469\(2003\)060<2509:ITITSB>2.0.CO;2](https://doi.org/10.1175/1520-0469(2003)060<2509:ITITSB>2.0.CO;2)
- van der Linden, S. J., Kruis, M. T., Hartogensis, O. K., Moene, A. F., Bosveld, F. C., & van de Wiel, B. J. (2022). Heat transfer through grass: A diffusive approach. *Boundary-Layer Meteorology*, 184(2), 251–276. <https://doi.org/10.1007/s10546-022-00708-7>
- Van Hooft, J. A., Popinet, S., Van Heerwaarden, C. C., Van der Linden, S. J., De Roode, S. R., & Van de Wiel, B. J. (2018). Towards adaptive grids for atmospheric boundary-layer simulations. *Boundary-layer meteorology*, 167, 421–443. <https://doi.org/10.1007/s10546-018-0335-9>
- Watanabe, T., & Kondo, J. (1990). The influence of canopy structure and density upon the mixing length within and above vegetation. *Journal of the Meteorological Society of Japan. Ser. II*, 68(2), 227–235.
- Wiernga, J. (1993). Representative roughness parameters for homogeneous terrain. *Boundary-Layer Meteorology*, 63, 323–363. <https://doi.org/10.1007/BF00705357>
- Yue, W., Meneveau, C., Parlange, M. B., Zhu, W., Van Hout, R., & Katz, J. (2007). A comparative quadrant analysis of turbulence in a plant canopy. *Water resources research*, 43(5).

# ACKNOWLEDGEMENTS

First and foremost, Bas, there are many, many things to thank you for. Thank you for offering me the opportunity to join the Fruitfrost team. I couldn't have made a better choice than doing a PhD with you. Thanks for all your guidance, support, and encouragement. You have been a patient and understanding supervisor and mentor (even when there is a grammar mistake in proposition 10 hah). Thanks for always being available to discuss my research. No matter how crazy the idea is, you always listen to me and give me valuable feedback. Thanks for the freedom you gave me in research directions. Thanks for always reviewing my papers in a lightning-fast way and when you do, you always put positive remarks in the review process. Thanks for doing that. I feel much more motivated and encouraged. I have also learned from you the way to give feedback to colleagues and fellow students. Thanks for your keen observation in spotting an important *bug* in the leaf heat transfer module. Again, there are many, many things to thank you for. I am very grateful to have you as my supervisor, mentor, and friend.

I would like to thank the Fruitfrost team. I want to address how important the weekly Tuesday afternoon meetings are. In these meetings, we come up with research ideas, refine them, and develop them into a research paper. Marie-Claire, thanks for your guidance and supervision. The team/I can always count on you to keep a clear head. Thanks for all the constructive feedback you have given me. Judith, I am very grateful to have you as my research partner and friend. We have had so many fruitful discussions. We have been to so many conferences together. We presented our work *back-to-back*. I will miss those times and I already miss them. Thanks for your endless encouragement and support in both research and life. The road to the PhD would have been much harder without you.

Antoon, thanks a lot for always helping me with modeling questions. I have learned a lot from you. Thanks for your patience. Sukanta, I am very grateful for your help throughout my research journey. You have been an inspiration to me. Stephan and Pier, thanks for the DALES and open boundary discussions we had. Steven, thanks a lot for all the discussions we had on LES model, IBM model, and the open boundary condition. Bart, thanks for helping me with the fieldwork. I also appreciate all the valuable fieldwork tips you shared with me. I am grateful to Prof. dr. Dino Zardi for the opportunity to visit and present at the University of Trento. Thanks for the research discussions and your encouragement.

Simulations within this work were carried out on supercomputers: (1) DelftBlue operated by (DHPC) and (2) Snellius, the Dutch National supercomputer hosted by SURF Cooperative.

I am also grateful to the GRS group. I had a wonderful time with you. I will miss the coffee breaks at 10am and 3pm. I am thankful to our lovely GRS secretaries: Natascha, Debbie, and Cindy. In addition, I would like to thank Maximilian, Pouriya, Alessandro, and Benjamin for inspiring discussions and coffee chats. I want to thank Sophie, Ann-

Sofie, and Wietske for creating a better PhD environment at GRS. Thank you for the great time spent with you: Ou Ku, Chengyu, Weiran, Weilun, Jan, Serge, Koen, and many others.

Finally, I would like to thank my family for their unconditional love and support. I am grateful to my girlfriend Yiyun for her companionship during my PhD journey. I am thankful for her understanding and encouragement.

# A

## APPENDIX

### A.1. ERROR ANALYSIS

The measured temperature by DTS cables without shielding or active ventilation often can be slightly lower than air temperature during nighttime (Schilperoort et al., 2020). Due to longwave radiative cooling or heat exchange, systematic errors will occur. Together with the uncertainty of temperature measurement itself, the total error will propagate in derived parameters such as the *normalized warming*.

This section estimates the total error of *normalized warming*  $\Delta T/\Delta T_{\max}$  (NW in Eq. 2.1) using error propagation. The total error of *normalized warming* is composite of the uncertainty  $\sigma_{NW}$  and systematic offset  $S_{NW}$  of *normalized warming*. Based on Eq. 2.1, the uncertainty  $\sigma_{NW}$  can be expressed in Eq. A.1, where the cross-terms are neglected.

$$\frac{\sigma_{NW}}{\Delta T/\Delta T_{\max}} \approx \sqrt{\left[\left(\frac{\sigma_{\Delta T}}{\Delta T}\right)^2 + \left(\frac{\sigma_{\Delta T_{\max}}}{\Delta T_{\max}}\right)^2\right]}, \quad (\text{A.1})$$

where  $\sigma_{\Delta T}$  and  $\sigma_{\Delta T_{\max}}$  are the variances of  $\Delta T$  and  $\Delta T_{\max}$ , respectively. There are given by

$$\sigma_{\Delta T} = \sqrt{\sigma_{T_{on}}^2 + \sigma_{T_{off}}^2 + \sigma_{T_{on,ref}}^2 + \sigma_{T_{off,ref}}^2} \quad (\text{A.2})$$

$$\sigma_{\Delta T_{\max}} = \sqrt{\sigma_{T_{hub}}^2 + \sigma_{T_{off}}^2} \quad (\text{A.3})$$

For every cable measurement, the uncertainty is the accuracy of measured temperature  $\sigma_T$ , which is 0.1 K. Then,  $\sigma_{\Delta T}$  equals to 0.20 K and  $\sigma_{\Delta T_{\max}}$  equals to 0.14 K in Eq. A.2, A.3. Based on Eq. A.1, the averaged  $\sigma_{NW}$  calculated for 2 m and 1 m are  $\pm 2.3\%$  and  $\pm 1.9\%$  respectively.

For systematic offset  $S_{NW}$ :

$$\frac{S_{NW}}{\Delta T/\Delta T_{\max}} \approx \frac{S_{\Delta T}}{\Delta T} - \frac{S_{\Delta T_{\max}}}{\Delta T_{\max}} \quad (\text{A.4})$$

With:

$$S_{\Delta T} = (S_{T_{on}} - S_{T_{off}}) - (S_{T_{on,ref}} - S_{T_{off,ref}}) \quad (\text{A.5})$$

$$S_{\Delta T_{\max}} = S_{T_{hub}} - S_{T_{off}} \quad (\text{A.6})$$

Where  $S_T$  is the corresponding systematic offset for cable temperature at different periods and sections. 2020 estimated the offset by comparing the temperature of unshielded cables to measurements from a psychrometer. The offset varies under different conditions of longwave radiation and wind speed. Specifically, the offset during the on mode  $S_{T_{on}}$  can be different in ( $S_{T_{on,in}}$ ) or outside ( $S_{T_{on,out}}$ ) the influenced area. In our study, the averaged net longwave radiation during the off and on mode are  $-33 \text{ Wm}^{-2}$  and  $-27 \text{ Wm}^{-2}$  respectively (see Fig. 2.2). The average wind speed is around  $0.30 \text{ ms}^{-1}$  during off mode. During on mode, the average wind speed in the influenced area is approximated as  $3 \text{ ms}^{-1}$ . Following 2020,  $S_{T_{on,in}}$  is estimated to be  $-0.05 \text{ K}$ , and  $S_{T_{on,out}}$ ,  $S_{T_{on,ref}}$  are approximated to be  $-0.20 \text{ K}$ , where the minus sign indicates lower temperature relative to air temperature. During the off mode,  $S_{T_{off}}$ ,  $S_{T_{off,ref}}$ ,  $S_{T_{hub}}$  are approximated as  $-0.30 \text{ K}$ . Based on Eq. A.4, Eq. A.5, A.6, the averaged systematic offset for the *normalized warming* in ( $S_{NW,in}$ ) or outside ( $S_{NW,out}$ ) the area of influence are  $+2.2\%$  and  $0\%$  respectively. Please note that  $S_{\Delta T_{\max}}$  always approaches to zero due to same offset of  $S_{T_{hub}}$  and  $S_{T_{off}}$ .

In summary, the error of the *normalized warming* is expected to lie within the range of  $(-2.5\%, +4.5\%)$  at 2 m and  $(-1.6\%, +3.8\%)$  at 1 m based on error propagation calculation.

## A.2. DESCRIPTION OF QUADRANT-HOLE (QH) ANALYSIS

The QH analysis divides the fluxes into four quadrants (hereafter Q1, Q2, Q3, and Q4) based on the signs of two individual flux-component quantities (such as  $w$  and  $u$  in the momentum flux). For the x-component of momentum flux displayed in Fig. A.1, for example, the flux contributions can be decomposed as (Lu & Willmarth, 1973; Yue et al., 2007):

Q1 when  $u' > 0$ ,  $w' > 0$ , outward interaction

Q2 when  $u' < 0$ ,  $w' > 0$ , ejections

Q3 when  $u' < 0$ ,  $w' < 0$ , inwards interaction

Q4 when  $u' > 0$ ,  $w' < 0$ , sweeps

For instance, the events of slow air parcel ( $u' < 0$ ) moving upwards ( $w' > 0$ ) are ejections. The sweeps events are characterized by fast air parcel ( $u' > 0$ ) transporting downwards ( $w' < 0$ ). In contrast, the motions of heat flux are sometimes defined differently in literature. To avoid confusion, we here adapted the definition from Lee and Black, 1993. The events of heat flux in Q1, Q2, Q3, and Q4 are defined as “warm updraft”, “cool updraft”, “cool downdraft”, and “warm downdraft”, respectively.

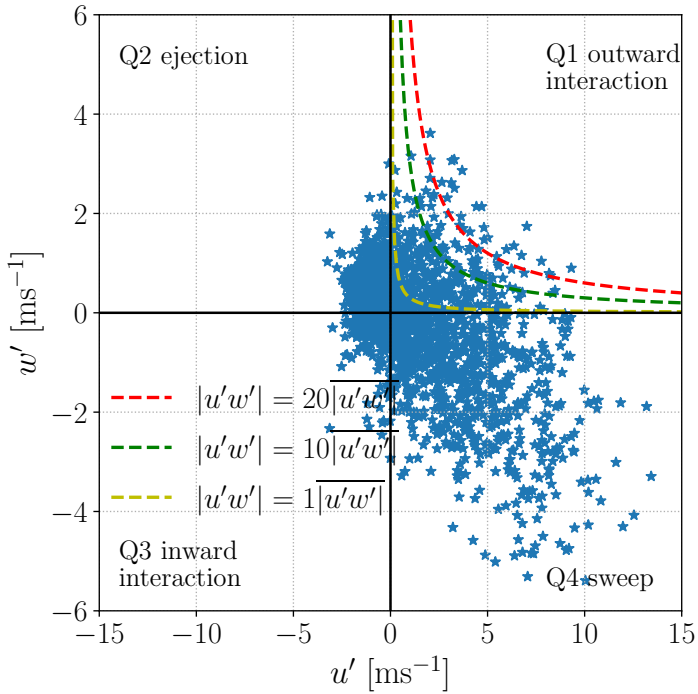


Figure A.1: A schematic of quadrant events based on the x-component of momentum flux measured at A1 during on mode and three examples of hole region ( $H = 20, 10, 1$ ). Points outside the hole regions indicate the flux contribution for each hole sampling.

To further characterize flux distributions in each quadrant, Hole Analysis, a conditional sampling technique, partitions the fluxes outside the holes based on the magnitude of fluxes. Here the partition condition is based on the time-averaged absolute value of fluxes  $\overline{|u'w'|}$  and the hole size  $H$ . For example, outside the hole implies:

$$|u'w'| \geq H\overline{|u'w'|} \quad (\text{A.7})$$

Next, the averaged flux  $\overline{|u'w'|}$  is chosen as the normalizer and the value is fixed in each scenario. Then, the flux distribution is a function of the hole size, and in this way the contribution of extremes to the flux is characterized. As the hole size  $H$  increases, the events of the fluxes have less chance of falling outside of the hole, and the significance of the instantaneous flux to the mean is relatively higher (Fig. A.1). To group the flux events in each quadrant and hole size, a conditional function  $I_{i,H}(u'w')$  is introduced

$$I_{i,H}(u', w') = \begin{cases} 1, & \text{if } (u'w') \text{ is in quadrant } i \text{ and } |u'w'| \geq H\overline{|u'w'|} \\ 0, & \text{otherwise} \end{cases} \quad (\text{A.8})$$

In Fig. A.1, for example,  $I_{1,10}$  equals one when the fluxes events fall in Q1 and outside the green dashed line. The values of the grouped fluxes in each quadrant ( $i$  th), as a function of hole size  $H$ , are summed and then normalized by the total fluxes:

$$S_{i,H} = \frac{\int_0^{T_{sp}} |u'w'(t)| I_{i,H}(u', w') dt}{\int_0^{T_{sp}} |u'w'(t)| dt} \quad (\text{A.9})$$

Where the normalized fluxes, called the fluxes *value fraction*  $S_{i,H}$ , in Eq. A.9 is similar to the definition in (Yue et al., 2007) in a different format.  $T_{sp}$  is the sampling period. Since the absolute values of the fluxes during the on mode are much larger than the off mode due to machine operation, here only relative distributions of the motions in each operation mode are compared. Furthermore, the frequency of the fluxes events in each quadrant or hole is assessed by the *duration fraction*  $t_{i,H}$ .

$$t_{i,H} = \frac{1}{T_{sp}} \int_0^{T_{sp}} I_{i,H}(u', w') dt \quad (\text{A.10})$$

### A.3. PERIODIC BOUNDARY CONDITIONS IN A LARGE-SIZE DOMAIN

In this appendix we demonstrate, using periodic boundaries, that the wave effects generated by the WM have little influence on the inflow boundary condition. Fig. A.2a presents the streamwise air temperature at 2 m height over the simulation period. After the WM starts operation, the air temperatures rise near the WM and the warming effect propagates downstream and upstream. Due to the background wind effect, the warming waves propagate further downstream than upstream. In panel b the time-averaged temperature profiles during the operation warms much close to the WM. At the boundaries of domain, these two profiles shows little influence of the WM mixing. This is also the case for an instantaneous temperature profile during the operation.

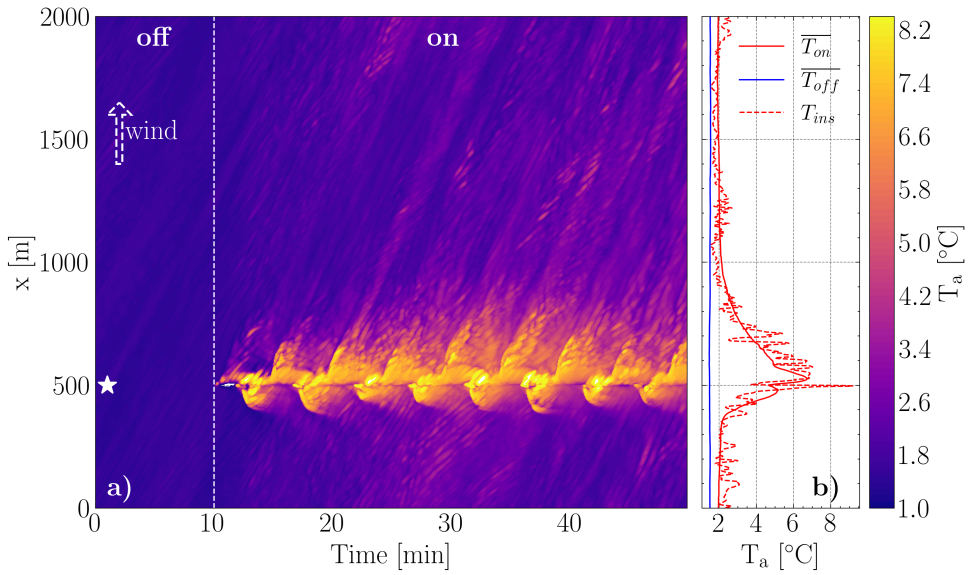


Figure A.2: Panel a shows the distribution of streamwise air temperatures at a 2 m height during the off and on periods of the WM. These profiles are taken across the WM location. The starting time of the WM is marked by a white dashed line. The WM location is denoted by a white star and the direction of the background wind is indicated with a white dashed arrow. In panel b the air temperature profiles are time-averaged for off and on periods ( $\overline{T_{on}}$  and  $\overline{T_{off}}$ ) and one instantaneous profile ( $T_{ins}$ ) is plotted from the operation period.



# CURRICULUM VITÆ

**Yi DAI (戴意)**

11-06-1996      Born in Hubei, China.

## EDUCATION

2014–2018      Bachelor of Engineering in Environmental Science  
Hohai University, Nanjing, China

2018–2020      Master of Environmental Science  
Delft University of Technology, Delft, The Netherlands

2020–2024      Doctoral Candidate  
Delft University of Technology, Delft, The Netherlands

2024–present    Post-doc researcher  
Wageningen University & Research, Wageningen, The Netherlands



# LIST OF PUBLICATIONS

## First author, peer reviewed

- **Dai, Y.**, van Hooft, A., Patton, E., Boekee, J., van der Linden, S., ten Veldhuis, M.C., van de Wiel, B.J., *Integrated large-eddy simulation for modeling plant-tissue warming induced by wind machines in an orchard canopy*. [Agricultural and Forest Meteorology 356](#), 110175.
- **Dai, Y.**, Boekee, J., Schilperoort, B., ten Veldhuis, M.C., van de Wiel, B.J., *Wind machines for frost damage mitigation: A quantitative 3d investigation based on observations*. [Agricultural and Forest Meteorology 338](#), 109522.
- **Dai, Y.**, Basu, S., Maronga, B. et al. *Addressing the Grid-Size Sensitivity Issue in Large-Eddy Simulations of Stable Boundary Layers*. [Boundary-Layer Meteorol 178](#), 63–89 (2021)

## Co-author, peer reviewed

- Boekee, J., **Dai, Y.**, Schilperoort, B., van de Wiel, B.J., ten Veldhuis, M.C., *Plant–atmosphere heat exchange during wind machine operation for frost protection*. [Agricultural and Forest Meteorology 330](#), 109312.
- Boekee, J., van der Linden, S.J.A., ten Veldhuis, M.C. et al. *Rethinking the Roughness Height: An Improved Description of Temperature Profiles over Short Vegetation*. [Boundary-Layer Meteorol textbf190](#), 31 (2024).

## Measurement data

- **Dai, Yi**; Boekee, Judith; Schilperoort, Bart; Veldhuis, Marie-Claire ten; van de Wiel, B. J. H. (Bas) (2023): *Data underlying the publication: Wind machines for frost damage mitigation: A quantitative 3D investigation based on observations. Version 1*. [4TU.ResearchData. dataset](#).
- Boekee, Judith; **Dai, Yi**; Schilperoort, Bart; van de Wiel, B. J. H. (Bas); Veldhuis, Marie-Claire ten (2023): *Data underlying the publication: Plant–atmosphere heat exchange during wind machine operation for frost protection. Version 1*. [4TU.ResearchData. dataset](#).

## Open source code

- The model, analysis codes and processed data are publicly available on [github](#).